7-28-2014

Synchrotron-based X-ray Imaging to Characterize Structural and Chemical Changes in Energy Materials

William M. Harris
University of Connecticut - Storrs, wmasonharris@gmail.com

Synchrotron-based X-ray Imaging to Characterize Structural and Chemical Changes in Energy Materials

William Mason Harris, PhD
University of Connecticut, 2014

The development of increasingly complex, multiphase, and micro-scale composite materials has led to a simultaneous increase in the demand for characterization techniques capable of examining and evaluating the quality of these material systems. These types of composites, which can include such devices as fuel cell and battery electrodes and dense gas separation membranes, display an intimate link between the microstructural arrangement of the various constituent phases and the device performance. This connection is often manifested through coupled transport, reaction, and degradation processes occurring at the micro-scale and conformal to the detailed phase distribution. Therefore, direct examination of the microstructure is critical to understanding how a composite material will perform within the device of its intended purpose.

This work is aimed at developing new characterization capabilities, particularly through the use of transmission x-ray microscopy and x-ray nanotomography, to examine these types of dense composite materials. The new tools developed in this dissertation add to existing characterization methods, but provide valuable new opportunities for the direct visual as well as quantitative evaluation of real structures in three dimensions at the nanoscale. Full-field absorption contrast and x-ray absorption near edge spectroscopy (XANES) methods are applied using a synchrotron-based microscope with a tunable incident x-ray beam. The elemental and chemical specificity permitted by these methods is exploited to obtain accurate identification and mapping of multiple solid phases in 3-D, including unintentional/poisoning phases introduced

during material fabrication or operation. The developed imaging capabilities are then applied to several different materials relevant to real applications of heterogeneous functional materials, and provide a means for evaluating the likely implications of the unintentional phases on the performance of the microstructure. In addition, a statistical approach is introduced to help guide the determination of a representative volume element (RVE) sample size for the accurate measurement of microstructural properties from experimental data.

Synchrotron-based X-ray Imaging to Characterize Structural and Chemical Changes in Energy Materials

William Mason Harris

B.S., University of Connecticut, 2010

A Dissertation

Submitted in Partial Fulfillment of the

Requirement for the Degree of Doctor of Philosophy

at the

University of Connecticut

2014

APPROVAL PAGE

Doctor of Philosophy Dissertation

Synchrotron-based X-ray Imaging to Characterize Structural and Chemical Changes in Energy Materials

Presented by

William Mason Harris, B. S.

Major Advisor_____

Wilson K. S. Chiu

Associate Advisor_____

Brice Cassenti

Associate Advisor_____

Eric Jordan

Associate Advisor_____

Ugur Pasaogullari

Associate Advisor_____

Michael Pettes

Associate Advisor_____

Wah-Keat Lee

University of Connecticut

2014

Acknowledgements

I'd like to acknowledge support and guidance from a number of people over the years, starting with my friends and family. Without them, I certainly wouldn't be the person I am today. It is with their support that I've had the continued motivation to pursue my interests and always put forth my best effort. I would also like to include my close friends and teammates on the UConn Skydiving Team for repeatedly helping me enjoy the best weekend stress reliever I can imagine.

I owe a tremendous thanks to all of the members of the research group I have worked with at UConn over the past several years. First and foremost this includes Prof. Wilson Chiu, who has provided me with countless educational and professional opportunities which have truly made my graduate career at UConn a pleasure. I especially appreciate the support for frequent travel to synchrotron facilities across the country, which has been a unique and enjoyable experience. I'd also like to recognize other members of the research group who have all been very helpful over the years, including (in alphabetical order) Alex Cocco, Matthew DeGostin, Kyle Grew, John Izzo Jr., Andrew Kiss, Jeffrey Lombardo, Timothy Myles, Dr. Arata Nakajo, Prof. George Nelson, and Dr. Aldo Peracchio. I owe particular thanks to Andrew Kiss, who has been not only an excellent lab-mate but also a great roommate over the past four years, as well as Alex Cocco and Jeffrey Lombardo who have spent countless hours producing samples for synchrotron experiments. In addition, I'd like to thank the members of my advisory committee, Prof. Brice Cassenti, Prof. Eric Jordan, Prof. Ugur Pasaogullari, and Prof. Michael Pettes of the University of Connecticut as well as Dr. Wah-Keat Lee of Brookhaven National Laboratory. I'd also like to thank the remaining faculty and staff in the UConn Mechanical Engineering department who have been very helpful.

I would also like to thank the staff of the synchrotron beamlines where much of the work in this dissertation has been conducted. At the Advanced Photon Source I would like to thank Alex Deiry, Barry Lai, Joan Vila-Comamala, and Steve Wang. At the National Synchrotron Light Source I'd like to thank Yu-Chen Karen Chen-Wiegart, Yong Chu, Chris Eng, and Jun Wang. And lastly, at the Stanford Synchrotron Radiation Lightsource I'd like to thank Joy Andrews, Doug Van Kampen, Yijin Liu, Florian Meirer, Johanna Nelson, and Piero Pianetta. In particular, Karen Chen-Wiegart and Yijin Liu provided repeated and extensive help with the synchrotron experiments, including everything from microscope operation to processing of results, and I am very grateful to have had the opportunity to work with them.

There have been numerous researchers involved with most of the projects presented in this dissertation, and I'd like to thank them for their guidance and support. The work presented on the solid oxide fuel cell cathodes is the result of an excellent collaboration with researchers from the Ecole Polytechnique Fédérale de Lausanne in Switzerland. From that group I'd like to thank Dr. Marco Cantoni, Prof. Christos Comninellis, Dr. Jan Van herle, Henning Luebbe, J. Andreas Schuler, and Pietro Tanasini. I'd also like to thank Prof. Meilin Liu and Dr. Mingfei Liu at the Georgia Institute of Technology for providing the sulfur-treated sample, as well as their expertise and guidance, related to sulfur poisoning of SOFC anodes. In addition, I'd like to thank Prof. Kyle Brinkman for his expertise and guidance of the work on gas separation membranes, as well as the electron microscopy contributions provided by Dr. Dong Su at the Center for Functional Nanomaterials at Brookhaven National Laboratory. Use of the computational facilities at the UConn Booth Engineering Center for Advanced Technologies (BECAT) and the electron microscopy facilities at the Institute of Materials Science (IMS) are also gratefully acknowledged.

Lastly, I would especially like to acknowledge the financial support that has made my studies in graduate school possible. First and foremost, I am very grateful for support from the Department of Energy's Energy Frontier Research Center (EFRC) on Science Based Nano-Structure Design and Synthesis of Heterogeneous Functional Materials for Energy Systems (HeteroFoaM Center, award DE-SC0001061) directed by Prof. Kenneth L. Reifsnider. Working with all members of the HeteroFoam team, including professors, research scientists, and fellow students, has been an enjoyable and educational experience. I would also like to thank the Department of Mechanical Engineering at UConn for partial support through teaching assistantship appointments.

Table of Contents

1. Introduction

1.1. Heterogeneous Functional Materials

Recent improvements in fabrication techniques, increased demand for improved energy efficiency, and a trend towards miniaturization of technological devices have led to the emergence of a new class of small-scale functional materials. This rather broad class of materials is characterized particularly by multiphase, often porous composites with functionality spanning a range of length scales from the atomic to device level. This definition has been embodied by the recent use of the term "HeteroFoaM" to describe heterogeneous functional materials.[1,2] Examples of the types of devices in which these materials have played a critical role, particularly in regards to energy systems, include fuel cells, electrolyzers, solar cells, batteries, and solid-state gas separation membranes.[3] Although each of the above-mentioned devices was designed to perform a specific task, they contain many similarities in the materials from which they are constructed. They typically contain multiple solid phases, for which the intrinsic properties of each have been optimized to perform a certain task, such as conduction or catalysis. However, one of the trademark features of HeteroFoaMs is the sometimes unexpected device performance which is observed when more than one of these phases is included as a constituent of a composite material. In this case, it is no longer appropriate to consider the behavior of various components individually; the HeteroFoaM can only be properly characterized and thus designed by considering its composition, structure, and performance in a comprehensive manner.

As a starting point, it is worth discussing the multiple length scales relevant to these material systems. Most obviously is the macro-scale, that which can be seen with the eye and

the scale at which a useful response is observed. At the macro-level we expect the device to perform some end function, whether it is energy conversion, storage, gas separation, etc. The end metrics on which we evaluate the usefulness of the device are typically measured or predicted on the macro-scale, without an intimate examination or description of a smaller scale. As a result, properties based on an "averaged" description of the underlying material components are used to connect to performance. This may include such properties as exchange current density, conductivity, permeation, density, and so on. On the other end of the spectrum is the atomic scale. The most basic building blocks of matter, and their specific arrangement, will dictate the ability of a material to perform a very specific function and therefore fill a specific role within the device. Of importance at the atomic level is bonding states, defect chemistry, molecular motion, grain orientation, and so on.

In between the macro and atomic scales is an intermediate length scale: the mesoscale (sometimes also called the microscale). It is the mesoscale that provides the links between the building blocks of the atomic scale and the device response of the macroscale. Included at this scale are the intricate and interdependent distributions of the various material phases. Typically for a multiphase composite, the functionality depends on the detailed geometry of its constituents at the mesoscale. This is true in terms of a number of aspects, including the creation of transport pathways and restrictions, the formation of new solid phases whether intentional or accidental, the distribution of reaction sites at which multiple phases and thus multiple mobile species convene, and the long term stability of a system due to its surface topology and evolution under non-equilibrium conditions. An improved understanding of the material structure at this scale, and the connections between the structure and device performance, could help guide future design and materials selection for next-generation energy devices.

1.2. Microstructure-Performance Connections

A number of studies have been published in recent years highlighting this connection between microstructure and device performance. The following discussion is meant to present just a brief review of some of the works investigating this connection. Grew *et al*. presented one of the earliest demonstrations of x-ray nanotomography for a composite solid oxide fuel cell anode.[4] The imaged structure was used to analyze transport processes and the distribution of localized restrictions in the transport of charge and mass through the ion-conducting and pore phases, respectively. Lynch *et al.* performed finite element simulation studies on the cathode of a solid oxide fuel cell imaged by x-ray nanotomography.[5] The activation of the cathode for electrochemical reactions was found to be strongly dependent on the microstructure, particularly due to the conduction pathways in the immediate vicinity of reaction sites. Experimental results were presented by Song *et al.* for the electrochemical impedance and polarization resistance of SOFC cathodes fabricated using different starting powder sizes and different sintering temperatures.[6] Results indicate that the differences in microstructure produced by the processing conditions had significant impacts on cell performance. Very small starting powders were found to undergo excessive grain growth during sintering, and lead to a decrease in electrochemical reaction sites, inhibition of ionic conduction pathways, and overall lower power output. A combination of percolation theory and simulated microstructures was employed by Cannarozzo *et al.* to develop an SOFC electrode model capable of linking composition, thickness, and microstructure with performance evaluated in terms of electrode overpotential and current density.[7] The authors note that electrode design can be formulated as an optimization problem aimed at simultaneously minimizing reaction and transport losses within the detailed

structure. An experimental approach was taken by Zhao *et al.* with similar goals.[8] The authors varied the porosity and thickness of SOFC components and measured the ohmic area-specific resistance and polarization of the cells in operation. Electrochemical results were compared with predictions from a simple analytical model. Results showed that when the thickness of the electrolyte is sufficiently small, there are significant contributions from the electrodes to the total ohmic resistance. The results from test cells were used to guide selection of optimal fabrication conditions to create the best possible microstructure.

In a review by Song *et al.* possible improvements in lithium ion battery performance are discussed in terms of advances in microstructural design.[9] The authors elaborate on the benefits of nanoscale features, which include shorter diffusion pathways, larger active surface area, and improved lithium storage and charge/discharge rate. Some of these effects were investigated by Chen et al., who used *in-situ* TXM to observe microstructural changes in Li-ion battery cathode materials during calcination processes.[10] In the 400°-800°C temperature range the authors observed crack formation leading to radial pore structures in synthesized particles, as well as chemical heterogeneity due to localized distributions of Ni and Mn species. The cracks are likely to provide the benefit of an electrolyte transport pathway towards the particle interior as well as more efficient Li ion diffusion, and were shown to give quicker charge/discharge rates. However, the segregation of Ni and Mn decreased the overall Ni^{+2}/Ni^{+4} redox capacity. Lastly, a review by Kharton *et al.* of mixed ionic-electronic conducting materials acknowledges the consistent literature observation of the microstructural impacts on total conductivity.[11] The authors also point out the potential for multiphase mixed-conducting membranes to produce additional emergent phases, which may either enable or inhibit performance depending on their

chemical composition and spatial distribution within the composite relative to the primary phases.

1.3. The Necessity of Direct 3-D Imaging

For HeteroFoaM materials, including but not limited to the examples mentioned above, gaining an accurate understanding of the microstructure-performance connection requires accurate three-dimensional imaging. This is due in large part to the materials' multiphase nature, in which the exact distribution of each one of the phases plays a critical role in the system and is immediately relevant to whether it is able to contribute to (or inhibit) the performance. In real devices, this distribution is inherently 3-D. This has become even more relevant in recent years, as new developments in fabrication techniques have enabled material design to move towards a deterministic rather than guess-and-check approach.[12-16] Simultaneous improvements in fabrication and materials characterization will provide opportunities for science-based design and analysis of real materials with tailored properties.

This includes properties which are not possible to examine with 2-D imaging techniques, notably network contiguity and tortuosity. As multiple phases form intertwined network structures, the connectedness and geometry of those structures can have a significant impact on their function. In many cases, including fuel cells, batteries, and dense ceramic membranes, each constituent phase of a composite serves as a transport medium for a given species (or in some cases multiple species). Therefore, the effectiveness of that phase in facilitating the transport of a particle from point A to point B is contingent on the path the particle must follow between those two points. Observation and characterization of these pathways is not possible using a 2-D image, particularly when greater than two phases are involved with each forming its own

percolating transport network. However, with a 3-D image, the spatial distribution of each constituent phase can be examined to identify such features as path lengths and local transport constrictions.

In addition to species transport considerations, long-term material stability can be a factor in HeteroFoams due to mobility of the solid phases themselves in a bulk manner. An example of this is the well-known propensity of nickel particles within solid oxide fuel cell anodes to coarsen under extended operation at high temperature.[17-21] These coarsening processes are driven by interfacial phenomena on a local scale, most notably surface curvature. With functional dependence on surface curvature, the chemical potential of solid phases can vary across length scales similar to the particle sizes themselves, providing significant driving forces for the rearrangement of particle structures, termed microstructural evolution. This can only be accurately measured in 3-D by the determination of the two principle surface curvatures.

1.4. Three Dimensional Imaging Techniques

Direct 3-D imaging techniques to observe these types of materials are somewhat limited. Cocco *et al.* provides a review of some of the common techniques and their applications to energy-related materials.[22] For dense structures consisting primarily of high Z elements, the options are somewhat more limited still. The most common methods include transmission electron microscopy (TEM) tomography, focused ion beam-scanning electron microscopy (FIB-SEM) serial sectioning, and x-ray tomography. While TEM provides the best resolution in the single nanometer range, there are severe limitations on sample size. The specimen must be thin enough to provide electron transmission, which for many dense materials means an impractically small sample. There have been a number of applications, however, imaging isolated high Z

particles and their distribution within a low Z matrix support. This has been used to examine catalyst distributions, as well as some battery and photovoltaic devices.[23-30] For thicker samples, FIB-SEM and x-ray tomography have emerged as the most flexible and powerful techniques for a variety of applications. FIB-SEM has seen extensive use due its widespread accessibility. The technique operates by obtaining an image of an exposed surface, and then using the ion beam to mill away a thin layer of material, typically with the thickness roughly equal to the lateral imaging resolution. After milling, another image is acquired, and so on, producing a series of 2-D cross sections. The cross-sections are then aligned to produce a 3-D data set. FIB-SEM can provide excellent spatial resolution and reasonable elemental sensitivity depending on the relative density of the different phases, and if advanced techniques are employed such as the embedding of pores with an epoxy resin or imaging using an energy selective backscatter detector.[31-37] Theoretically, FIB-SEM can also image very large volumes, as the time required for milling and image acquisition are the only limiting factors. However, FIB-SEM suffers from two main disadvantages. The first is that it must operate in a high vacuum (or near-vacuum in the case of environmental SEM) which inhibits the ability to perform realistic *in situ* measurements even with 2-D imaging. Secondly, because the material is lost when it is milled from the surface, the method is destructive. This eliminates the possibility to perform imaging of the same sample before and after some environmental exposure, for example.

X-ray tomography methods provide some complementary capabilities to aid in the characterization of these types of materials. Included in the broad title "x-ray tomography" are variations with both micro and nano level resolution, as well as both lab-based and synchrotron-based systems. The distinguishing feature of nano versus microtomography is the use of x-ray

focusing optics, which over recent years has seen significant advances and has even been implemented in the newest lab systems. The most crucial of these optics is the zone plate objective lens, a diffraction optic lying downstream of the sample to focus transmitted x-rays onto the detector.[38-42] The precision with which the zone plate is manufactured dictates the instrument resolution, and the best reported result so far is 17 nm.[38] However, these lenses typically have low efficiency on the order of single percent and therefore require a high-intensity x-ray source, or very long exposure time, to provide sufficient signal. Conversely, microtomography lacks the optics and instead directly uses transmitted photons in either a parallel beam (synchrotron) or cone beam (lab source) arrangement to produce a projection at the detector. While this simplification reduces the cost and complexity quite a bit, it does so at the expense of the image resolution which is typically limited to about 1 micron.

X-ray tomography systems in general, whether or not focusing lenses are used, can be based on either a lab system or at a synchrotron beamline. Lab systems use an x-ray tube as the source of photons, which operates by accelerating electrons and bombarding a target material. As the electrons decelerate upon impact, they generate a combination of broad-band Bremmstrahlung radiation as well as characteristic emission lines specific to that target material. The overall low intensity eliminates the possibility of filtering a variable single energy level to produce a tunable monochromatic beam, which would be too weak to provide reasonable signal. Therefore, a polychromatic beam is typically used, which can sometimes lead to the so-called "beam hardening effect", in which low energy photons are more readily attenuated than those of high energy. The result can be a sample which appears denser at the boundaries than the interior. The resolution of lab-based systems is dictated by the size of the x-ray source, which ideally is a

point source but in reality obtains some finite size, as well as the density of pixels in the detector downstream of the sample.

Synchrotron-based experiments provide some unique capabilities due to the high intensity and monochromatic beams that are produced. Synchrotron sources use a monochromator upstream of the experimental station to filter all but a selected energy level of incident photons, and can also be adjusted, providing energy tunability over a range of photon energy. This feature opens the door for elemental and chemical sensitivity by probing known absorption behavior of certain elements or compounds at specific incident energy levels. Furthermore, spectroscopy can be performed, providing a fingerprinting technique for compounds with only subtle differences in absorption behavior. These techniques are explored and applied to real materials in subsequent sections. In addition, synchrotrons provide parallel beam arrangements, simplifying interpretation of 2-D projection images and their correlation with the 3-D tomography reconstruction. The high intensity of the x-ray beam also enables very rapid image acquisition, on the order of 1 image per second. The quick exposure time is helpful for developing *in situ* capabilities, which are made possible due to the fact that x-ray imaging is both non-destructive and does not require a vacuum environment around the sample. Recent work has already proved the viability of *in situ* characterization for dense materials with energy applications.[10,43,44]

1.5. Synchrotron-Based X-ray Nanotomography

The work presented in this dissertation focuses on the use of synchrotron-based x-ray techniques, notably full-field x-ray nanotomography, to image and characterize dense composite

materials for energy-related applications. The imaging work has been performed at three synchrotron facilities:

- Stanford Synchrotron Radiation Lightsource (SSRL), beamline 6-2c, at the Stanford Linear Accelerator Laboratory
- National Synchrotron Light Source (NSLS), beamline X8C, at Brookhaven National Laboratory
- Advanced Photon Source (APS), beamline 32-ID, at Argonne National Laboratory

While each source has its own intricacies, the transmission x-ray microscope (TXM) at each shares the same basic equipment, as shown in Fig. 1 (from [22]). Upstream of the TXM are various mirrors for proper direction of the beam, as well as the monochromator. The beamline then leads to the TXM itself, located in an enclosed room called a "hutch" to decrease radiation exposure when the experiment is running. All components of the beamline and microscope are controlled by computer stations outside of the hutch. The microscopes are capable of providing a field of view on the order of tens of microns, depending on the size and resolution of the zone plate as well as the image magnification.

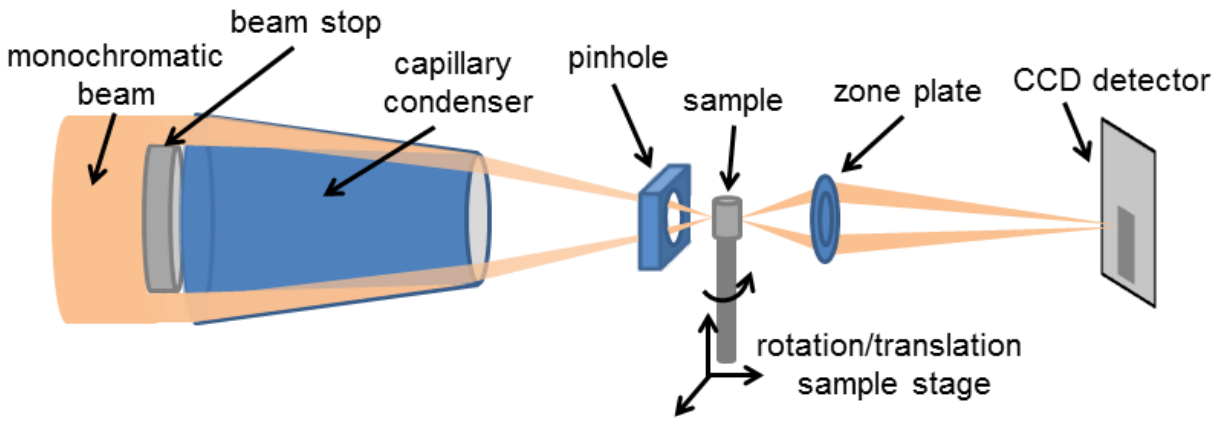

Figure 1: Synchrotron-based transmission x-ray microscope used for nanotomography measurements. A monochromatic incident beam, shown by the orange highlight, enters on the left side of the figure, where photons are guided by a capillary condenser onto the sample, which is mounted on a rotational/translational stage. Transmitted photons are focused by a zone plate objective lens onto a detector downstream. The components are not drawn to scale. Figure from [22].

In general, x-ray transmission images display contrast attributable to two sources: phase contrast and absorption contrast. (The term "phase" is used frequently throughout this dissertation and the literature to describe a solid region of common composition and crystal structure, and is not to be confused with the use of "phase" in this instance which refers to the wave propagation of light). Phase contrast is a result of the phase change of x-ray photons as they traverse the sample, and is often the dominant mechanism in low Z materials, especially in the hard x-ray regime. Imaging methods have been developed to exploit the phase contrast effect and this mechanism is often employed for biological samples, for example.[45-51] However, for the dense high Z materials of interest for energy applications, x-ray interactions are dominated by absorption. Mathematically, an incident beam of intensity I_o is attenuated by a sample according to the Beer-Lambert law:

$$I = I_o \exp\left(-\mu(e) * l\right) \tag{1}$$

where I represents the intensity of the transmitted beam, l is the thickness of the sample, and μ is the linear attenuation coefficient. As shown in Eq. 1, the attenuation coefficient is a function of energy level e, and therefore the intensity of the transmitted beam will also depend on the energy of the beam. The product $\mu(e)*l$ is known as the optical density, OD. The measurement of I_o is

obtained by removing the sample from the field of view and acquiring a background image of the empty space. Figure 2 demonstrates the acquisition of a background image (a), a transmission projection of a cylindrical sample (b), and the optical density image by applying Eq. 1 (c). The cylindrical sample is about 10 microns in diameter, and a gold ball can be seen on the top of the sample, which is typically added prior to imaging for use as a fiducial marker.

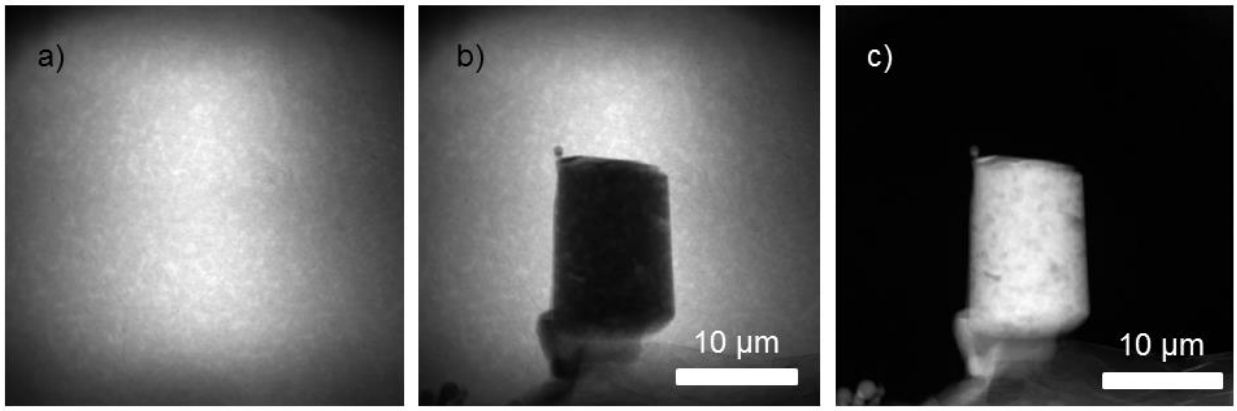

Figure 2: Full field transmission x-ray microscopy images. First, a background image (a) is collected to represent the incident beam intensity I_o. An image of the sample (b) shows the transmitted x-rays, I. The negative of the natural log of (b) divided by (a) yields an image of the optical density (c).

For a composite sample consisting of multiple solid phases, the transmitted beam intensity at every point will then depend on thickness contributions from the various phases, each of which with its own energy-dependent attenuation coefficient

$$I = I_o \exp\left(-\sum_{i=1}^{n} \mu_i(e) * l_i \right) \qquad (2)$$

From an experimental perspective, the best results are obtained when a sample is neither

very transmitting nor very attenuating. This can be conveniently described using the notion of attenuation length, which is the thickness of a sample for which the transmitted beam intensity is a 1/e fraction of the incident intensity (1/e is approximately equal to 0.37). The best results occur for samples which have a thickness similar to their attenuation length. Those which are much thicker will be too thick and have a very small transmission signal ("photon starvation"), while those which are much thinner will have too high of a transmission signal which may be very similar to the background signal. In practice, the attenuation length of a real sample is usually not known *a priori*, as it will depend on the chemical composition, quantity, and distribution of the various phases present. However, reasonable estimates can be calculated using free online tools which are typically close enough to guide the planning of x-ray imaging experiments.[52] The attenuation length, in microns, for several transition metals commonly found in energy materials is shown in Fig. 3. It can be seen that a sample thickness on the order of 10 to 15 microns is typically appropriate. As x-ray energy increases, the photons obtain more penetrating power and are able to transmit through thicker samples, thereby increasing the attenuation length. However, discontinuities at elemental absorption edges occur due to a threshold phenomenon in which the x-rays begin to interact with core shell electrons at a specific energy level. The absorption K-edges of the various elements are depicted in Fig. 3. Absorption edges, and their utility in imaging composite samples, are discussed in more detail and revisited frequently throughout this work.

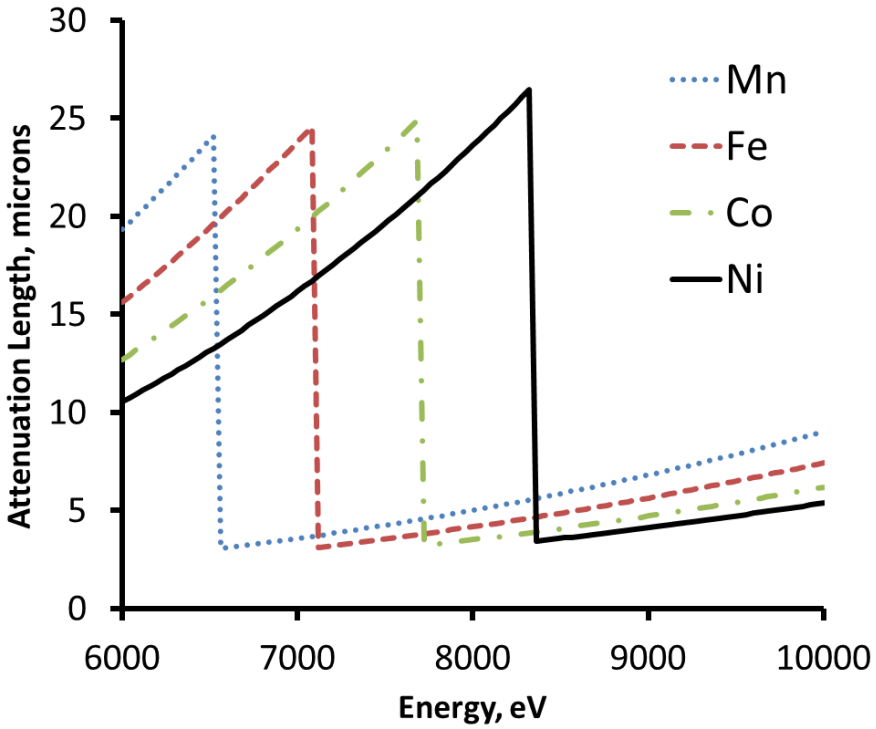

Figure 3: Attenuation length of several elements commonly found in heterogeneous functional materials for energy applications.

Equations 1 and 2 describe the signal that is obtained in a single 2-D projection image. However, to perform tomography and recover the internal structure of the sample requires obtaining many such projection images over a range of incident angles. In practice, this is done by incrementally rotating and imaging the sample at fine angular steps between -90 and +90 degrees. Once all projection images are obtained (several hundred or more is common), they must be aligned to a central axis of rotation prior to the reconstruction process. This is normally done manually by marking a common reference point on each image, thereby defining the position of the object at each angle of rotation. It is common practice to use an optical microscope to place small gold balls on the top of a sample prior to imaging to use as a reference point in the alignment. Recent improvements in microscope stages and software, however, have

begun to eliminate the need for manual interaction, provided the sample is stable throughout the duration of tomographic image acquisition.[53] Once aligned, the projections are reconstructed to recover the 3-D structure. The process of reconstruction is an "inverse" problem, aimed at identifying the unknown object capable of producing the set of known projection images. A wide variety of reconstruction algorithms exist and there is extensive literature on the topic.[54,55,55-58] The most popular and widespread method is filtered back-projection (FBP) due to its robustness, speed, and ease of implementation.[57] However, others have been developed particularly for cases requiring especially high accuracy, low-contrast images, or tomography scans consisting of relatively few angular exposures.[55,56] Some of these are available in the "TXM Wizard" software developed by the staff at SSRL, which has been used frequently in this work.[59] Whatever the method, the resulting 3-D data after reconstruction represents a spatial distribution of the attenuation coefficient μ, sometimes referred to as a density map due to the strong correlation between μ and Z.

1.6. X-ray Nanotomography Challenges

In practice, acquiring quality images using full-field TXM requires consideration of a number of factors. First and foremost is the quality and stability of the synchrotron beam, which is typically out of the user's direct control. The illumination of the field of view by the beam can be manipulated with a number of focusing mirrors, but the beam can tend to "drift" over time, resulting in a changing background signal. This can present complications for experiments requiring long exposures or tomography scans, because the incident beam used to create a projection I (see Fig. 2) is no longer accurately represented by the previously acquired background image I_o. Correct focus is also important, as the focal length of the zone plate lens

changes as a function of beam energy. It is therefore critical to make corresponding adjustments when imaging a sample at multiple energy levels. Examples of well-focused (a) and poorly-focused (b) projections are shown in Fig. 4. "Double edges" and highlights can be seen surrounding features in the poorly-focused image. A reconstruction performed on a set of projections with poor focus is shown as an example in (c). The "halo" outlines surrounding the features are artifacts and can be problematic in subsequent image analysis steps.

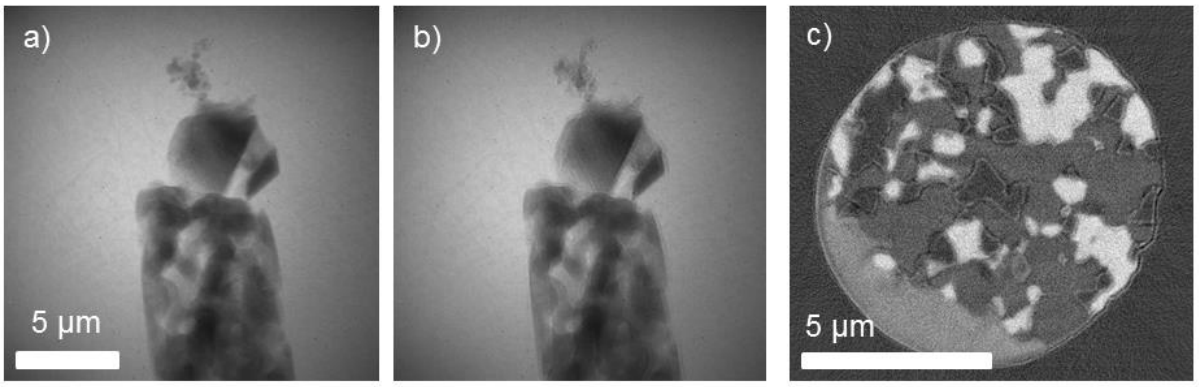

Figure 4: Focus of transmission images. The use of x-ray optics necessitates proper focus of the sample. The typical depth of focus is on the same order of magnitude as the field of view, namely tens of microns. Shown are examples of a well-focused image (a), a poorly-focused image (b), and reconstruction artifacts stemming from poor focus (c).

The experimenter must also consider the angular settings used during tomography. In theory, the Nyquist criterion dictates the number of projections n_θ which should be used to accurately represent the structure based on the number of pixels n_r in the horizontal direction in the 2-D projections

$$n_\theta = \frac{\pi}{2} n_r \tag{3}$$

but in practical applications this level of sampling is often not achieved nor necessary.[57] For manual alignment (clicking of gold balls at each projection angle, as described above), the uncertainty associated with marking the exact same point in every projection offsets the benefits of adding more projections. This has been demonstrated in Fig. 5, which displays cross-sections from the imaging and FBP reconstruction of a sample consisting of a single porous sumaria-doped ceria (SDC) phase. The reconstructions were performed using 181 (a), 361 (b), and 721 (c) projections, in each case evenly spaced over a range of -90 to +90 degrees. While a close examination can reveal marginal improvements between 181 and 361 projections, almost no difference can be seen when increasing to 721 projections. More recently though, automatic alignment capabilities demonstrated by the beamline staff at the NSLS have eliminated the uncertainty associated with manual alignment and thus opened the door for improvements in image quality through increased angular sampling.[53] While acquiring additional angles can become a time consuming exercise (as total tomography run-time is directly proportional to the number of projections acquired), time could potentially be recovered by the fact that manual alignment of the projections is no longer necessary.

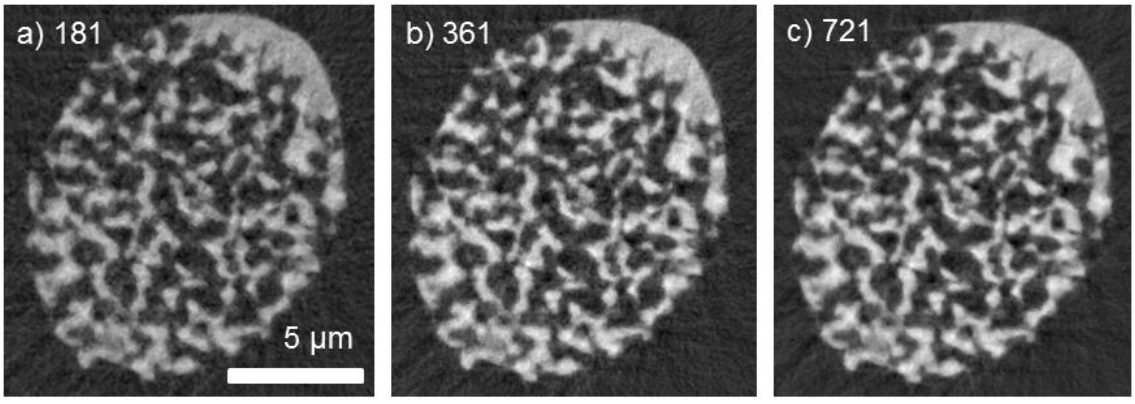

Figure 5: Reconstructions of the same sample using 181 (a), 361 (b), and 721 (c) evenly-spaced projection images.

Lastly, regardless of the angular sampling rate, it has been observed that sampling over a full range of -90 to +90 degrees is critical for accurate reconstruction results. Although most algorithms are capable of operating on a partial data set, reconstruction performed without certain angular exposures results in the so-called "missing wedge" effect and significant artifacts. This is depicted for a multiphase composite membrane sample (to be discussed in section 3.3) in Fig. 6. The same cross sectional slice of the sample is depicted in (a) and (b) and each has an angular step size of 0.5 degrees. However, the reconstruction in (a) was performed utilizing only the projections between -45 and +45 degrees, while (b) includes all projections between -90 and +90. Significant and catastrophic loss in image quality is obtained for the lower sampling range. This result could have significant implications for samples contained within an environmental chamber for *in situ* measurements, as full angular rotation may not be possible due to the additional equipment surrounding and attached to the sample stage.

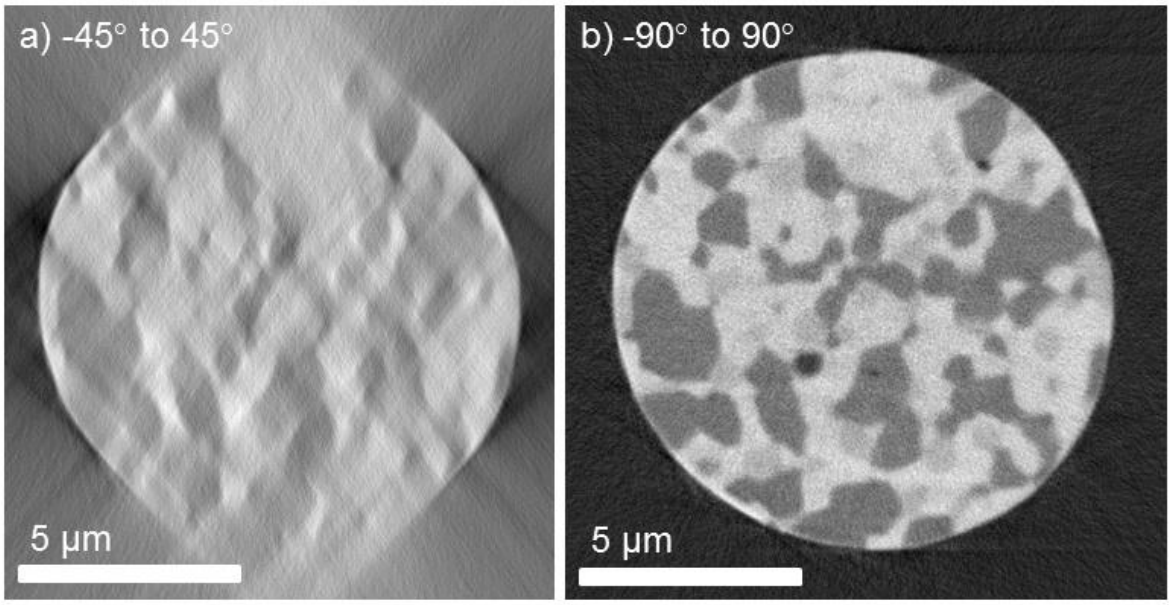

Figure 6: Limited angle tomography. The incomplete rotation of a sample during tomography results in imaging artifacts called the "missing wedge" effect as shown in (a). This issue does not occur when a full range of angles is used, as shown in (b).

1.7. Image Processing Challenges

After imaging, another substantial challenge appears in the processing of the tomography data. The tomography reconstructions provide a 3-D array of grayscale values corresponding to that location's x-ray attenuation. Further characterization of the structure requires first labeling each data point as belonging to a certain phase of material, whether it be a solid phase or pore. This process is termed segmentation, and on its own has been the source of extensive research and methodology development in a number of fields.[60-65] As such, a variety of techniques exist, but adaptation of a given technique to a type of sample is not necessarily straightforward as the process is often very case-specific. The simplest type of sample would contain only solid and pore, and the easiest way to segment such a sample would be the selection of a threshold value, splitting the grayscale histogram into two sections corresponding to the two phases.

However, the process is not as simple when three or more phases exist. Although it is possible to define two threshold values in such a case, it can lead to erroneous segmentation results, particularly at particle boundaries as shown in Fig. 7.

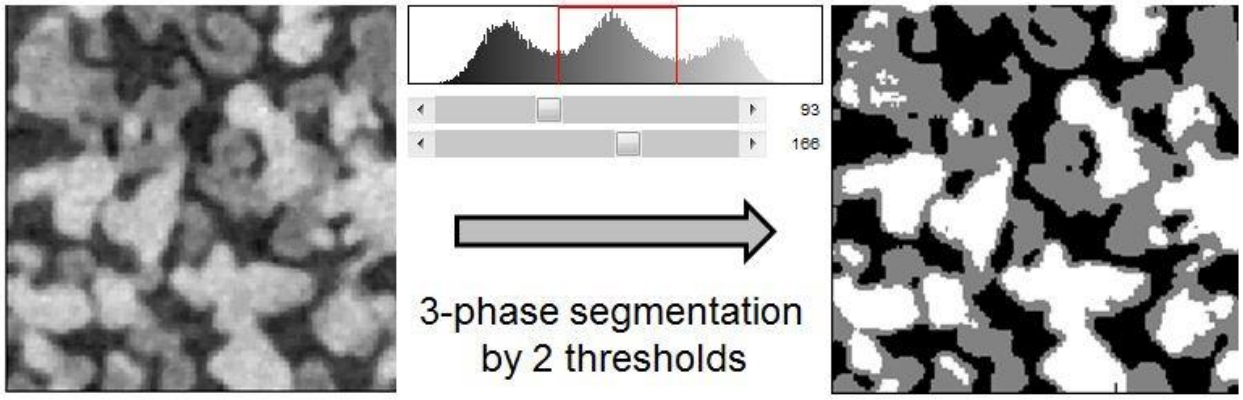

Figure 7: Segmentation challenges. Segmentation of images with more than two phases is complicated by the fact that boundaries of phases are not abrupt, and there is always some amount of blurring of edges. Simply selecting two thresholds according to the histogram will create an incorrect result, as blurred edges are accidentally labeled as the intermediate gray phase.

While a number of alternatives exist, the primary method proposed for this work is the watershed algorithm, which can be placed in a class of methods called “region growing”.[65] The idea is as follows, and is depicted in Fig. 8:

1) Define regions of the domain which you can, with complete confidence, prescribe to certain phases of the material. There is great flexibility with how this can be done, and the result is usually a combination of intuition and trial-and-error on the part of the user. These regions are called “seeds” or “catch basins”.

2) Define boundaries. This is usually done by taking the magnitude of the 3-D gradient map of the data. Because particle boundaries are normally associated with sudden changes in grayscale values, they will be areas of high gradient.

3) The seed regions are overlaid on the gradient map as local minima, and iteratively expanded in a bounded manner based on the gradient map. Locations where neighboring seeds come to touch each other are termed "watershed lines", and correspond approximately to local maxima of the gradient map. When all seeds have been expanded as much as possible, the domain is fully segmented, and the watershed lines represent particle boundaries.

Segmentation methods, including the watershed algorithm, can be somewhat subjective and the responsibility rests on the user to determine what constitutes a "good" segmentation result. Determining factors can include the signal to noise of the reconstructed volume, the size of the features, the spatial variation/frequency of the features, and the contrast between different sample phases.

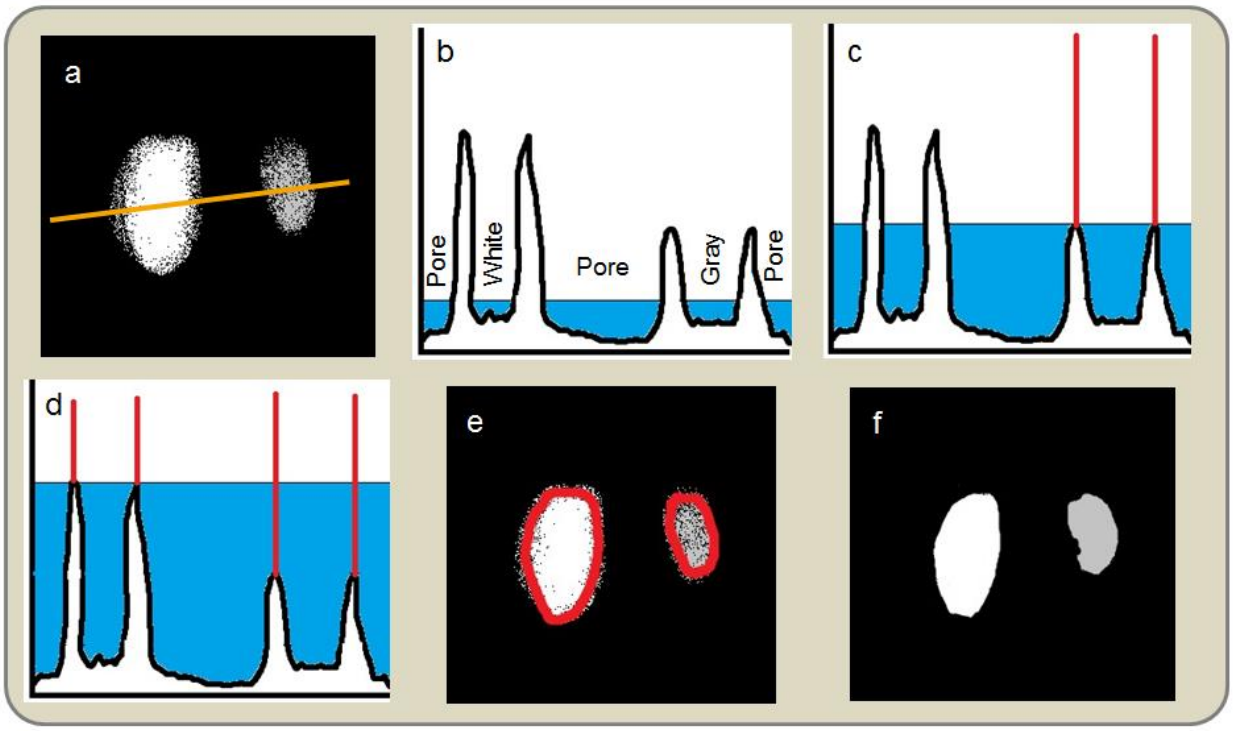

Figure 8: Watershed segmentation algorithm. a) A grayscale image with two objects, one is bright white and the other is gray. b) Gradient magnitude of image (a) along the yellow line. Also shown are regions that can be confidently assigned to either the pore, white, or gray phase, which are termed "seeds". For simplicity, the gradient and algorithm are demonstrated in 1-D in this figure. (c) The "flooding process" causes neighboring watersheds to meet at regions of (local) maximum gradient, as shown in red. These are the watershed lines. (d) Flooding continues until all pixels have been covered and all watershed lines labeled. (e) Watershed lines are used as explicit particle boundaries. (f) Particles are labeled into discrete regions based on the boundaries and watershed "seeds" identified in (b).

1.8. Existing Imaging Tools

Two previously developed tools for x-ray nanotomography imaging and characterization, which are used extensively in this dissertation, are described briefly here. The first is a technique

used for producing samples for x-ray nanotomography imaging. This was developed by former lab-mate Jeffrey Lombardo, and is described in detail in [66]. Almost all samples used in this dissertation were produced by this method, either by Jeffrey Lombardo or lab-mate Alex Cocco. The technique utilizes the milling capabilities of the ion beam in a dual beam focused ion beam-scanning electron microscope. The ion beam is used to mill away material in a pattern of concentric rings surrounding a central un-milled cylinder. With each ring, the ion beam mills deeper down from the sample surface, effectively creating a core sample standing vertically in the middle of a milled cavity. The cylindrical geometry is generally chosen for x-ray nanotomography because it has a well-defined and consistent thickness profile at each incident angle, thus providing consistent transmission behavior for all projections of a tomography scan. The cross-sectional diameter of the cylinder is chosen to be on the order of the material's attenuation length, which is usually around 10-15 microns for the materials in this work. The desired height of the cylinder dictates the necessary ion milling time, as taller cylinders will require the removal of additional material. About 20 microns is usually considered reasonable for the height. Once the milling is complete, a micromanipulator probe and platinum deposition welds are used to lift the cylinder out of the bulk material, and position it on the tip of a pin. Another Pt weld is then used to attach the sample to the pin. The sample can then be handled via the pin using tweezers, pliers, or by hand. Although direct accidental contact with the tip of the pin will immediately dislodge or destroy the sample, the Pt welds themselves have been shown to be remarkably resilient to shock, as carrying by hand or commercial shipping cross-country is typically not a problem. As a side note, the FIB milling technique has also been used to create samples of different geometry, including rectangular prisms, cones, and wedges, but the cylinder geometry is used throughout this work.

An additional set of tools, for microstructural characterization after imaging, have been previously developed by former lab-mate Kyle Grew and have been used extensively in this work. The algorithms used for calculating various properties are described in detail in [67,68]. The routines take as an input the segmented structures, with discrete numeric labels (1, 2, 3, etc.) denoting the different phases. The work in this dissertation was accelerated by numerous minor alterations as well as the compilation of various characterization routines into a comprehensive program written in FORTRAN. These changes were largely performed to make the characterization process more streamlined and "user friendly". Among the more substantial changes was the modification of the code's input routines to accept cylindrical samples for characterization, in addition to cubes or rectangular prisms. Because most samples used in this work are cylindrical in shape, this allows for the analysis of as much of the imaged sample as possible. Another significant improvement was the implementation of message passing interface (MPI) programming for the calculation of network tortuosity. The tortuosity routine in Grew *et al.* solves the Laplace equation in the discrete material microstructure to simulate the diffusion process of a transport species across the domain.[67] The effective flux of the species calculated in this manner is then compared to the "ideal" flux which would be obtained through a straight channel of the same nominal length. The difference between the two can be used to describe the transport limitations in terms of the volume fraction and tortuosity of the transport phase. This approach has been taken by several researchers to calculate tortuosity in discrete structures obtained experimentally.[69-71] However, implementing even the relatively simple finite difference method to solve the Laplace equation becomes computationally expensive for large volumes with slow convergence. It has been observed that volumes larger than 200x200x200 voxels can take days or longer to reach a converged solution. In this work, this problem has been

remedied by splitting the domain into multiple sub-domains, each of which is operated on by a single computer node. Communication between nodes is implemented using MPI routines at the boundaries of the sub domains. With this approach, linear speed-up in processing time is observed for additional computer nodes, up to a point. With too many nodes, communication time becomes a limiting factor rather than computation. In practice, for the typical volume sizes in this work, up to 20 nodes have proven to be beneficial.

2. Synchrotron Transmission X-ray Microscopy Methods

2.1. Elemental Absorption-Edge Imaging

The ability to distinguish materials using TXM is a result of differing levels of x-ray transmission, or conversely x-ray attenuation. This behavior can be characterized by a material's linear attenuation coefficient, μ, with units of inverse length. Attenuation can include both absorption and scattering effects, but in the TXM literature it is common to see the terms "attenuation" and "absorption" used interchangeably, even though that is not rigorously accurate. The attenuation coefficient is related to the intensity of an incident x-ray which is transmitted through a sample via the Beer-Lambert law, Eq. 1, as discussed in section 1.5.

Generally, μ is dependent on the material density expressed in terms of the atomic number Z. High Z elements (and compounds which contain high Z elements) are more strongly attenuating than low Z elements. The attenuation coefficient is also a function of the incident beam energy, as typically μ decreases as beam energy increases.

When a sample is used to obtain a 2-D projection image, the intensity at a given point is a function of both μ and *l*, the sample thickness. If tomography is performed by collecting many projection images over a range of angles, subsequent reconstruction eliminates the thickness effect and recovers a representation of just the attenuation coefficient μ. Therefore, regions in the reconstructed data having the same composition should all share the same value, regardless of their size, shape, or location. Note, the reconstructed value of μ is typically normalized in the reconstruction process, and is therefore not directly relatable to the specific numeric value that could, for instance, be found in a table for some materials. However, the reconstruction will provide a measure of the attenuation coefficient of different regions and species within the

sample relative to each other, and therefore still provide valuable information as to the local variations in composition.

These local variations are most easily observed when different species have substantially different attenuation coefficients, and therefore display noticeable contrast in the resulting tomography. However, in cases where the various species have similar attenuation, improved contrast can be obtained through imaging across an elemental absorption edge. This capability is unique to synchrotron sources, which have a monochromatic and tunable x-ray beam. An absorption edge occurs at an element's binding energy, which is the energy at which an incident particle is sufficient to eject a core shell electron from the interacting atom. Binding energies for each element are known and tabulated and are unique to the given element.[72] When the energy of the incident particle (an x-ray photon in this case) is below the binding energy, it cannot be absorbed via the ejection of the corresponding core shell electron, as shown in Fig. 9(a). Therefore, the x-ray is that much more likely to be transmitted through the sample and reach the detector. However, if the x-ray energy is increased a small amount such that it is just greater than the binding energy, it is much more likely to be absorbed as it ejects a core shell electron, as in Fig. 9(b). The ejection of a core shell electron is accompanied by a relaxation process, which involves an outer shell electron transitioning to fill the core shell vacancy along with an emission of energy equal to the difference in energy between the outer and inner shell electronic states. The emission can occur as an Auger electron or a characteristic fluorescent photon, both of which provide usable signals and are the basis of experimental measurement techniques in their own right. (The use of fluorescent photons will be utilized in section 3.2 in the study of a solid oxide fuel cell anode poisoned by hydrogen sulfide). Within the context of transmission x-ray microscopy, the most significant implication of imaging above an absorption

edge is the drastic increase in x-ray attenuation (and decrease in transmission) that occurs compared to imaging below the edge. The result is a large change in output (transmission signal) for a small change in input (x-ray energy).

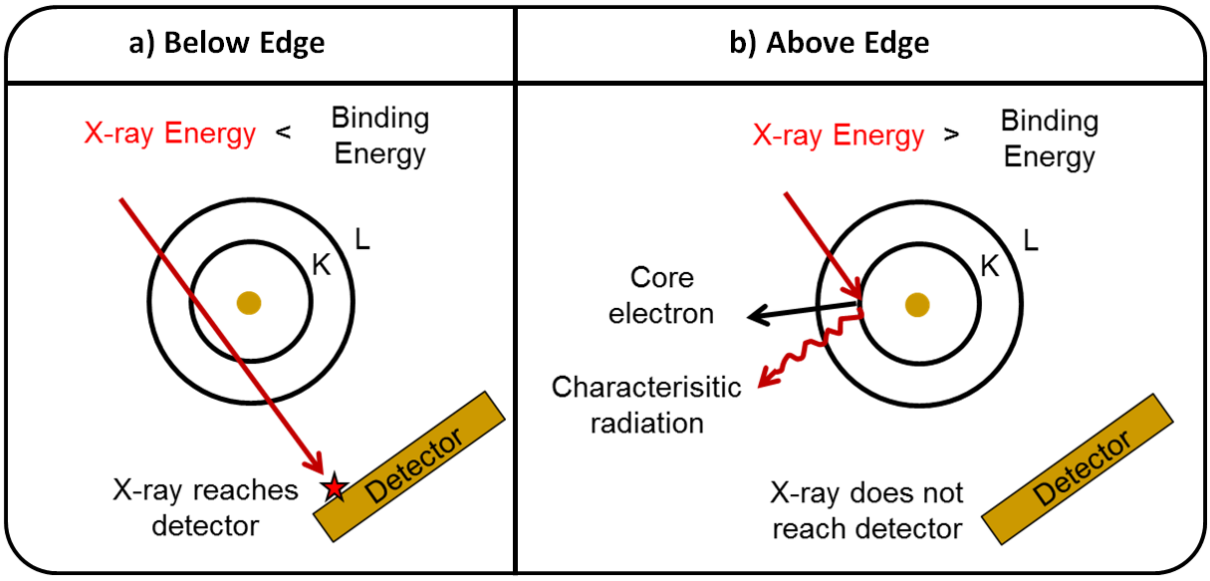

Figure 9: Elemental absorption edges. An incident photon with energy less than an electron's binding energy (a) will not be able to eject the electron from its orbital around the nucleus. However, a slight increase in photon energy, to a level greater than the binding energy (b), will allow a core-shell electron ejection and an attenuated x-ray beam.

For a composite material containing multiple phases, imaging performed at a single energy level may not be able to distinguish the different phases if they have similar attenuation coefficients. However, if absorption edge imaging is performed below and above an edge of an element contained in just one of the phases, that phase will display a contrast change between the two data sets. Thus, elemental mapping capability is obtained. This approach has been applied by our group and others for a number of energy-type composite materials in recent years,

particularly SOFC anodes.[4,73,74] This concept is demonstrated below in Fig. 10 for the first time for an SOFC cathode.

An SOFC cathode consisting of a composite Lanthanum Strontium Manganite, $(La_{0.7}Sr_{0.3})_{0.9}MnO_{3\pm\delta}$, and 8 mol% Yttria-Stabilized Zirconia (LSM-YSZ) composite was fabricated by collaborators at Ecole Polytechnique Fédérale de Lausanne (EPFL), with details provided elsewhere[31,75]. A cylindrical sample was prepared by former lab-mate Jeff Lombardo using the FIB-SEM sample preparation technique. Tomography was performed at SSRL below (6525 eV) and above (6554 eV) the manganese K-edge (6539 eV) using 361 projection images and 1 second exposures. The data was reconstructed using filtered back-projection, with results from the reconstructed data shown in Fig. 10 (a) and (b).

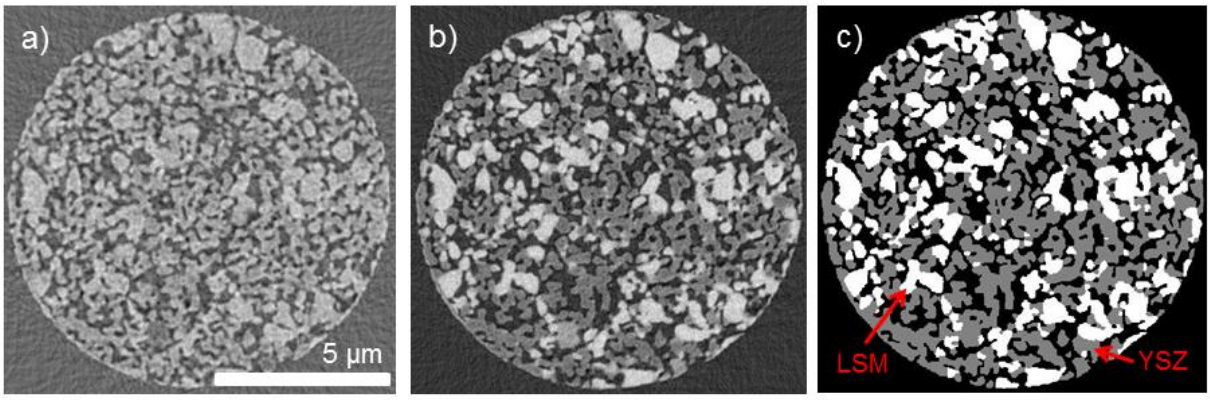

Figure 10: Reconstruction of an LSM-YSZ cathode of a solid oxide fuel cell. Absorption edge imaging across the Mn K-edge reveals contrast change in the LSM phase when moving from below (a) to above (b) the edge. Knowing the bright phase in (b) is LSM, the structure can be segmented to produce a phase map of the electrode (c).

Corresponding slices of the below and above edge data are shown in Fig. 10 (a) and (b), respectively. Below the edge, LSM and YSZ have comparable absorption, and the two phases

are not distinguishable from one another. However, above the Mn K-edge the LSM appears brighter due to the presence of manganese, and the two phases are easily distinguished, as is the pore space. Knowing that the bright regions are LSM, it becomes possible to segment the structure based purely on the above-edge data. (This would not have been possible, however, had imaging not also been performed below the absorption edge since it would remain unknown whether the bright phase is the LSM or YSZ). A watershed algorithm was used to create a segmented representation of the structure, as shown in Fig. 10(c). Additional imaging of the LSM-YSZ cathode was performed and compared to results from FIB-SEM serial section imaging of the same bulk material using energy-selected backscatter detection. The FIB-SEM imaging was performed by collaborators at EPFL, while I performed the subsequent image processing and characterization. Results from the two imaging methods were compared by Nelson *et al.* to validate measurements, and good agreement was found, providing confidence in each of the imaging techniques.[31] Additional discussion of the LSM-YSZ nanotomography imaging and characterization can also be found in [75].

2.2. Full Field X-ray Absorption Near-Edge Spectroscopy (XANES)

The tunable nature of the synchrotron beam permits the simultaneous acquisition of structural and chemical information. In the previous section this was discussed through the use of absorption edge contrast imaging. To review, in some instances absorption contrast can be found in multiphase materials at a single energy level due to substantial differences in density (and therefore x-ray attenuation, as the two are closely correlated) of the various phases. When this is the case, performing imaging at a single selected energy level may be sufficient to map the phases and structures contained in the sample. However, for the general case of a multiphase

composite, it is beneficial to perform absorption edge imaging by operating the microscope below and above an absorption edge of a constituent element and observe locations in the sample which exhibit contrast change, thus denoting the presence of that element. Such an approach can be repeated for multiple elements, corresponding to multiple phases of the material, and provide mapping capabilities for each phase provided an absorption edge of each of the primary elements can be accessed by the microscope.

While absorption contrast imaging can provide elemental mapping, it is difficult to obtain chemical information regarding the specific state of that element. This has motivated the development of full-field x-ray absorption near edge spectroscopy (XANES) imaging in this work. XANES spectroscopy is concerned with the absorption behavior of a material in the immediate vicinity of an absorption edge, typically about +/-50 eV. In this region, the absorption spectrum is specific to the chemical state and can display certain characteristic features which can be used as a fingerprinting method to identify a certain composition. If x-ray tomography imaging is then performed at specific energy levels at which these spectral features occur, the results can provide insights into whether and where different chemical compositions containing the same element exist within a sample. In this manner, x-ray tomography coupled with XANES spectroscopy can be thought of as a highly specialized form of absorption contrast imaging targeting the absorption changes occurring over a range of energy levels in a very well defined fashion around the element's absorption edge.

To apply this methodology to a real sample typically requires some knowledge of the expected compositions in the sample. This can typically be estimated by the researcher based on the nominal composition of the material, its function, its exposure or operating conditions, as well as any preliminary pilot studies concerned with examining the composition. The sample

can then be examined using XANES TXM to determine if it contains any of these possible "candidate" compositions. This concept will be demonstrated in this section using two example systems. One contains nickel foil and nickel oxide (NiO) powder, and another contains nickel foil and nickel subsulfide (Ni_3S_2) powder.

The study of each is primarily motivated by degradation processes in solid oxide fuel cells. In the case of nickel oxidation, the reduction-oxidation cycling of nickel-based oxides also has implications for the performance of lithium-ion battery cathodes and nickel oxide supercapacitors.[43,76-82] In the fuel cell field, nickel is still used as the most common catalyst and electron-conducting phase in SOFC anodes due to its relatively low cost, high catalytic activity, tolerance to carbon monoxide, and ability to serve as a structural support. However, nickel oxidation is a serious problem and can lead to rapid degradation and cell failure under certain exposure conditions. This can occur by the accidental introduction of oxygen (air) during cell start-up or shut-down, imperfect sealing of cell components, or high O^{2-} concentration occurring at fuel-depleted regions in the vicinity of the triple phase boundary. The oxidation process is accompanied by a volumetric expansion on the order of 70%, generating significant stress within the structure and creating mechanical failure.

Similarly to nickel oxides, nickel sulfide compounds have applications in several fields in addition to SOFCs. For example, nano-scale nickel sulfide compounds have recently received attention as an attractive cathode material in lithium ion batteries due to their high theoretical capacity.[83-86] Sodium batteries have made use of nickel sulfide phases as well, due to low cost, long life cycle, and good performance.[87,88] Solar cells have also seen recent advances due to the development of new fabrication techniques involving nano-scale structures replacing traditional, expensive platinum counter electrodes.[89] On the other hand, the presence of

undesirable contaminants in a system, even in concentrations in the ppm level, can often result in the formation of new solid phases within the microstructure, creating a poisoning effect. In particular, many chemical and electrochemical energy conversion systems suffer from sulfur poisoning of catalyst materials by the formation of solid sulfur-containing phases, leading to a decrease in the number of active sites. Such poisoning may occur for contaminant concentrations as low as 1 to 10 ppm.[90-94] Due to its effects on performance, this poisoning phenomenon has received significant attention in a number of fields, including the reformation of tar resulting from biomass gasification,[95,96] automobile storage-reduction catalytic converters for the reformation of NO_x,[97,98] treatment of unburned exhaust methane from natural gas power systems,[98,99] steam reformation of liquid hydrocarbons,[100,101] and electrochemical oxidation of readily available fuels in SOFCs. While the high operating temperature and fuel flexibility of SOFCs allow for cost-effective and energy efficient conversion of hydrocarbon fuels (such as natural gas, anaerobic digesters, or syngas), the presence of sulfur-containing compounds in these fuels may occur due to propagation from the feedstock material/gas or by its introduction as an odorant. Although some work has been done to enhance the tolerance of SOFC anode materials to sulfur poisoning,[102-105] sulfur is still a widely recognized poisoning agent for the commonly used Ni-based anodes. Further discussion of sulfur poisoning is presented in section 3.2.

2.2.1. Two-Dimensional XANES

The following discussion is based on work published in [106]. Full-field XANES spectroscopy can be performed in 2-D to obtain absorption spectra of known compounds as a calibration measure. This was done on two separate occasions for the systems described above.

For the Ni/NiO system, 2.54 μm thick Ni foil (99.95% pure) was obtained commercially from Alfa Aesar and NiO powder (99.99% pure) with 0.5-1.5 μm particle size was obtained from Fuel Cell Materials. A small section of Ni foil was cut from the stock material and glued to the tip of a pin, while the powder was mounted separately using x-ray transparent Kapton tape. The samples were mounted one at a time in the TXM at SSRL and used to collect XANES spectra. This was done by adjusting the incident x-ray energy between 8250 and 8600 eV and collecting a projection image as well as a background image at each step, each with a 0.5 second exposure. Different energy step sizes were used for different regions of the spectra. Very fine step sizes were used (0.5 or 1 eV) in the immediate vicinity of the absorption edge, while larger steps (2 or 5 eV) were used in the pre-edge and post-edge regions. Scripting capabilities developed by the staff at SSRL have enabled automation of the entire data collection process (including image collection, energy adjustments, and zone plate movement to maintain sample focus). The result of the imaging process is a set of projection images and a corresponding set of background images. For each energy, the background image is used to correct the projection image, creating an optical density image. The spectra can then be constructed by examining the absorption of the material as a function of energy level. This can be done by selecting a common region of interest containing the material in each image, or by spatially registering the images and using the total absorption across the entire field of view. The absorption values are normalized by the pre-edge and post-edge regions as is standard practice. Results are shown in Fig. 11 for Ni and NiO reference materials over a range of 8300 eV to 8480 eV. I would like to acknowledge Florian Meirer for his help processing the images to generate the spectra. Processing of TXM XANES data, as well as a variety of other TXM results, is easily performed using the software tool “TXM Wizard” developed by the beamline staff at SSRL.[59]

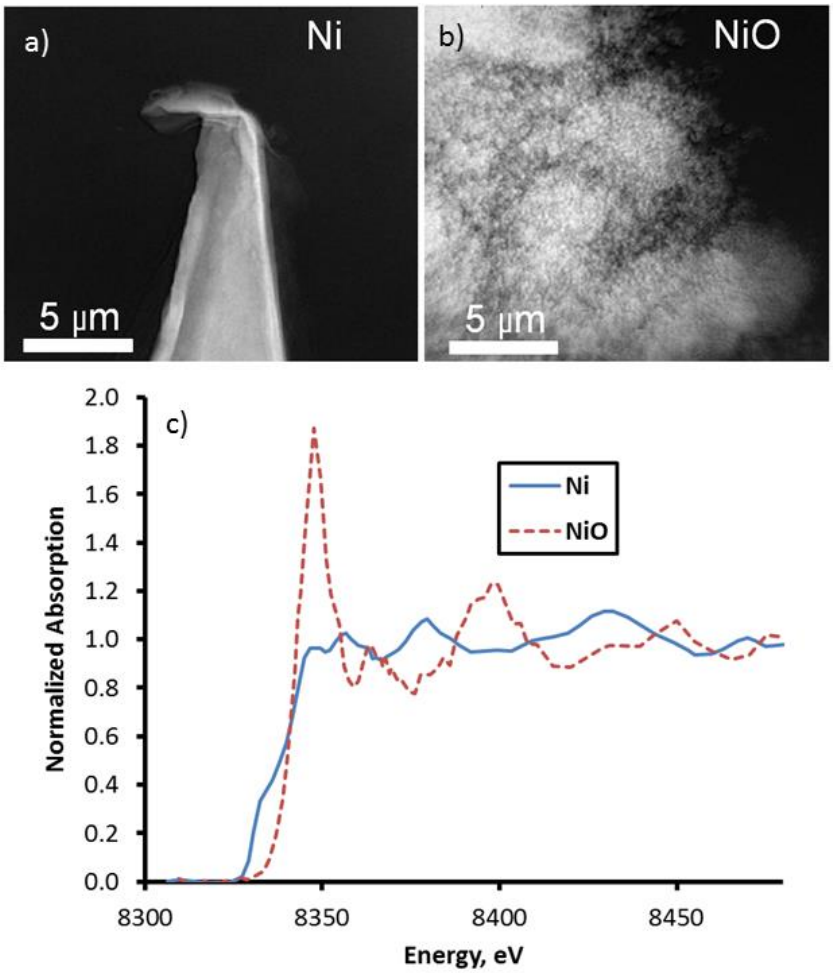

Figure 11: Full field TXM XANES of Ni and NiO. Reference samples of Ni foil (a) and NiO powder (b) are imaged over a range of energy levels spanning the Ni K-edge. Changes in absorption are used to construct absorption spectra of each composition (c).

The XANES spectra of Ni and NiO display distinctly different features close to the nickel K-edge. Specifically, NiO has a large peak at about 8348 eV on the upper end of the absorption edge, while no such distinct peak is noticed for Ni. There are also some lesser differences and minor peaks in the post-edge region, but none as large as the so-called "white line peak". This peak serves as a helpful distinguishing feature for these two chemical species.

A similar procedure was followed for comparing the spectra of Ni and Ni_3S_2, which was performed on the TXM at APS. The discussion of these materials is based on work published in [107]. A Ni foil sample was prepared in the same manner as described above. The Ni_3S_2 powder (99.7% pure, Sigma-Aldrich, St. Louis, MO) was produced from 150 mesh powder which was ground to produce a finer powder and then deposited on a copper transmission electron microscope grid for mounting in the TXM. The TXM was used to obtain images of each sample at energy levels between 8325 eV and 8354 eV, at 1 eV increments and with an exposure time of three seconds. A somewhat smaller range of energy levels was covered in this study due to the lack of automated data collection, leading to substantially more time-consuming data acquisition. In addition, the absorption characteristics of Ni and Ni_3S_2 are not particularly distinguishable when comparing the two materials far below or above the Ni K-edge.[52,108] The images were processed in the same manner, and the resultant spectra were normalized by their endpoints (representing below- and above-edge regions) as shown in Fig. 12. (figure from[107])

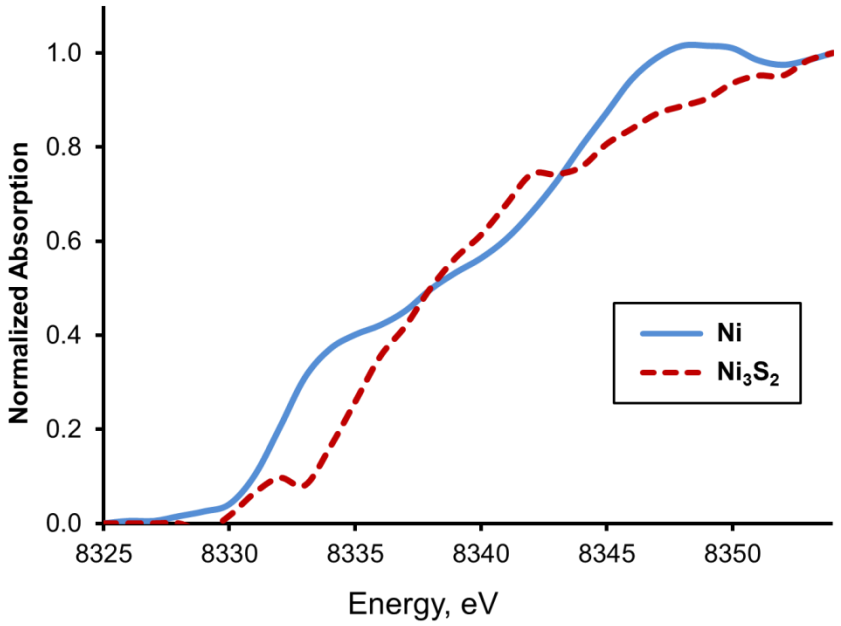

Figure 12: XANES spectra of Ni and Ni_3S_2, measured using full field TXM XANES. Figure adapted from [107]

In contrast to the Ni and NiO spectra, the comparison of Ni and Ni_3S_2 in Fig. 12 is much more subtle. The difference in the two compositions is only minor changes in inflection of the spectra across the edge jump region. This pre-edge structure of the Ni-S species is attributed to electronic transition from 1s to 3d.[109] Ideally, sulfur species could also be examined through use of the sulfur K-edge at 2.47 keV. However, this is not practical experimentally for two reasons. First, for any real sample where sulfur species are contained within a higher density matrix of other material (as in Ni/YSZ of an SOFC anode), the low energy of the sulfur edge prevents the possibility of obtaining any useful transmission signal from a real sample. At that energy, attenuation lengths of the denser materials would be on the order of a single micron, which equates to a sample size too small to provide any practical results. Secondly, the beamline optics are not able to access the sulfur energy because of limitations in the instrumentation. Consequently the sulfur composition can only be measured indirectly via Ni by its XANES spectra. In this study, the Ni speciation is identified using the pre-edge contrast in this spectral region.

Two dimensional TXM projection images can also be used to examine composite samples consisting of multiple phases. Demonstrations of this approach can be found in Nelson *et al.* and Meirer *et al.* [106,110]. Development of a new *in situ* imaging technique has also utilized this approach to examine nickel oxidation processes in real time using the TXM.[43] When multiple phases exist, any given spot in the projection image can contain a contribution from one or more of the phases. Therefore, XANES spectra collected on a local scale at various

locations of the sample will give different results depending on the composition of the sample at that location. This is shown in Fig. 13, which is adapted from a cited work [106] based on data collected at APS using the same procedure described above. (I would like to acknowledge the co-authors of this work for their contributions to the analysis of the data used in this figure.) Projection images at several selected energy levels are used to demonstrate the contrast change of the two phases across the Ni K-edge (darker regions represent higher attenuation). While location B contains NiO only, location A contains mostly Ni, and location C contains overlap of Ni and NiO. As a result, the XANES spectrum of this region is a linear combination of the spectra of Ni and NiO, as shown by the graph on the left. A similar procedure was used by Meirer *et al.*, where each pixel of the image was evaluated using a least-squares fitting algorithm to known reference spectra to determine the contribution of Ni and NiO phases to the total absorption value. [110] The authors were then able to create a phase map of the spatial distribution of Ni and NiO phases across the entire field of view.

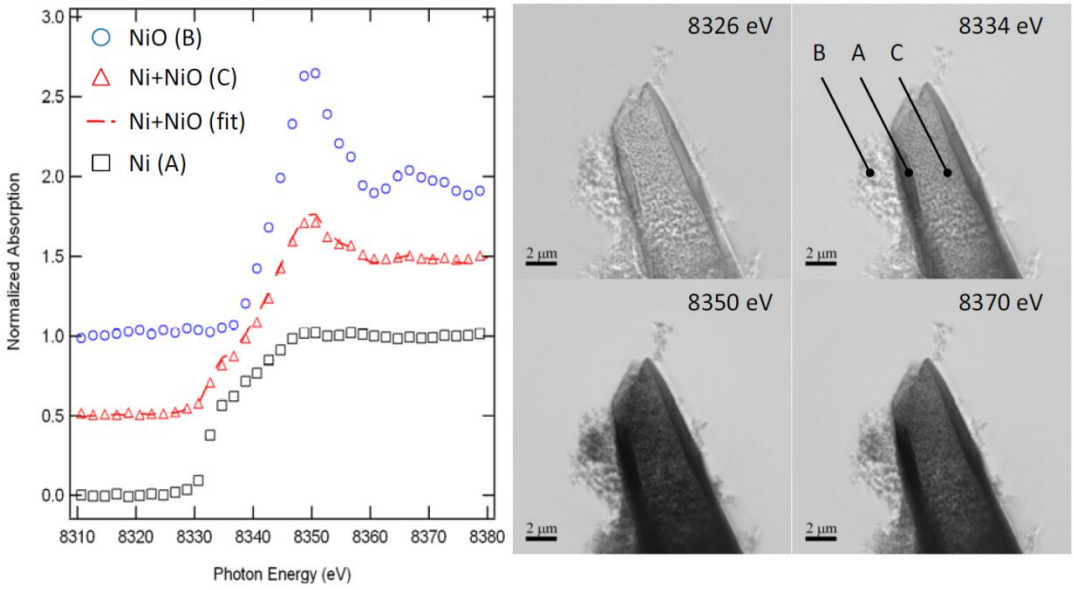

Figure 13: Full field TXM XANES of a composite sample containing Ni and NiO. Measurements of local absorption change are used to reveal regions containing mostly Ni (A), NiO (B), and a mixture of the two (C). Figure adapted from [106].

2.2.2. Extension to Three Dimensional XANES

The information obtained from the 2-D XANES studies can be used to help guide work in 3-D. While 2-D data collection involves only examining the sample from a single orientation, obtaining 3-D data requires performing tomography, involving repeated exposures of the sample from a large number of incident angles, frequently numbering in the hundreds. Therefore, there is an incredible increase in experimental time (as well as complexity) when transitioning from 2-D to 3-D data collection.

In this work, once reference spectra were generated for each of the individual components of the Ni/NiO and Ni/Ni_3S_2 systems, composite samples were created by dipping the metallic Ni into the powder and allowing the powder to cling on by static forces. The resulting Ni/NiO sample was analyzed at SSRL, and the Ni/Ni_3S_2 sample at APS. In each case, knowledge of the XANES spectra of the individual constituent phases guides the selection of certain energy levels at which to perform tomography. For samples consisting of two phases, there are two unknowns: the spatial distribution of each of the phases. Therefore, a minimum of two "equations" are required to solve for the unknowns. The "equations" are provided by imaging at multiple energy levels. These energy levels can be selected based on the spectra shown in Figs. 11 and 12, and should be chosen as to have the maximum possible difference in absorption behavior for the two different phases.

Tomography of the composite sample is then performed at each of the two energy levels. In this study, imaging was performed at 8348 and 8358 eV for the Ni/NiO system. For the Ni/Ni_3S_2 system, imaging was performed at 8334 and 8341 eV. Although the phases and energy levels are different, the following discussion applies equally to both samples. This approach separates the solid phases via the projection images at different energy levels prior to any reconstruction. The description of this image processing procedure is taken from my contribution to the supplementary material in Nelson *et al.*[106]

It is helpful to start from the most basic concepts of x-ray attenuation, which will involve some review of material from sections 1 and 2. Reviewing earlier discussion, the x-ray absorption can be expressed in terms of the Beer-Lambert law, Eq. 4, which yields the intensity I for an x-ray beam transmitted a distance, l, through a material.

$$I = I_o e^{-\mu \cdot l} \tag{4}$$

Here, I_o is the incident beam (measured as the background image collected during data acquisition) and μ is the material's x-ray attenuation coefficient. This law can be expressed in terms of the non-dimensional optical density (OD) according to Eq. 5.

$$OD = \mu \cdot l = -\ln\left(I / I_o \right) \tag{5}$$

In this method applied to segment the composite samples, the XANES spectra of each individual species can be calibrated and expressed in terms of the absorption at a given energy level divided by the absorption at a fixed reference energy level. The selection of the fixed reference level is arbitrary. The resulting ratio, Eq. 6, can be calculated over the range of the XANES spectra or just at the specific energy levels of interest used for tomography.

$$C = \frac{OD}{OD_{ref}} = \frac{\mu}{\mu_{ref}} \tag{6}$$

To illustrate the segmentation process for a general case of two hypothetical species, "*A*" and "*B*" will be used to denote the two species. Presumably, a real sample would contain both *A* and *B* in unknown quantities and spatial locations. Nanotomography is performed on this sample at two energy levels of interest identified from the XANES spectra, denoted by superscripts *1* and *2*. The transmission images from the nanotomography data set will undergo background reference correction to convert to an optical density scale, producing a series of sample images over the angular range scanned (e.g., -90^o to 90^o in 1^o increments) for each energy level. The optical density images at each angle are paired, corrected based on magnification to have a consistent pixel size, and spatially registered using a phase correlation algorithm. The following procedure is then applied at each angle pair.

The optical density of each image at the energy levels of interest are known and designated as OD^1 and OD^2. The relative absorption values of the two species at the two energy levels, *C* in Eq. 6, are also known based on XANES spectra previously collected on the individual species. Extending Eq. 5 to the case where there is an arbitrary amount of each species, the optical density at each energy level can be determined.

$$OD^1 = \mu_A^1 \cdot l_A + \mu_B^1 \cdot l_B \tag{7}$$

$$OD^2 = \mu_A^2 \cdot l_A + \mu_B^2 \cdot l_B \tag{8}$$

Using Eq. 6, the absorption coefficients in Eqs. 7 and 8 can be expressed in terms of the absorption ratio, *C*, and the value of the absorption coefficient at the reference energy level.

$$OD^1 = \mu_A^{ref} \cdot l_A \cdot C_A^1 + \mu_B^{ref} \cdot l_B \cdot C_B^1 \tag{9}$$

$$OD^2 = \mu_A^{ref} \cdot l_A \cdot C_A^2 + \mu_B^{ref} \cdot l_B \cdot C_B^2 \tag{10}$$

The reference absorption coefficient and the length can be grouped together for each material by defining

$$A = \mu_A^{ref} \cdot l_A \tag{11}$$

$$B = \mu_B^{ref} \cdot l_B \tag{12}$$

Expressing Eqs. 9 and 10 in this way provides a system of two equations and two unknowns that can be readily solved for *A* and *B*. These two unknowns represent the images that identify the two materials. They can be calculated based on the known values of absorption ratios and the original images of the total sample at the two different energy levels. These *A* and *B* images are calculated for every angle pair, resulting in two volumetric data sets, one corresponding to each species, as shown in Eqs. 13 and 14.

$$A = \frac{\left[OD^1 - \frac{C_B^1}{C_B^2} OD^2 \right]}{\left[C_A^1 - \frac{C_B^1}{C_B^2} C_A^2 \right]} \tag{13}$$

$$B = \frac{\left[OD^2 - \frac{C_A^2}{C_A^1} OD^1 \right]}{\left[C_B^2 - \frac{C_A^2}{C_A^1} C_B^1 \right]} \tag{14}$$

Implementation of the procedure above is demonstrated in Fig. 14. Fig. 14 (a) and (b) display optical density images of the Ni/NiO sample from a single angle at 8348 and 8358 eV. Panels (a) and (b) represent OD^1 and OD^2 in the notation above. The "C" ratios are determined

directly from the Ni and NiO XANES spectra depicted in Fig. 11. After applying Eqs. 13 and 14, spatial maps of each of the individual species NiO and Ni (A and B in the general notation) are shown in Fig. 14 (c) and (d). Similar images are obtained at every projection angle.

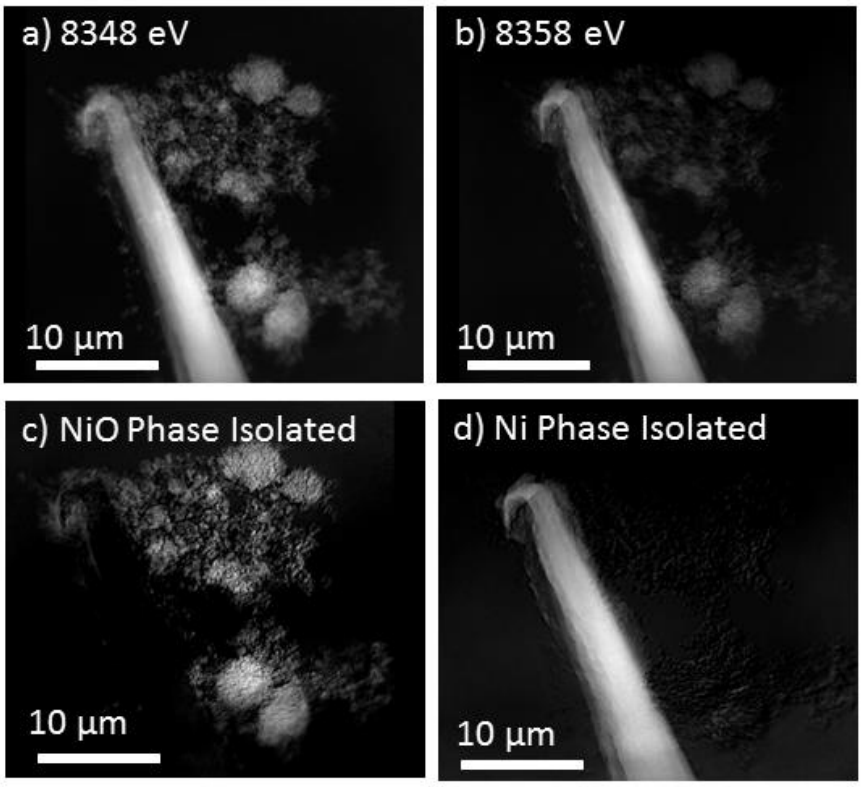

Figure 14: Implementation of full field XANES for 3-D imaging of a two-phase sample. In this demonstration, known contrast in projection images collected at certain energy levels (a and b) is used to isolate NiO (c) and Ni (d) phases.

Each of the angular sets belonging to the two species is reconstructed separately, using the iterative reconstruction algorithm.[55] A similar approach for separate reconstruction of the phase maps of different species has been used by Meirer *et al.* [110,111] The data resulting from the reconstructions is then overlaid to reveal the positions and amount of the two species in the

sample. Results are shown in Fig. 15 for the Ni/NiO as well as Ni/Ni_3S_2 systems. Figures have been adapted from Nelson et al. and Harris et al. [106,107].

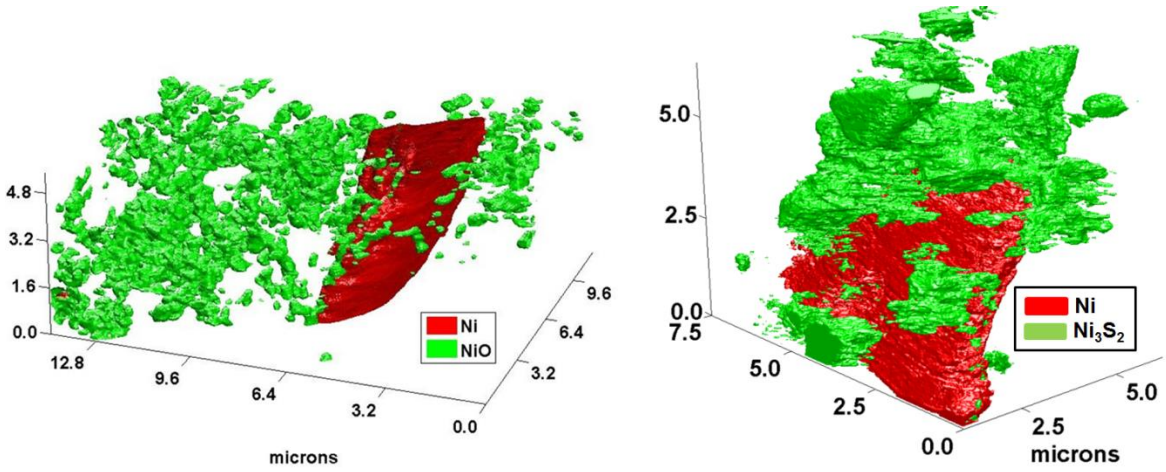

Figure 15: 3-D renderings of the Ni/NiO sample (left), and Ni/Ni_3S_2 sample (right). Figures adapted from [106,107]

2.2.3. 3-D XANES for Real Samples

The procedure described above manipulates the optical density images at each angle before reconstructing separate phase maps of each of the species in the sample. The mathematical description, which was presented in terms of two species and therefore two unknowns, can be readily extended to any number of possible species provided their absorption behavior is both known and sufficiently unique. (Two species with vary similar XANES spectra, such as NiO and Ni_2O_3, would not be distinguishable using this method). To test this approach, a sample was created with three species by adding some NiO powder to a Ni/YSZ anode sample affixed to the tip of a pin. Several NiO particles were manually added to the sample with the aid of an optical microscope. Tomography was performed at NSLS at the following energy levels: 8300, 8348, and 8375 eV. A minimum of three energy levels are needed to satisfy the three unknown species, and the energy levels were chosen to highlight different absorption behavior of

the three species. The differences in Ni and NiO are the same as described above for the Ni/NiO system (imaging performed at 8375 eV provides similar results to imaging at 8358 eV), and the absorption behavior of YSZ is constant across the Ni K-edge, as it contains no nickel. Example images at a single angle are presented in Fig. 16, where (a)-(c) show the optical density images and (d)-(f) show each of the three species maps. One of the NiO powder particles is labeled by a white arrow in (b) and (c). As expected, both Ni and NiO have substantial increases in absorption moving from below (8300 eV) to above (8348 and 8375 eV), but NiO also shows a decrease in absorption between its white line peak at 8348 eV and the post-edge at 8375 eV.

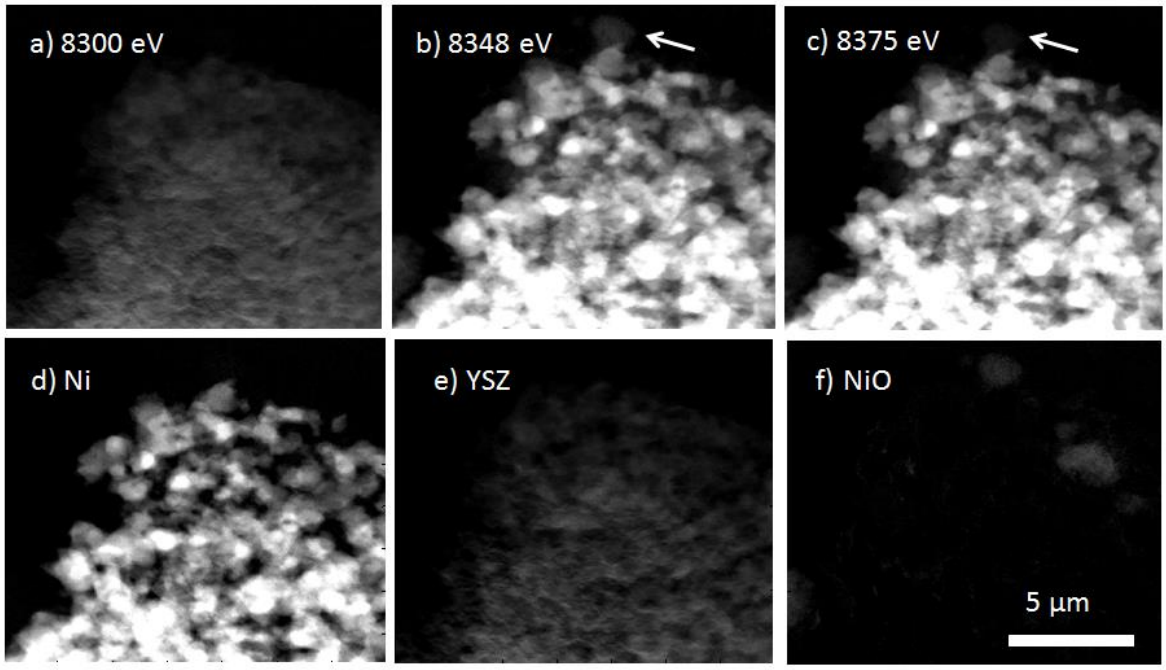

Figure 16: 3-D XANES imaging of a Ni-YSZ sample with added NiO powder. Imaging at 3 selected energy levels (a-c) permits isolation of each of the solid phases (d-f).

Despite the results presented in Fig. 16, producing and reconstructing separate phase maps for 3 or more phases in 3-D is currently complicated by microscope sensitivity, stability,

and signal to noise ratio. The theoretical development and mathematics are quite straightforward as discussed above, but the implementation of the approach is rather unreliable with current instrumentation. The quality of the isolation of the phases at all angles is not consistent as beam intensity and stability changes over the long duration of the experiment, which creates significant complications for 3-D reconstruction. An attempt of the method was performed, and the results of reconstructing the phase maps of Ni, YSZ, and NiO are shown in Fig. 17. A single cross sectional slice of the reconstructed data from the same location is shown for each phase. The spatial distribution of the Ni and YSZ phases appears to be captured fairly well. However, the NiO particle on the side of the sample is barely visible in the reconstruction, and could easily be confused with an artifact or noise. There are several reasons for this issue. First, the very fine and highly irregular geometry of the powder particles makes the algorithm incredibly sensitive to image alignment and noise problems when comparing the data sets at the three different energy levels. Although this was an issue to a lesser extent in the 2-phase Ni/NiO and Ni/Ni_3S_2 samples described previously, the introduction of a third variable (YSZ) in the current application confounds the issue. Secondly, the NiO is fairly weakly absorbing at all energy levels, including even its white line peak at 8348 eV. This means the signal it generates (the fraction of photons transmitted versus attenuated) is weak, especially at 8300 and 8375 eV, further enhancing the effects of noise. Lastly, beam stability can be an issue when attempting to correlate tomography data that was collected over the time scale of an entire day. Each tomography took several hours to acquire, which means there is substantial time between the background reference image collected prior to the tomography and some of the projection images comprising the tomography itself. As is typical with synchrotron beamlines, the beam can “drift”, meaning that the beam’s illumination of the field of view can slowly change over time (a time scale of minutes to hours).

This is especially apparent for the small field of view and fine resolution used in synchrotron nanotomography. The result of this drift is the introduction of additional noise to the data after the background has been used to correct the projection images. Ordinarily, this is not a substantial problem because the process of reconstructing a single tomography data set can "wash out" this noise as the overall signal obtained from the many angular exposures is much greater than the level of noise. However, the methodology presented above to isolate multiple phases from projection images occurs prior to reconstruction, and is very sensitive to noise at each projection angle, especially for regions which have low signal to begin with (such as NiO). This effect can possibly be mitigated by collecting background images immediately before or after each projection image, or averaging multiple images to improve the signal to noise ratio especially for weakly absorbing phases. Some of these capabilities have very recently been made available by the team at SSRL using the TXM Wizard software, but they require access to the scripting capabilities specific to their system and have not yet been tested at this time for these material applications. As a side note, the SSRL team has had success with generating and reconstructing separate elemental maps for one element at a time using below- and above-edge absorption contrast imaging, and is working towards obtaining results using the XANES approach for three or more chemical species (containing the same element) at a time. [111,112] This represents a future opportunity with potentially significant benefits in the 3-D imaging field.

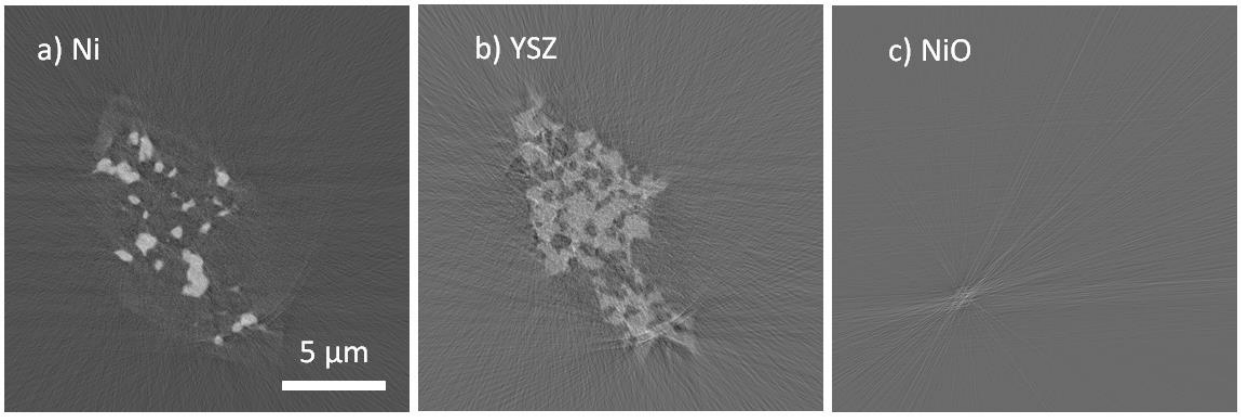

Figure 17: Reconstruction of Ni (a), YSZ (b), and NiO (c) phase maps. The small and weakly-attenuating NiO particle does not provide adequate and consistent signal at all projection angles, and as a result produces a very poor reconstruction.

An alternative approach is to reconstruct the tomography data sets at each energy level (without applying Eqs. 6-14) and then compare the results fo the reconstructed 3-D data. This was done using the same Ni/YSZ/NiO sample in a paper co-authored with the staff at NSLS.[113] With this approach, the results of the reconstruction are used to evaluate the spatial distribution of the various phases. Fig. 18, adapted from Chen-Wiegart *et al.*[113], depicts the sample after reconstruction at 8375 eV (a) and the contrast that can be observed in one of the NiO particles (labeled by the red arrow) across the three energy levels, (b)-(d). The contrast change of the NiO is very apparent, and matches the expected behavior displaying a local maximum at the white line peak followed by a decrease in the post-edge. Clearly, the NiO particle is much more visible and accurately represented using this methodology than the previous (which manipulated the optical density images *prior* to reconstruction). The data is not nearly as sensitive to the noise introduced by beam drift and the low signal of the NiO particles. Furthermore, alignment of the 3-D data can be performed after reconstruction (in 3-D using *Affine Registration* module in Avizo, for example) and is easier to visually asses the quality.

Lastly, by comparing the data after reconstruction, it is possible to utilize the contrast that may exist between various phases even at a single energy level. Using the previous method based on manipulating the projection images, this is likely not possible because it is difficult to tell the level of contrast between the different phases in the 2-D projections. However, after reconstruction it may be easier to observe the absorption differences and utilize them to aid in identifying and segmenting phases.

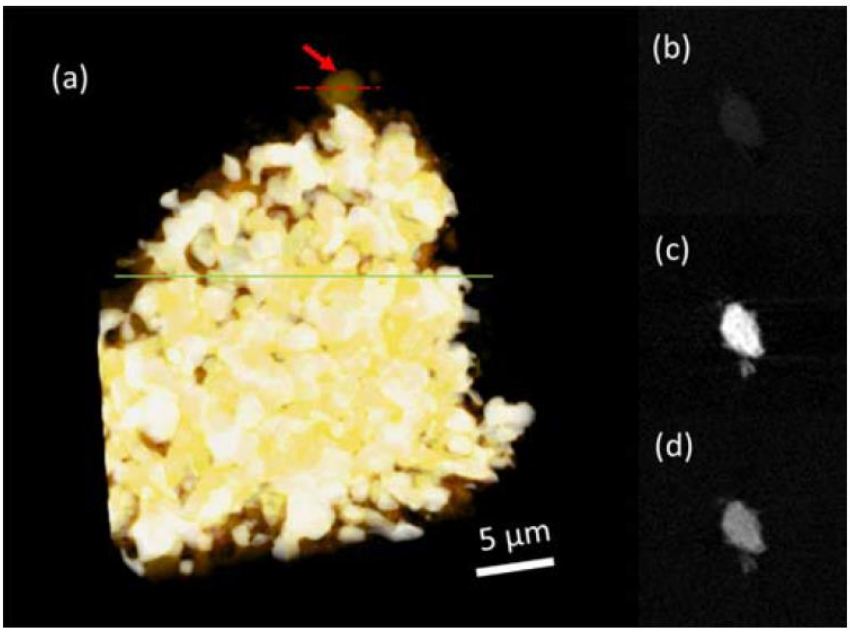

Figure 18: Reconstruction of the same Ni-YSZ and NiO powder sample. By first reconstructing the data from the tomography of each energy level, and comparing results after reconstruction, it is much easier to observe the NiO particle and its expected contrast change, as shown at 8300 (b), 8348 (c), and 8375 eV (d). Figure from [113].

3. Microstructural Evaluation of Heterogeneous Functional Materials

The following sections apply the x-ray imaging techniques to several real materials of use in energy systems:

- An intermediate-temperature solid oxide fuel cell cathode
- A Ni-YSZ solid oxide fuel cell anode poisoned by hydrogen sulfide
- A dense dual-phase ceramic oxygen-separation membrane

For each application, the materials share the common connection between microstructure and performance, particularly with regards to changing microstructures due to contamination and reaction/poisoning processes. These processes have in each case created a new phase or phases which were not initially expected, and could have significant implications for the functionality of the material within the larger device. The 3-D x-ray nanotomography methods are applied to gain a deeper insight into these microstructure-performance connections which was not previously available using well-established characterization techniques. However, the exact imaging approach for each material varies, and typically the x-ray measurements are complemented by independent characterization methods, such as electron microscopy. Lastly, despite significant personal contributions to the development and implementation of x-ray nanotomography, input from collaborative teammates, particularly with the secondary characterization techniques, has been welcome and hugely beneficial. I have acknowledged specific instances in which this is the case.

3.1. Neodymium Nickelate SOFC Cathode Contamination

Section 3.1 is in part based on the publishing of this work in [114].

3.1.1. Introduction to Solid Oxide Fuel Cells

Increased demand for clean, energy-efficient power sources has led to substantial research efforts in numerous types of fuel cells, including solid oxide fuel cells (SOFC). One of the most attractive features of fuel cells is the electrochemical oxidation of fuel, which is not restricted by the Carnot limit of heat engine efficiency. The primary components and basic operation of an SOFC are shown in Fig. 19 (adapted from wikipedia.com).

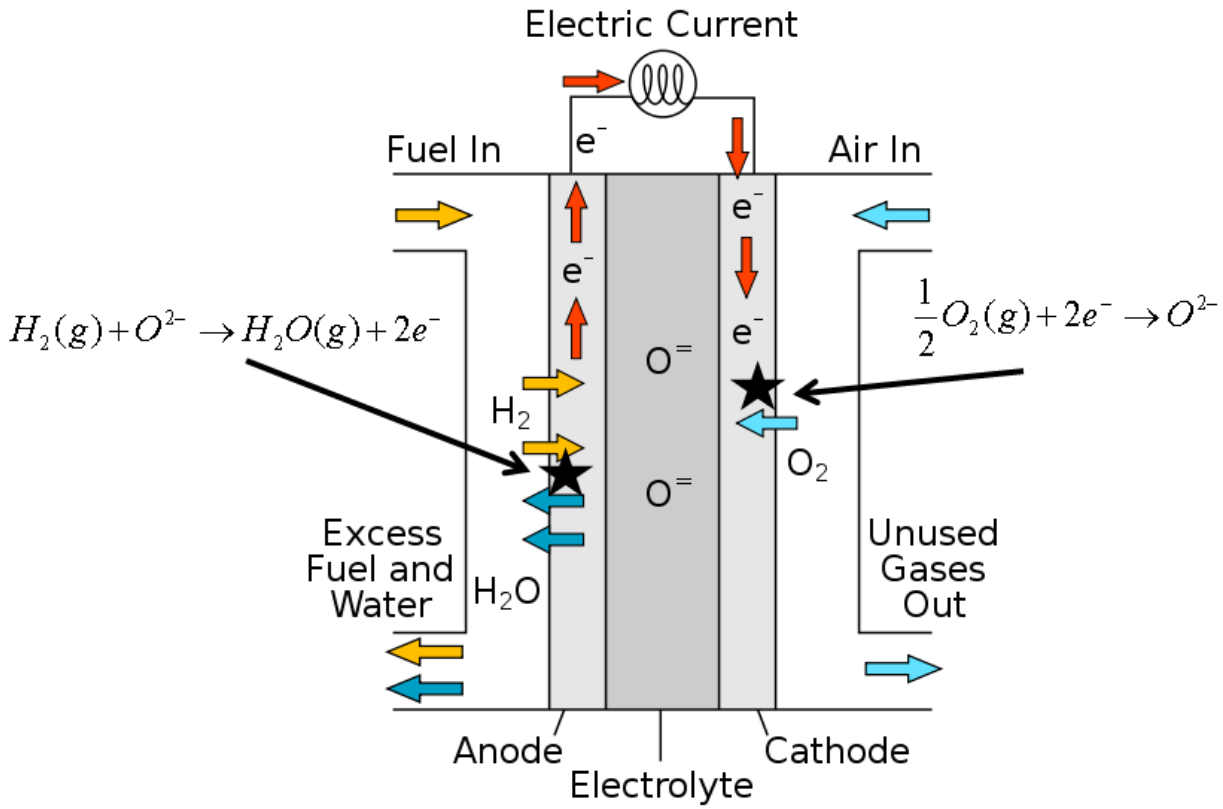

Figure 19: Solid Oxide Fuel Cell structure and operation. Adapted from wikipedia.com.

Fuel entering the anode side is oxidized by oxide ions transported through the electrolyte. The hydrogen oxidation reaction is written on the left. The reaction produces electrons, which travel through an external circuit producing power. On the cathode side, electrons reduce oxygen from the air to produce oxygen ions, which then transport through the electrolyte to complete the circuit. All electrochemical reactions occur at the triple phase boundary (TPB), which is the location where gaseous, ionic, and electronic phases converge, capable of supplying transport pathways for the reactant and product species. The prevalence of these TPB sites dictates the exchange current density of either electrode, and it is desirable for the TPB density to be as large as possible. However, this cannot be done at the expense of severing the percolating networks of the various phases. For a TPB site to be "active" not only must the ionic, electronic, and gaseous phases meet at a single point, but each must be connected to a contiguous network through which charge or mass can move. Therefore, there exist competing effects of optimizing reaction and transport properties within the discrete multi-phase microstructure.

One of numerous variations of fuel cells, the SOFC stands alone as the type with the highest operating temperature, typically 600° to 1000° C. The high temperature is used to promote catalytic behavior of the electrode materials, and enhance kinetic rates of the oxidation and reduction reactions, increasing the device's current density. The improved catalytic behavior also enables fuel-flexible operation, as pure hydrogen is not required at the anode as it is for some other fuel cell types. SOFCs can operate on a number of light hydrocarbon fuels directly through their internal reformation within the anode structure at high temperature.[115-118] These benefits also eliminate the need for expensive noble metal catalysts to be included in the electrode. In addition, the high temperature is necessary to promote ionic conductivity through the solid ceramic electrolyte, which is not sufficiently conductive at lower temperatures.

While the diagram in Fig. 19 depicts the basic operation of an SOFC, in reality it is much more complicated. The electrolyte is a dense, single phase ceramic, but modern state of the art electrodes are typically multi-phase porous composites consisting of discrete ionic and electronic conducting phases. The advantage of this approach is the extension of the electrochemically active TPB region away from the electrode-electrolyte interface and into the electrode structure. Typically this is done by fabricating a rather dense region close to the electrolyte as the electrode functional layer, with low porosity but high TPB density and efficient ionic/electronic transport. Further from the electrolyte is a more porous support layer, with larger pore features more conducive to gas diffusion. The most common composite anode is a cermet (composite consisting of a ceramic and a metal) of nickel and yttria-stabilized zirconia (YSZ). YSZ is also currently the most common electrolyte material. The cathode side usually consists of composite lanthanum strontium manganite (LSM) and YSZ. The Ni and LSM are chosen due to their tolerance to reducing and oxidizing environments, respectively, as well as catalytic behavior and high electronic conductivity.

Research in new materials, as well as methods for mitigating problems with current SOFC materials, is ongoing.[118-122] Particularly due to the high operating temperature, SOFC materials are susceptible to a number of challenges, including:

- Solid contamination and secondary phase formation
- Compatibility issues between various SOFC components
- Mechanical stability
- Coarsening-driven microstructural evolution
- Poisoning processes due to impurities in fuel streams
- Stability in a variety of gas environments (redox cycling)

The result of these challenges is that the microstructure of SOFC components is typically not static, but rather dynamically changing with time and operation depending on the operating conditions, fuel, device cycling, thermal management, etc. The impacts of these various factors on device performance can frequently be traced back to modifications of the microstructural networks, motivating the desire to observe them directly in 3-D to quantify the effects.

3.1.2. Tubular Intermediate Temperature SOFCs

Within the broad and extensive research efforts focused on SOFC development, tubular SOFCs in particular have received attention due to their potential as an alternative power source for small-scale and portable applications. While the planar stack design (of alternating layers of electrodes, electrolyte, and interconnect) remains the common configuration for stationary power, the tubular design has a number of advantages including robustness, fast thermal cycling, simplified sealing, decreased risk of layer delamination, and the ability to fabricate very small geometries.[123] The attractiveness of small geometries has gained recent attention in the modeling world with the movement towards micro-tubular SOFCs.[124,125] In addition to the advantages previously mentioned, the micro-tubular cells offer an additional number of attractive features including rapid cell start-up/shut-down (due to small thermal mass), a high tolerance to cycling and thermal shock, decreased ohmic and concentration transport losses, and increased volumetric power density.[123,126,127] Refinements in micro-tubular SOFC design have been made possible through a number of experimental studies, and have suggested significant improvements in performance are possible based on two design considerations: 1) fabrication of micro-tubular cells based on a cathode support layer, and 2) development of materials suitable for intermediate temperature (IT) operation.[127-133]

Use of cathode supported cells provides several advantages. First, low electronic conductivity of most cathode materials (compared to that of typical anode materials) means cell design can benefit from a thicker cathode and hence increased current collection on the cathode side. In addition, with the cathode providing the structural support for the cell, the anode can be kept thin, which has the duel benefits of shorter gas diffusion pathways (and hence lower concentration losses and higher fuel utilization) as well as improved structural stability. SOFC anodes, particularly those using the common nickel-based cermet composite, are well known to be susceptible to structural degradation due to redox cycling and long-term nickel coarsening at high temperature. The resulting expansion and contraction of the anode structure leads to the development of local stress concentrations, and typically cell failure.[126] The use of a thin anode, enabled by a cathode-supported cell, can help reduce some of these problems. [134]

The motivation for intermediate temperature SOFC operation is due to several potential simplifications in cell operation, including the facilitation of rapid start-up (which has particular benefits for portable power), and alleviation of material stability issues which are exacerbated at high temperature, particularly on the anode side as discussed previously. However, the most significant obstacle in the way of IT-SOFC development is the intrinsically low conductivity of many classic SOFC materials at the lower temperature. For this reason, the development of successful IT-SOFCs will require the consideration of alternative materials.

One such choice for cathode-supported IT-SOFCs is non-stoichiometric Neodymium Nickelate (NNO), $Nd_{1.95}NiO_{4+\delta}$.[135-138] It is of the Ruddlesden-Popper type, and provides mixed ionic-electronic conductivity (MIEC) due to its ability to incorporate excess oxygen ions at interstitial sites.[139-141] An MIEC, which can transport both electrons and oxygen ions, eliminates the need for multi-phase composite electrodes, simplifying the material synthesis and

compatibility considerations, as well as percolation problems that can exist within the composite designs. But different challenges still exist with the NNO material, most notably in cell fabrication during co-sintering of cathode and electrolyte layers. As with any alternative material, compatibility with the remaining cell components is a significant simultaneous constraint along with those of intrinsic performance, and includes issues such as compatibility of thermal expansion coefficient, sintering shrinkage rates, and chemical reactivity. These are areas of ongoing research in the field.[129,142,143]

For the NNO material in particular, additional poisoning processes have been observed which could affect the electrode performance. Electron microscopy work has revealed the presence of silicon and chromium contaminants present in the cathodes following cell operation.[143,144] While the Cr is prescribed to the deposition of volatile Cr species from cell interconnects during actual operation, the Si is likely to have originated from the manufacturing process and was present in the raw material. The cathodes studied in this work were never operated as part of a cell, and therefore Cr is not expected. Other work has reported on the Cr poisoning effects.[144] However the Si was introduced during the synthesis of the raw material by the manufacturer, likely using cost-cutting powder-milling procedures. Previous reports using x-ray diffraction (XRD) and energy-dispersive x-ray spectroscopy (EDS) have shown that the silicon in the raw powder is mostly amorphous due to poor detection using XRD, but exists in roughly the 2-3 atomic percent range as measured by EDS.[143,144] During the fabrication of the NNO cathode, the Si interacts with the primary NNO phase creating a poisoning effect. In this study, the poisoning effect will be observed and characterized using x-ray nanotomography for NNO cathodes which have not yet been operated in a cell. Therefore, the observed structures are solely a result of the fabrication processes rather than any operational degradation. The 3-D

distribution of phases and structures within the cathode is then considered and discussed in terms of the expected implications of the poisoning for cell operation.

3.1.3. Microtubular Nd-Nickelate Cathode Fabrication

The NNO powder used in this work (nominal composition $Nd_{1.95}NiO_{4+\delta}$) was obtained commercially from Marion Technologies. Fabrication of the micro-tubular cathodes was performed by Kerafol (Germany). The powder was mixed with an 18wt% organic additive and sent through a proprietary extrusion process to make the hollow tubes. If the cathode tubes were to be used in an operating cell, they would be co-sintered with an electrolyte layer at 1300°C for 2 hours. Although an electrolyte was not included for this study, the same sintering conditions were used for consistency. The geometry as well as some of the microstructural features of the sintered tubes can be observed in the scanning electron micrographs in Fig. 20 (from [114]). The SEM work was performed by collaborators at Ecole Polytechnique Fédérale de Lausanne (EPFL) who have done extensive work on this material.[142-144] Fig. 20 reveals tubes several hundred microns in wall thickness and about 2 mm in diameter. Porosity throughout the tube wall occurs on a range of length scales, with generally very fine pores near the inner and outer surfaces (Fig. 20(c)) and larger macro-pores in the interior.

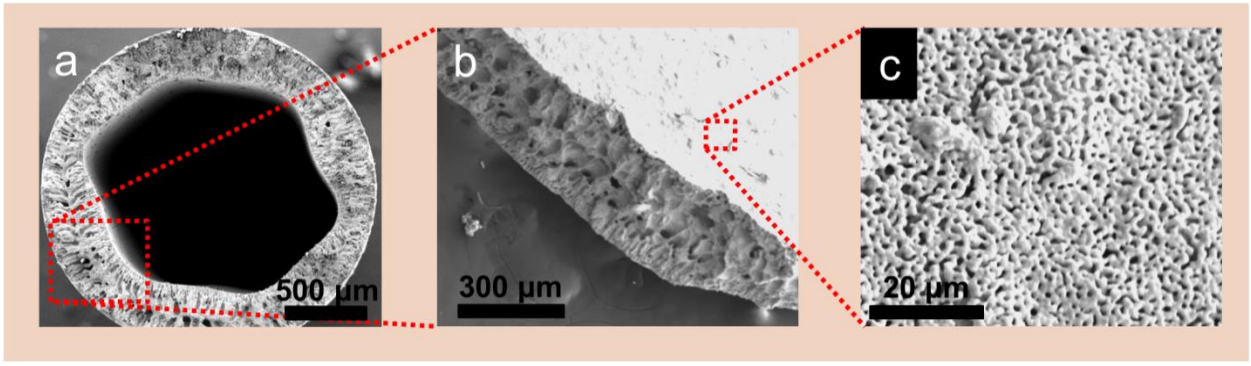

Figure 20: SEM micrographs. a). SEM micrograph of fractured extruded Nd-Nickelate tube. b). Fractured wall of NNO tube, showing macro-pores within tube, as well as the interior surface of the tube. Sample 1 was taken from the interior surface (visible in figure), and sample 2 was taken from the exterior surface (not visible). c). A close-up view of the NNO surface, from which cylindrical samples for X-ray nanotomography were extracted using FIB-SEM. Figure from [114].

3.1.4. X-ray Nanotomography Imaging

Two samples were prepared using FIB-SEM milling (which was performed by lab-mate Jeff Lombardo). One sample each was taken from the interior and exterior surface of an NNO tube, where generally small pores are observed. Because the samples had not been previously examined using transmission x-ray techniques, the attenuation length of the material was not known with certainty. To this end, the samples were created with two different sizes to improve the likelihood that reasonable transmission signal could be obtained for at least one of the samples. Sample 1 was taken from the interior surface of the tube and was taken as a cylinder of approximately 6 micron diameter. Sample 2 was approximately 9 microns in diameter and was taken from the outer surface of the tube. (During imaging, it was found that both cylinders were of reasonable size to provide good signal, and therefore the preparation of differently sized cylinders was a non-issue). After milling, each cylinder was mounted vertically on the tip of a stainless steel pin and gold particles were added as fiducial markers.

The first x-ray nanotomography experiments were performed on NNO at SSRL. Because the magnitude and composition of any possible poisoning phases was not initially known, an incident beam energy of 8360 eV was used. This energy is just above the Ni K-edge (defined at

8333 eV) and was chosen to provide strongly-absorbing behavior of Ni-containing species. Tomography was performed by collecting 181 projection images, at angular steps of 1° between -90° and +90°, using an exposure time of 0.5 seconds. The zone plate had an outer-most zone width providing 30 nm spatial resolution. The projection images were aligned using the gold fiducial markers and reconstructed using a filtered back projection algorithm. The resulting images revealed what appeared to be two solid phases (plus pore space). While one of the phases was suspected to be the primary NNO phase, the composition of the other was not known. Prior work by collaborators at EPFL had suggested the possible presence of both Si-based (silicate) as well as NiO phases, however these were not distinguishable using the single tomography data as their absorption behavior was similar and provided no contrast.

To investigate the structure and composition further, additional imaging was performed at a future date at NSLS. In this second experimental run, tomography was performed both above (8400 eV) and below (8300 eV) the Ni K-edge. For data collection, the same 181 projection images were collected and with a zone plate providing the same 30 nm resolution. However, the lower flux provided by the NSLS required the use of 50 second exposures to obtain a similar signal as at SSRL. An example optical density image of sample 1, shown in Fig. 21(a), is taken from the above-edge data set and shows the NNO cylinder, Pt remaining from the sample preparation, and the gold particles used as markers. Both of the data sets for both samples were reconstructed using filtered back-projection. The 3-D data that results from the reconstructions can be used for comparison of below- and above-edge. Representative cross sections from sample 1 are shown in Fig. 21 (b) and (c). Fig. 21(b) shows an above-edge image, and is comparable to the data obtained at SSRL. Two shades of gray, representing two solid phases, are clearly apparent in addition to the dark background representing void space. The equivalent

below-edge image of the same region is shown in Fig. 21(c). Red circles are used to highlight regions with substantial contrast change across the absorption edge. NiO, an expected secondary phase based on previous reports, contains high Ni content and would be expected to display such a drastic change. Therefore, these regions are prescribed to the NiO phase. From Fig. 21(c), two other phases exist. The bright phase is prescribed to the primary NNO phase due to its high density (and therefore high x-ray absorption and brighter shade), while the remaining darker gray is concluded to be a silicate phase. Note, the silicate phase can be differentiated from the NiO by the fact that it does not contain Ni, and therefore appears the same shade of gray at both energy levels.

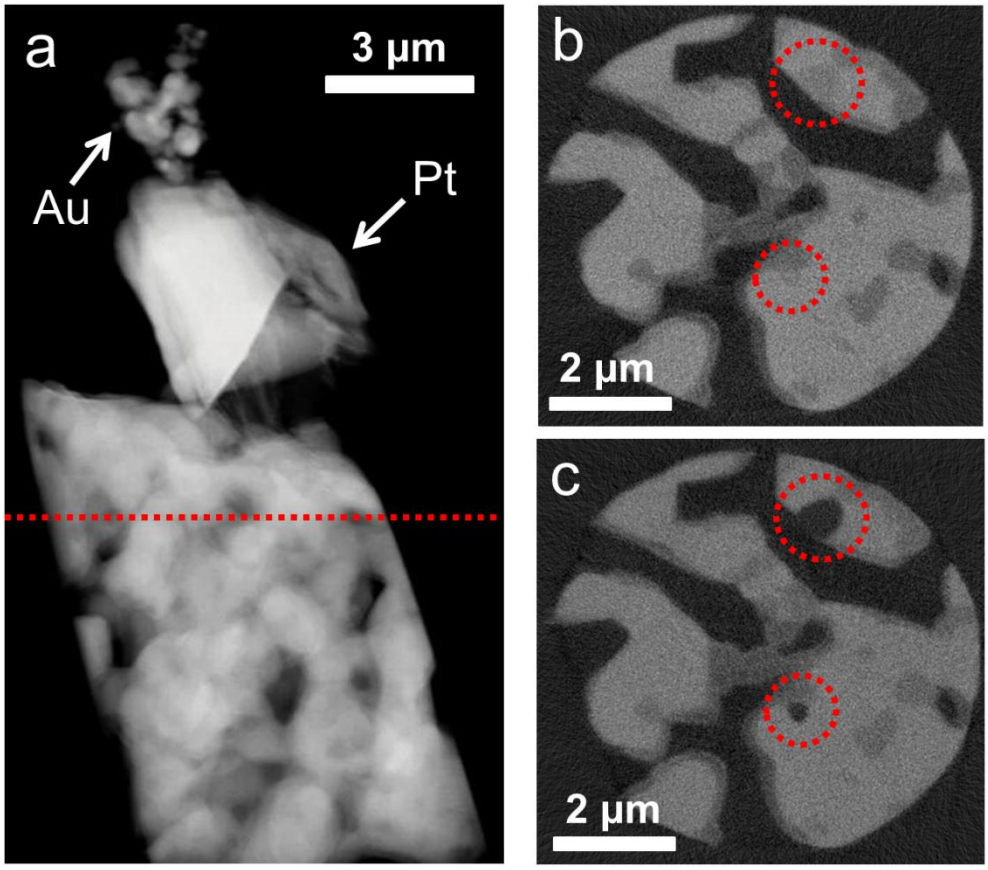

Figure 21: X-ray nanotomography of Nd-Nickelate material. a) Absorption-mode image of an NNO cylinder produced by FIB milling. Notice platinum on top of cylinder remaining from sample preparation procedure, and Au particles placed on top as fiducial markers for use in

image alignment. The red dotted line denotes the location of the cross section shown in images b and c. b) An example cross section of the reconstructed sample, imaged above the Ni K-edge, 8400 eV. c) The same cross section, taken from the below-edge data set, 8300 eV. The red circles show regions of contrast between the two data sets, attributed to the NiO phase. Other phases are pore: black, silicate: dark gray, NNO: light gray. Figure from [114].

The reconstructed data sets (two data sets for each of the two samples) were processed in the following manner. The above- and below-edge data for each sample were spatially aligned to one another using a phase correlation registration algorithm. Image subtraction was performed by subtracting the below-edge data from the above-edge data on a pixel-by-pixel basis. The image subtraction revealed all locations of NiO. The subtracted data was then added back to the above-edge data to create a single 3-D map for each of the 2 samples. The maps each contained 4 shades of gray corresponding to the three solid phases plus pore, as shown in Fig. 22(a). Some minor filtering was used to smooth the data and remove noisy pixels, and the data was then segmented using a watershed algorithm. The result of the segmentation with the various phases labeled is shown in Fig. 22(b). Because the image processing was all performed in 3-D, and with no preference to direction on the voxel grid, the full 3-D segmented structure can also be observed as shown in Fig. 22(c). The segmented data for each sample was then cropped in preparation for quantitative analysis. To keep as much of the data as possible, yet omit the surrounding void space not physically a part of the sample, the cropping was performed using an oblique cylindrical volume tightly conforming to the actual geometry of the cylindrical sample. The total volume of each sample contained within the cropped structures was 201 μm^3 for sample 1 and 313 μm^3 for sample 2.

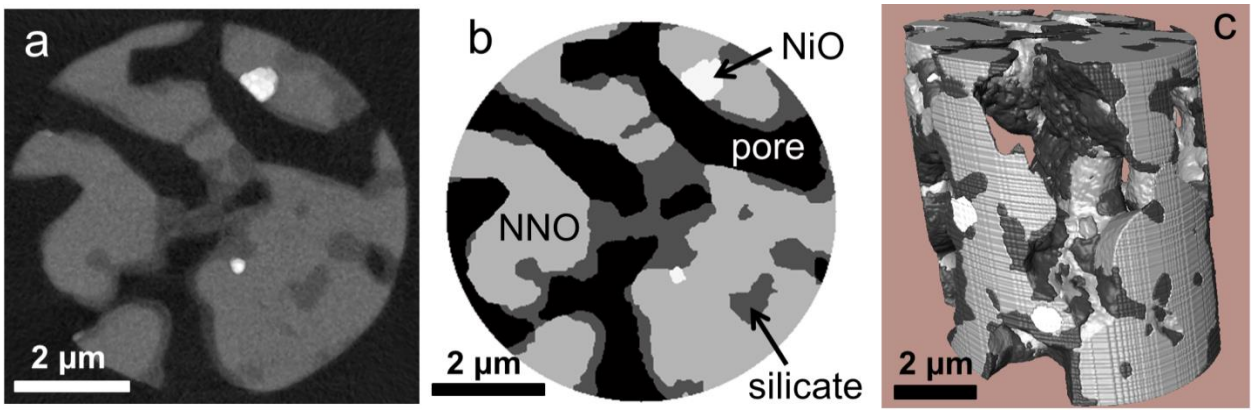

Figure 22: Digital image processing. a) The same region from Figure 21, with the data above (Fig. 21(b)) and below (Fig. 21(c)) the Ni K-edge combined to identify the four phases (three solid plus pore) by differences in grayscale value. b) The same cross section of the sample after using watershed segmentation to identify the phases. NNO: light gray, silicate: dark gray, NiO: white, and pore: black. (Note: the cylinder has been cropped slightly in figure b to simplify subsequent processing and characterization steps). c) A 3D rendering of the segmented full cylindrical sample. This type of data can be used as input to microstructural characterization routines. The apparent "etching" pattern on the exterior of the cylinder is simply a manifestation of the discrete nature of the voxel-based data set. Figure from [114].

3.1.5. Microstructural Characterization of Poisoning Phases

The cylindrical volumes were used to generate 3-D renderings of the data (Fig. 22(c)) as well as inputs to microstructural characterization codes previously developed.[67] Analysis was performed to determine volume fractions, phase size distributions, interfacial contact areas, and contiguity and tortuosity of the connected phases. Contiguity and tortuosity were calculated assuming the vertical axis of the cylinder as the primary transport direction. The variation in characterization results with volume size was analyzed by decreasing the cylindrical sample

volume and repeating the characterization. For most properties, significant deviation of the results began to occur for volumes smaller than 150 μm^3, providing confidence that the measurements on the original, largest cylinders was a reasonable representation of the structure. (A more detailed approach for assessing the statistical variation of property measurements is presented in section 3.4)

Detailed discussions of the likely poisoning reactions are discussed elsewhere in works by collaborators at EPFL.[143,144] However, a brief description of the suggested mechanisms is provided here to guide the analysis of the observed microstructures. As stated previously, XRD analysis did not detect any significant evidence of a crystalline silicon phase in the starting powder. However, EDS measured atomic silicon in the 2-3 at% range, indicating its existence in an amorphous state. During the cathode fabrication, likely the high-temperature sintering, the silicon and NNO were able to react to create the observed silicate phase, with a suspected chemical formula of $Nd_4Si_3O_{12}$.[144] In addition to the formation of the insulating silicate phase was the formation of NiO grains, as well as Nd-depletion of the NNO to create a less conductive stoichiometric phase, Nd_2NiO_4. In a compact form, the process can be written as

$$NNO_{\text{non-stiochiometric}} + Si \xrightarrow{T \approx 900^{\circ}C} Nd\text{-}Silicate + NiO + NNO_{\text{stoichiometric}} \quad (15)$$

Results of the characterization of the two samples are presented in Table 1. Volume fractions of each of the solid phases are presented as a percentage of the total solid volume. The two poisoning phases, silicate and NiO, are seen to account for 20 to 30 percent of the volume, while only 70 to 80 percent remains the desired NNO phase. Of the poisoning phases, there is a substantially greater amount of silicate, which is consistent with EDS measurements of the starting powders. At first glance, the 2-3 at% of Si measured in the powders seems to contradict the ~20 volume percent of silicate present in the sintered structure. However, the apparent

discrepancy is due to the difference in the types of measurements. While EDS measures a Si atomic percentage, the nanotomography results provide a volume percentage of the entire silicate phase, which includes the Si atoms as well as the other atoms to which it is bonded. Quantitatively, the consistency can be verified by using the stoichiometry of the various phases presented above and approximate silicate density values from the literature to convert between the two types of measurements.[145,146] In this manner, the two results describe the same overall amount of silicon in the system.

Although the poisoning phases account for a significant percentage of the solid material, the quantity alone does not provide a thorough description of the poisoning effect. It is equally important to consider the spatial distribution of the silicate and NiO relative to the active NNO phase. Recalling that NNO is a mixed-conductor, within an operating fuel cell its entire exposed surface could be available for electrochemical reactions. This is in contrast to a composite electrode, where electrochemical activity is confined to the triple phase boundary intersections of the ionic, electronic, and gas transport phases. Therefore in the case of an NNO electrode, the exchange current density (and therefore activation losses) will depend on the total surface area of the NNO which is exposed to the pore. However, the presence of the silicate and NiO now substantially decrease the exposed NNO surface, as observed in Fig. 22. In fact, the silicate phase appears to have a coating effect and creates a prevalent barrier between the NNO and pore phases. On the other hand, the formation of NiO appears to occur in a more localized manner and results in distinct particles, typically near NNO/silicate boundaries. Clearly, the morphological differences between the silicate and NiO phases lead to drastically different implications in terms of inhibition of cell performance. Herein lays a substantial benefit of the x-ray nanotomography technique: the ability to discern the 3-D morphology of multiple phases,

and in particular describe the significance of the morphology with regards to transport and reaction processes.

3.1.6. Implications for Performance

In an effort to quantify the effects of the poisoning phases, we can consider the hypothetical case in which Si was never present in the starting powder and thus silicate and NiO phases were never formed. Had this been true, presumably all of the solid would still be in the primary NNO phase. This scenario can be artificially created by converting all of the silicate and NiO in the segmented structures into NNO, as depicted in Table 1. Admittedly this is an approximation, as it is very possible that if the additional phases never existed, the microstructure could be somewhat different from that which is observed in this work. Therefore, the quantitative results of this approach are taken as an approximation. Since an actual pristine, un-poisoned sample is not available for rigorous comparison, a hypothetical pristine sample provides the best estimator of the ideal NNO structure. Characterization results for the actual and hypothetical ideal structures for each sample are shown in Table 1.

The values for NNO-pore area reported in Table 1 are calculated based on the total volume of each of the cylindrical samples, 201 μm^3 and 313 μm^3 for sample 1 and sample 2, respectively, as described earlier. The NNO-pore area is considered to be the best quantitative indicator of the silicate poisoning effect due to its tendency to coat the NNO surface and substantially decrease the active area for electrochemical activity. The NNO-pore area was found to decrease by 67% and 37%, in samples 1 and 2 respectively, due to the poisoning effect. The reason for the difference between these two samples is not entirely known, but could be due to the somewhat different microstructures seen in the interior and exterior of the extruded

cathode, as well as possible chance/random selection of sample location. However, the decrease in surface area for both samples is quite significant, and would be expected to severely affect cathode performance via an increase in activation losses.

Microstructural characterization of real and hypothetical "ideal" NNO structures		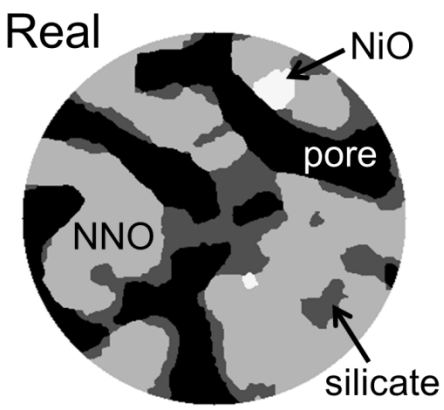		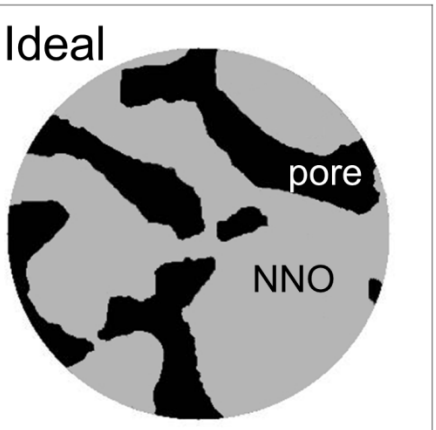	
		Sample 1	Sample 2	Sample 1	Sample 2
% of solid	NNO	70.3	80.3	100	100
	Silicate	27.9	17.7	-	-
	NiO	1.8	2.0	-	-
Mean phase size, μm	NNO	1.32	1.61	2.00	2.59
	Silicate	0.49	0.53	-	-
	NiO	0.49	0.49	-	-
NNO-pore area per volume, μm^{-1}		0.51	0.97	1.54	1.53
NNO tortuosity		1.33	1.37	1.16	1.22
NNO contiguity, %		99.7	99.9	~100	~100

Table 1: Microstructural characterization of real and idealized structures for sample 1 and sample 2. The images show NNO phase as light gray, the silicate phase as dark gray, NiO as white, and pore as black. Table from [114].

In addition to the surface phenomena, the implications for transport through the conductive phases (NNO and pore) can be considered as well. Assuming the poisoning phases are non-conductive, the NNO serves as the transport medium for both electronic and ionic species due to its nature as an MIEC material. The pore, in a similar fashion serves as the transport medium for gas species, namely oxygen to the active surface of the NNO. Therefore, the contiguous nature of both phases is important. The cathodes were highly porous, and as a result the pores were highly contiguous and assumed to not be responsible for transport-limiting behavior. More concerning transport limitations could occur in the NNO, particularly due to the alteration of the structure through the new phase formation. Table 1 reports that both the real and ideal structures of both samples retain NNO contiguity nearly completely. The NNO networks within each can then be further characterized by their tortuosity, which is a measure of the effective transport path length for electrons or oxygen ions divided by the straight-line path distance. The results suggest modest increases in NNO tortuosity (15% and 13%) for each sample due to the poisoning. The fact that the tortuosity is similar for each structure is not surprising. Because the silicate appears to be primarily a surface effect, the bulk transport within the interior of the NNO would logically not be significantly affected. The 15% and 13% losses which are observed when silicate and NiO are included could be due to possible local constrictions or severing of NNO transport pathways on a local scale.

3.1.7. Section Summary

The work presented in this section demonstrates an application of absorption contrast tomography to an SOFC cathode material poisoned during the fabrication process. Contamination of the starting powder with a small percentage of silicon led to the formation of

secondary poisoning silicate and NiO phases during high-temperature sintering. The primary phase, NNO, is expected to have changed stoichiometry to a less intrinsically conductive form, and is also restricted morphologically due to the two new phases. The silicate was found to have a coating effect on the NNO, which would have dual implications of substantially decreasing the NNO-pore active area as well as likely altering the NNO microstructure and creating bulk transport restrictions. The direct observation of these microstructural effects in 3-D provides substantial insight to their implications for cathode performance. Such descriptions would not be possible without the simultaneous capabilities of elemental sensitivity and 3-D structural mapping available through x-ray nanotomography. Clearly, for the NNO to be a viable cathode material for IT-SOFCs, particular care will need to be taken to avoid the formation of such widespread poisoning phases.

3.2. Sulfur Poisoning-induced Degradation of a Ni-YSZ SOFC Anode

Section 3.2 is based on the publishing of this work in [147].

3.2.1. The Sulfur Poisoning Problem

The conventional solid oxide fuel cell anode material, a composite consisting of nickel and yttria-stabilized zirconia (Ni-YSZ), has been shown to be highly sensitive to poisoning degradation due to trace impurities, such as hydrogen sulfide, in the inlet gas stream.[91,148,149] However, despite these issues, the Ni-YSZ cermet remains the most common choice for SOFC anodes due to a number of advantages: excellent physical, chemical, and thermal-mechanical compatibility with other SOFC components, as well as excellent catalytic behavior at high temperature for both electrochemical and internal reformation reactions.[102,105,150-152] However, for the continued development of SOFC's operating on reformed hydrocarbon-based fuels (whether reformed externally or internally), attention be paid to understanding the degradation mechanisms that can occur due to the impurities in the fuel streams. This section focuses on characterizing and understanding the sulfur poisoning effect and how it impacts electrode function.

Sulfur poisoning of SOFC anodes is typically described in terms of two separate processes.[103,153-156] Initially, elemental S adsorbs on the surface of the Ni, blocking active sites and therefore decreasing electrochemical activity. This process has been observed to occur immediately upon H_2S exposure and cause a rapid performance loss.[157,158] However, with prolonged exposure, lower operating temperatures, or higher H_2S concentrations, a second poisoning phenomenon is observed. The gas reacts with the Ni metal leading to the formation of nickel sulfide species in a bulk manner.[159] These phases have been observed to form with

length scales on the order of microns, which is similar in scale to the microstructural features typically observed in SOFC anodes.[85,92,97] This poisoning process is much slower than the sulfur adsorption, and is typically attributed to extended exposure. It is thought that the formation of new phases will create irreversible changes of the microstructure of the anode.

However, there remains debate in the literature as to the conditions (temperature, time, and H_2S concentration) under which each of the two poisoning regimes is applicable. This is primarily due to a lack of understanding about the fundamental mechanisms and the difficulty in directly observing the poisoning processes experimentally. To help guide understanding, Wang et al. used density functional theory (DFT) to numerically generate a Ni and S phase diagram, which suggests that under typical SOFC operating conditions with ppm-level H_2S, surface-adsorbed S is more likely than bulk nickel-sulfide formation.[160] The high temperature of SOFC operation is more conducive to the adsorption poisoning mechanism. However, operation under higher H_2S concentration (which could occur due to a lapse of proper sulfur removal from feed streams) or lower temperature (such as during cell start-up or shut-down) could produce conditions more suitable to bulk sulfide phase formation. Some experimental work has been done to examine these bulk phases.[90,148]

Due to the temperature-ramp exposure conditions that were used in this work, it could be possible the anode was subjected to both poisoning mechanisms. While each has implications for anode performance, the adsorption mechanism is not observable using the techniques currently employed. The x-ray nanotomography and x-ray fluorescence techniques described in the following sections work under spatial resolutions on the order of tens of nanometers, and would not be able to detect a monolayer or even thin multi-layer surface coverage. On the other hand, bulk nickel-sulfide phases are easily observed, although their exact composition in this

study remains unknown. (Use of an additional complementary technique, such as x-ray diffraction, high-resolution energy dispersive x-ray spectroscopy, or high-sensitivity XANES/EXAFS would be required to determine the chemical composition). Therefore, nickel sulfides in general will be denoted in this work by Ni-S, realizing that this could refer to such possible forms as NiS, Ni_3S_2, Ni_3S_4, Ni_7S_6, etc.[90,148,161]

3.2.2. Sample Treatment and X-ray Nanotomography Imaging

Ni-YSZ anodes were fabricated by a procedure similar to that reported by Yang *et al.* [104] (except without the addition of barium oxide as described in the cited work, and with the addition of corn starch as a pore former). The anode fabrication and exposure to hydrogen sulfide was performed by collaborators in Meilin Liu's group at Georgia Tech, but are described briefly here. The anode was fabricated using NiO and YSZ powder, as is typically done, and was produced along with an electrolyte and cathode comprising a whole cell. The cell was mounted on an alumina support tube, and heated to 800 °C in air. The gas was then switched to pure hydrogen to reduce the anode to the Ni-YSZ form. This process is typical for Ni-YSZ anode fabrication. 100 ppm H_2S was then introduced to the hydrogen fuel and the cell was held at 800 °C for 1 hour. Following the hold period, 100 ppm H_2S was maintained during a temperature ramp-down. The cell was cooled at 1.5 °C per minute down to room temperature. As an additional note, the 100 ppm poisoning condition used in this study is somewhat higher than what would be typically seen in an operating fuel cell (with H_2S concentrations more likely on the single ppm level). However, the higher concentration used in this study was to promote the poisoning process and the formation of bulk nickel sulfides in a reasonable amount of

experimental time, and produce noticeable alterations of the Ni-YSZ structure, even if done in an exaggerated manner.

FIB-SEM (performed again by Jeff Lombardo) was used to create a sample for x-ray nanotomography. The resulting cylindrical sample was approximately 10 microns in diameter and 20 microns tall. Reasonable sample dimensions to obtain ideal x-ray transmission characteristics were estimated based on previous work with Ni-YSZ imaging.[4] The cylindrical sample was mounted on the tip of a pin, and an optical microscope was again used to place several gold particles on the top of the sample as fiducial markers.

X-ray nanotomography was performed at the Advanced Photon Source, beamline 32-ID-C. For the first set of imaging, tomography was performed at 4 energy levels (8326, 8334, 8341, and 8348 eV) spanning the Ni K-edge. The energy levels were chosen based on the results in section 2.2.1. (see Fig. 12), and represent subtle inflection points for each of the Ni and Ni_3S_2 spectra.[106,107] Inflections points were chosen because, when observing the change between these energy levels, Ni and Ni_3S_2 would display the greatest differences in contrast. An alternative approach, in theory, would be to perform imaging across a sulfur absorption edge in addition to the Ni edge. However, in practice limitations in the beamline optics and instrumentation make this impossible. The S K-edge, 2472 eV, is beyond the lower limit of the monochromator's range, and incident x-rays with such low energy would also be too readily absorbed by the composite structure and provide inadequate transmission signal anyway. Therefore, the difference in spectra for Ni and Ni-S across the Ni edge is used as an alternative indicator of the presence of S. At each energy level, tomography was performed with 361 projections at 0.5° increments from -90° to +90°. A zone plate providing spatial resolution of 30 nm, and image pixel size of 25 nm, was used for each tomography. After using the gold particles

to correct the images to a central rotation axis, reconstruction was performed using filtered back projection, resulting in four separate 3-D data sets.

Some example cross sections of data from each energy level are shown in Fig. 23(a-d), which are all normalized to the same gray scale. The pure Ni metal is the most obvious solid phase, and displays a drastic increase in absorption (dictated by bright pixels) across the Ni edge, as expected. Across most of the Ni surface there also appears to be another phase which has some increase in absorption across the edge. This scale layer must therefore contain some Ni, although in somewhat lesser concentration than the pure Ni phase. The scale is preliminarily prescribed to be a Ni-S phase, and will be discussed in greater detail in following sections. Two other phases are also evident. There is a darker gray phase, which does not show any change in absorption behavior amongst the four images, and is labeled as YSZ. Lastly, the uniform dark background is the pore space.

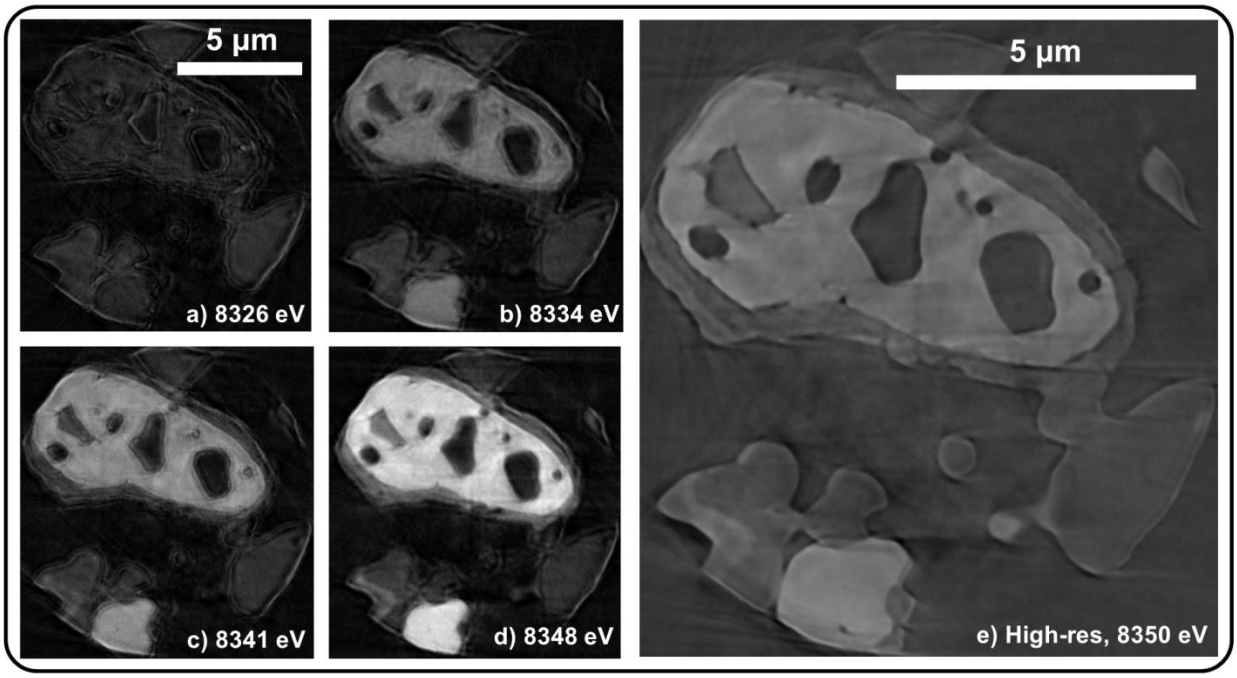

Figure 23: X-ray nanotomography of a sulfur-treated Ni-YSZ anode. In (a)-(d) Multi-energy tomography is performed by imaging the sample at four energy levels across the Ni K-edge. Contrast change indicates the presence of Ni, and therefore can identify Ni and Ni-S phases. In (e) a high-resolution tomography at 8350 eV with improved optics is shown in an enlarged view to demonstrate the clear definition of edges and particle boundaries. Figure adapted from [147].

As seen in Fig. 23(a-d), the original four tomography scans show adequate contrast for the Ni-containing phases, but there is a high level of noise and artifacts, especially at the edges of particles. These types of imperfections are fairly common in x-ray tomography, and it is a consistent challenge to the researcher to mitigate them. As discussed previously, imperfect beam alignment, focus, low signal/noise ratio, or a combination of the above is frequently the cause. However, following the acquisition of the original data sets, improvements were made in x-ray optics, and the sample was imaged a fifth time using a new zone plate capable of 17 nm spatial resolution.[38] The fifth scan was performed by collaborating beamline staff Joan Vila-

Comamala and Steve Wang at the Advanced Photon Source. To obtain the best results possible, the tomography parameters were optimized to obtain a single high-resolution scan. Imaging was performed above the Ni K-edge at 8350 eV to obtain optimal contrast of the Ni and Ni-S phases with the surrounding YSZ and pore. Tomography was performed with 721 projection images acquired at 0.25° increments from -90° to +90°. Reconstruction was performed with an advanced Fourier transform (FT)-based *gridrec* method, which can achieve higher accuracy than filtered back projection for high-resolution data and is described in detail elsewhere.[56] A cross-sectional slice of the resulting reconstruction is shown in Fig. 23(e). Significant improvements can be observed in image quality compared to the earlier data sets, particularly at particle boundaries. Interfaces between the different phases, manifested as sharp edges in the images, are much more visible in the high-resolution scan.

Because of the substantial time involved to collect the high resolution tomography (on the order of hours), the imaging was only performed at the single 8350 eV energy level. Ideally, imaging across the Ni K-edge, as with the low-resolution zone plate, would be performed, but limited microscope access and run-time precluded this option. Fortunately, a combination of the original data and the high-resolution data could be used to map the various phases. The multiple energy levels of the original data provide contrast imaging information, whereas the high-resolution data clearly defines boundaries. To work with them together, the high-resolution data set was resampled to match the lower resolution, and spatially registered in 3-D using Avizo's "Affine Registration" module. Although this sacrifices the very fine resolution obtained from the improved zone plate, the high quality of the images and ability to differentiate edges is still maintained.

To label the 4 phases, a segmentation approach using the watershed function in MATLAB was adopted. In an ideal world, an entire 3-D structure could be completely manually labeled as Ni, Ni-S, YSZ, or pore and there would be no need for any type of segmentation algorithm. However, while doing so is possible, it would require substantial time investment and be very tedious. In addition, such an approach would not lend itself to large or geometrically complicated structures. Therefore, the watershed algorithm is implemented to decrease the total amount of manual interaction by automating part of the labeling process. Discussion of the watershed algorithm for image segmentation was presented in section 1.7, but is re-iterated briefly here in the context of the specific application unique to this sample. The watershed algorithm requires as inputs the definition of "seeds" and "boundaries". The algorithm then proceeds by "flooding" starting at the seed regions, within the constraints of the boundaries, to label the entire structure. For this study, the gradient magnitude of the high-resolution data was used to define boundaries.

As the origins of the flooding process, the seeds of the watershed must represent regions which can, with a high level of confidence, be identified as a given phase. It is therefore up to the researcher to identify these regions. For example, if we can determine a large region of an image that is clearly the Ni phase, we would manually label that region as a Ni seed. There might be some regions which appear to be possibly Ni, but if this region is for example near an interface with another material, it may not be entirely clear whether that region belongs to the Ni phase or the other phase. Therefore, we would leave this region of the material unlabeled. The unlabeled region will then be given a label automatically during the watershed algorithm based on its proximity to other labels as well as particle boundaries. The same approach is applied to all phases of the material. In this work, the selection of which regions belong to which phase is

guided by the contrast in the four data sets of the low-resolution data, as well as the x-ray fluorescence data which will be discussed in the following section.

The watershed seeds were created manually using the "Segmentation Editor" plugin for the free software ImageJ. The 3-D data from the high-resolution scan was loaded into ImageJ as a tif image, which amounts to a series of 2-D cross sectional slices. Freehand selection tools were used to outline seed regions, using the contrast in the low-resolution data as a guide. To produce the seed labels in a reasonable amount of time for over 300 slices of data, interpolation was used to avoid the need to label every slice. To do this, labels were manually produced for certain slices, as shown in Fig. 24(a). Slices (i) and (iii) were manually labeled, shown by the green highlights, while 1 or more slices between them exemplified by (ii) are "skipped" and not labeled. The labels for these skipped slices (ii) were then created automatically by interpolating the labels from the manual slices (i) and (iii). Results of the interpolation are shown in Fig. 24(b,ii). Depending on the number of skipped slices, and the complexity of the geometry, the labels frequently required some manual modification and corrections to conform correctly to the structure. Either the interpolated labels could be modified, or additional labels could be created for slices which were previously skipped, and the interpolation then repeated with less separation between labeled slices. This was an iterative process requiring substantial manual interaction, and was repeated until a satisfactory set of labels was created for each phase. Note that the labeling for just the Ni phase is shown in Fig. 24(a-b), but the same process is performed for the Ni-S, YSZ, and pore phases as well.

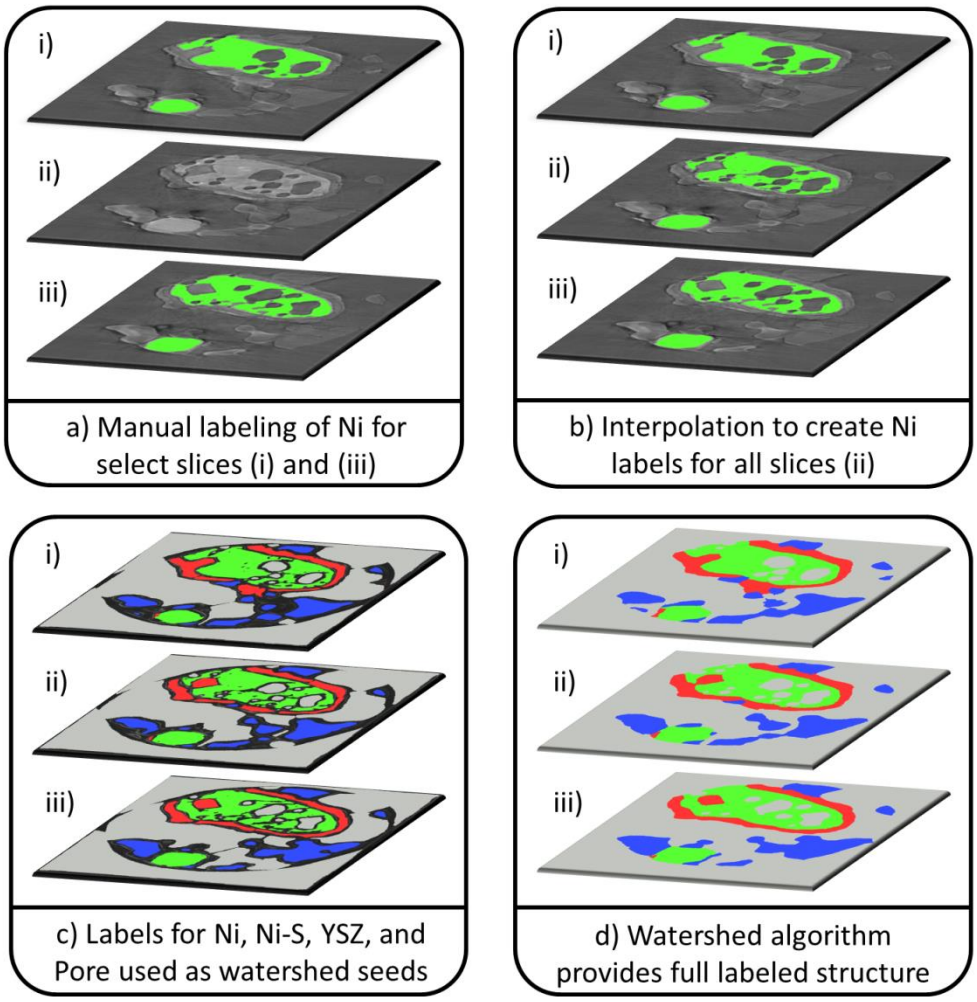

Figure 24: Manual input to watershed algorithm. In (a), manual labeling of the 3-D data was performed for some slices, shown by (i) and (iii). Other slices (ii) were left unlabeled. An interpolation scheme was used to create labels for those slices which were not manually labeled, as shown in (b). Labels for all 4 phases (Ni, Ni-S, YSZ, and pore) for the entire volume were used as seed labels for watershed (c). Watershed segmentation provides labels for the entire structure (d). Figure from supplementary material of [147].

The labels are then used as seeds in the watershed algorithm. This is first done by overlaying the seed labels on the gradient magnitude image, as shown in Fig. 24(c). The labels are imposed as local minima on the gradient map, and therefore serve as origins of the

"flooding" process which expands the seeds until neighboring labels meet at local maxima (aka the edges). Results after the watershed segmentation has been performed are shown in Fig. 24(d). The segmented structure contains simply one integer label for each of the four phases, depicted as four different colors in the figure. The quality of the segmentation result is assessed visually by comparison with the original grayscale data, as depicted in Fig. 25. If the seeds used in the watershed algorithm are too sparse, they will not accurately capture the correct distribution of phases. In addition, weak edges, which can occur due to neighboring phases of similar gray-scale value (such as YSZ and Ni-S), can be problematic if sufficient labels are not provided because there is not enough constraint in the growth of the seeds, and there may be extensive regions mislabeled. The labeling process is therefore a trade-off between accuracy and manual interaction time. In addition, it is an iterative process, as qualitative evaluation of the results in Fig. 25 may not be satisfactory on the first attempt. In this work, a second iteration of seeds was used to correct regions that were not captured properly by the watershed on the first attempt, and reasonable results were obtained. As is common in image processing and segmentation, it is a "human factor" judgment of how well the segmented structure represents the original data. This is commonly the case with the analysis of real structures, even using simple segmentation approaches like grayscale threshold selection.

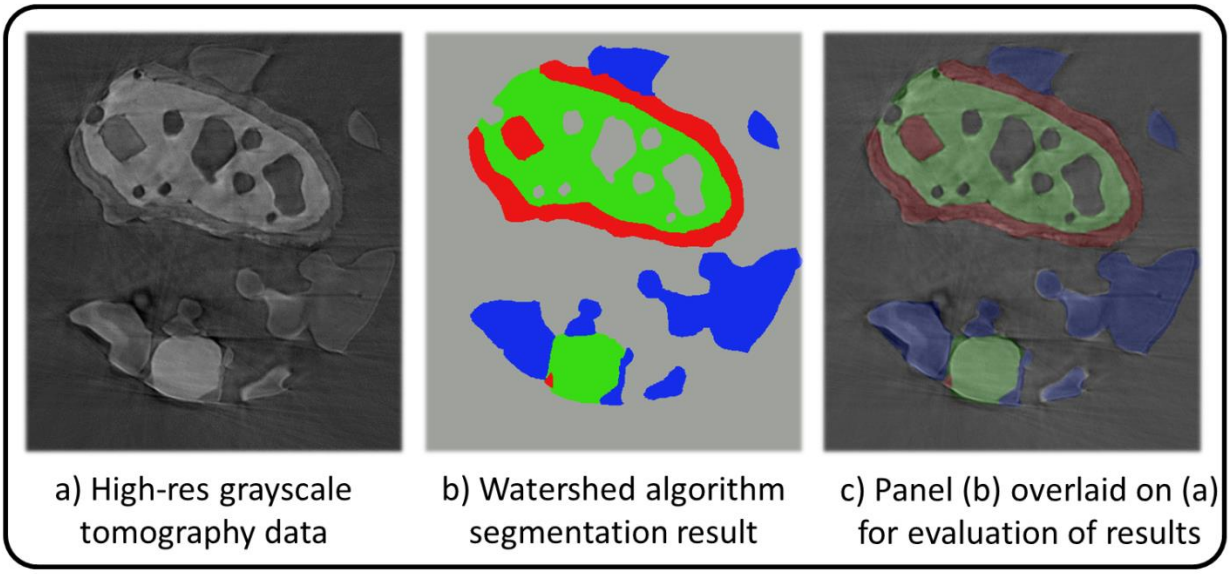

Figure 25: Evaluation of segmentation results. One example cross-sectional slice of the original high-resolution data is shown in (a). The results of the watershed segmentation for the same cross section are shown in (b). By overlaying (b) on top of (a), we can visually assess the accuracy of the segmentation results, and determine the labels represent the structure quite well. Figure from supplementary material of [147].

3.2.3. Synchrotron X-ray Fluorescence Elemental Mapping

The scale of material coating the nickel in the tomography data has, to this point, been assumed to be a nickel sulfide. The XANES spectra of Ni and Ni_3S_2 were investigated previously as described in section 2.2. However, even though imaging was performed at corresponding energy levels in the current work, the noise and imaging artifacts in the multi-energy tomography data (Fig. 23(a-d)) made it difficult to obtain exact matches between certain regions in the structure and the known reference spectra.[107] This could possibly also be explained by the nickel sulfide in this work existing in a different chemical form, and therefore exhibit a somewhat different XANES spectrum, than the Ni_3S_2 examined previously. To

confirm that this scale is in fact a nickel sulfide, x-ray fluorescence (XRF) spectroscopy was used to provide elemental mapping of the sample from a single orientation.

Synchrotron XRF was performed by collaborating beamline scientist Barry Lai at the Advanced Photon Source, beamline 2-ID-D, using a focused beam with a spot size of 200 nm. Because the primary purpose of the XRF measurements is to determine the composition of the scale, which is on the order of several hundred nanometers to single micron in thickness, the 200 nm spot size of the XRF probe is reasonable for obtaining a significant fluorescence signal. The resolution of the XRF is coarser than that of the tomography, the latter of which requires a small resolution (tens of nm) to provide an adequate structural map of the morphological features of the sample. However, comparison of the XRF and tomography data is visual and qualitative (as shown in Fig. 26), and not on a direct point-to-point basis, so having the same resolution or pixel size for the two methods is not necessary.

General information about x-ray fluorescence measurements can be found in the literature.[162] In contrast to the full-field capabilities of the TXM, the XRF method utilizes a focused beam which is rastered across the sample to simultaneously collect spatially-resolved fluorescence signals from nickel, sulfur, and zirconium and provide a corresponding map of the Ni, Ni-S, and YSZ phases respectively. To obtain signal, the sample is exposed to a beam with a sufficiently high energy to excite electron shell transitions within the constituent atoms, the K transitions being the most prominent, followed by the lesser L and M transitions. Therefore, the detected signal contains emitted fluorescent x-rays of characteristic energy which can be prescribed to known transitions within the expected elements of Ni, S, and Zr, providing mapping capability. The result is a 2-D elemental map of the sample. Note however, that for a given raster spot location, it is common to detect signal from more than one element. This is

because the incident beam transmits through the thickness of the sample, exciting transitions and creating fluorescent signal in the interior of the sample as it progresses. Therefore, the detected signal at a given spot is a function of the relative amounts of the different elements along that spot's beam path, as well as their depth into the sample and distance from the detector. Regions of the sample close to or facing the detector will provide more usable signal than regions opposite the detector, the fluorescent signal of which must travel through the sample material itself in order to reach the detector. Rotation of the sample or detector followed by an additional scan could resolve this issue if necessary, but was not determined to be necessary in this work.

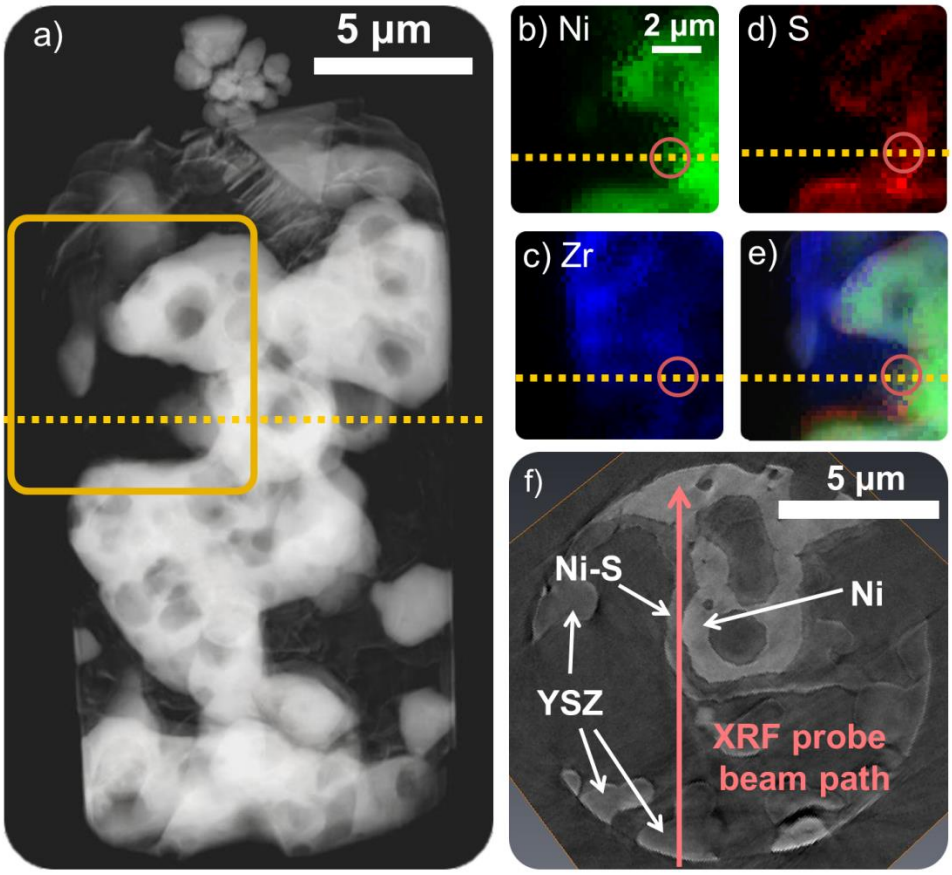

Figure 26: X-ray fluorescence spectroscopy of the H_2S-treated Ni-YSZ sample. An absorption-based image (a) from the XNT experiments is compared with XRF maps of Ni (b), Zr (c), S (d). A composite map of the three elements overlaid on the corresponding region of the absorption

image is also shown (e). The S signal is strongest near the edges of the Ni signal. The yellow dotted line shows the location of a cross section, extracted from the high-resolution XNT tomography, shown in (f). The pink circles in (b)-(e) and the pink arrow in (f) denote the XRF beam location and path at one particular scanning spot on the sample. The high Ni and S signals seen in (b) and (d) are correlated to a significant thickness of the scale, shown by the pink arrow in (f). The correlation of these images provides strong confidence in the identification of the scale as a nickel-sulfur compound, denoted generally by Ni-S. Figure from [147].

Results of the XRF chemical mapping have been compared to the tomography data in Fig. 26. Figure 26(a) is an absorption-based image of the entire sample taken from the tomography data. Bright regions indicate high x-ray absorption (high density). The yellow box denotes a region of interest used for XRF mapping (Fig. 26(b-e)). Figures 26(b-d) represent the XRF signals for Ni, Zr, and S, respectively. Note the sulfur signal (Fig. 26(d)) is clearly evident, and approximately correlated with the Ni signal, particularly around the edges of the Ni. In Figs. 26(a-e), a horizontal yellow dotted line is drawn to indicate the location from which a cross-sectional slice of the high-resolution tomography is extracted, and shown in Fig. 26(f). In addition, Figs. 26(b-e) each have a pink circle, indicating one particular spot at which the XRF beam was used to acquire the Ni, Zr, and S signals. Note that the incident x-ray beam will travel through the sample, creating fluorescent x-rays throughout the thickness of the sample. At the location of this circle, the XRF indicates the presence of all three elements, including a relatively high amount of S. To correlate to the tomography data, the XRF beam path corresponding to the circular marks of Figs. 26(b-e) has been labeled by a pink arrow in Fig. 26(f). The beam path clearly intercepts a significant amount of the scale, as well as some Ni and some YSZ (and some

pore). Because the XRF data displays a significant concentration of S at this location, and because the tomography data showed an increase in x-ray attenuation at this region when increasing x-ray energy across the Ni K-edge, it is reasonable to conclude that this scale contains both S and Ni, and is hence labeled generally as Ni-S. This validates the earlier assumption of the Ni-S scale.

3.2.4. Characterization and Discussion

The 3-D structure, segmented and labeled by combining information from nanotomography and XRF measurements, is shown in Fig. 27. This cylindrical sample was milled from bulk material using FIB-SEM, and therefore the surfaces on the exterior of the cylinder are not true exposed surfaces. The 3-D rendering permits some qualitative observations. The Ni-S scale, shown in red, appears nearly uniformly on the Ni surface, except for in regions where Ni and YSZ are in direct contact, or areas of internal porosity, such as the large pore visible in the middle of Fig. 27(a) labeled by the black arrow. But in addition, there are some anomalous regions of exposed Ni surface without a Ni-S scale. Such a surface can be seen in the top left of Fig. 27(a) labeled by the white arrow. A reasonable first guess to explain this would be that the pore volume next to this Ni grain is disconnected from the other pores, and was therefore never exposed to H_2S gas. However, more detailed examination of the internal pore structure of the sample reveals this is not the case. Ni surfaces that are both exposed and covered by a Ni-S scale are in contact with a common pore network, and have therefore been exposed to the same gas environment. (Although this is not easily discernible from the figures in this paper, the authors have used digital 3-D renderings and cross-sectional views of the internal structure to confirm the conclusion.) Presumably, this pore network within this relatively small sample is

also connected to a larger pore network contiguous throughout the entire anode, as evidenced by the fact that hydrogen sulfide gas seems to have clearly penetrated the sample, creating the sulfide scale on most exposed Ni surfaces. So why is there no Ni-S scale on some Ni surfaces? Although the reason is unknown, and would require further investigation, the authors present two possibilities at this time. One possibility is that during the fabrication of the cylindrical sample by FIB milling, the porous nature of the material may have allowed the ion beam to accidentally mill some of the interior of the sample. If that is the case, it could have removed some material, possibly including Ni-S. Of the regions of exposed Ni surface, most are located near the exterior of the cylinder, meaning they could have been exposed to the ion beam. However, the exposed surfaces also exist in several locations and have faces oriented in a number of different directions, which complicates the explanation since the ion beam mills by a line-of-sight mechanism. A second possible explanation is preferential nucleation of Ni-S formation at certain locations on the Ni surface. If that were the case, it could be possible that S atoms adsorbed on the Ni surface diffused to a nearby Ni region where Ni-S formation was occurring, leaving the remaining surface exposed to the gas without formation of Ni-S. To validate this hypothesis, it would be necessary to characterize the surface orientation and surface defects of the Ni region without the Ni-S formation as well as the interface between Ni metal and Ni-S using transmission electron microscopy to reveal the surface characteristics that prevent Ni-S formation. This analysis may provide further insight into rational design of sulfur-tolerant Ni surfaces.

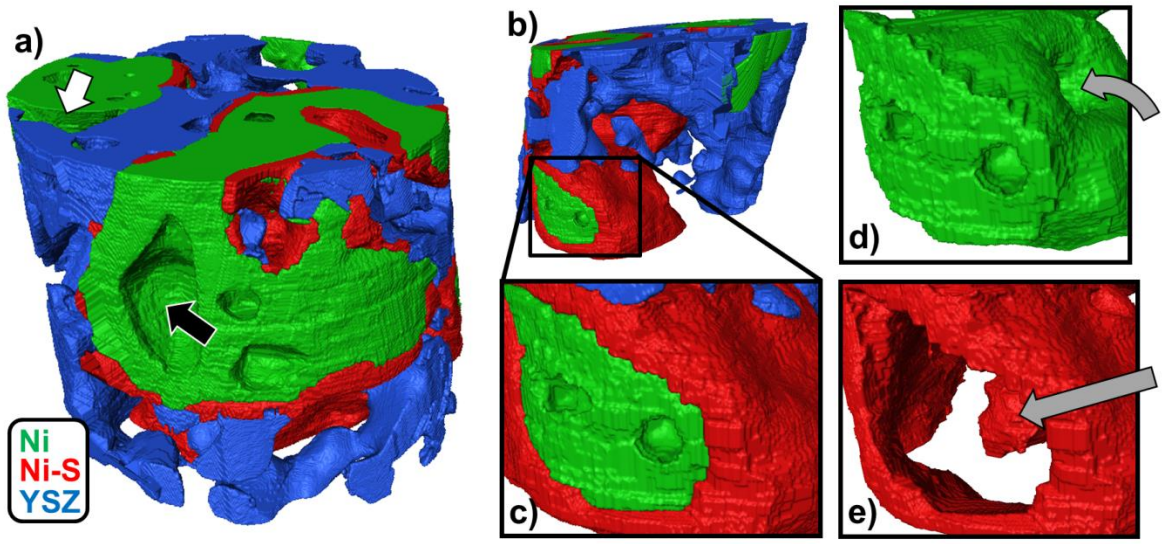

Figure 27: 3-D renderings of the anode microstructure. The 3-D structure of the cylindrical sample is shown in (a). The diameter of the cylinder is about 12 microns. Recall the cylinder was milled from bulk material using FIB-SEM, so the exterior surfaces of the sample are not actually exposed surfaces. A second view is presented in (b), and a magnified picture of a particular region is shown in (c). The region shown in (c) is also used to show the distributions of the Ni phase (d) and the Ni-S phase (e). Figure from [147].

Qualitative observation also suggests that the Ni-S scale forms by outward diffusion of Ni ions through the sulfide scale to the gas interface (as opposed to inward diffusion of S to the Ni interface), as suggested in the literature.[90,161,163] This is apparent because of large regions of Ni-S which seem to extend into the interior of Ni particles. This effect is depicted in Figs. 27(b-e), which display a second angle of the microstructure. Figures 27(b-c) show a magnified view of one region of Ni-S scale growth. In Fig. 27(d), only Ni is displayed, and there is a visible cavity extending into the interior of the Ni particle, as labeled by the curved gray arrow. In Fig. 27(e), just the Ni-S is shown. The straight gray arrow points to a volume of Ni-S

which occupies the entire cavity. It is unlikely this type of Ni-S structure would form by an inward S diffusion mechanism, as it would imply a larger S diffusion coefficient, and thus a deeper reaction penetration, in some regions of Ni versus others. More likely, these interior regions were pores before H_2S exposure, and upon sulfidation the scale grew thicker and thicker on the interior surfaces of the Ni cavity until the entire cavity was filled by Ni-S. This explanation is consistent with previous studies which used inert markers and optical microscopy to show scale growth outward from the metal surface. [164,165]

Such outward scale growth is also relevant to the role of YSZ in the system. It is clear there are regions of Ni-S scale which cover Ni surfaces only to the extent at which they are exposed to pore and not in contact with YSZ. That is, there is not a Ni-S scale between Ni and YSZ. Furthermore, there is no S scale on YSZ alone, and the XRF data does not display any significant correlation between the locations of Zr and S. Therefore, it is concluded that YSZ does not participate in any chemical reaction, and serves only as a physical barrier to the growth of the Ni-S scale on Ni surfaces.

The segmented 3-D microstructure was also characterized quantitatively.[67,68] A voxel counting scheme was used to compute the volume fraction of each of the four phases (the three solid phases plus pore). The Ni-S scale was found to account for close to 11% of the sample volume, on the same order of magnitude as the Ni and YSZ phases, which contributed to 26 and 19 percent, respectively. This ratio of total Ni to YSZ is in approximate agreement with the 55:45 weight ratio of NiO to YSZ in the starting powders of anode fabrication. Interfacial areas between the phases were also determined by a counting scheme. In the calculation of interfacial areas, isolated and internal pores were neglected. Such pores, several of which can be observed internal to Ni in the center of Fig. 27(a), were discounted because they are non-contributing in

terms of transport and chemical/electrochemical reactive area. Considering the remaining Ni surfaces, 74% are in contact with Ni-S, 18% with YSZ, and only 8% remain exposed to pore (for unknown reasons as discussed previously). Evidently, the vast majority of what were originally clean Ni surfaces are now covered by the Ni-S scale. If the Ni-S is insulating and non-catalytic, this could have serious implications for the possible use of Ni surfaces as catalyst sites in hydrogen oxidation or hydrocarbon reformation reactions, as well as the triple phase boundary (TPB). The TPB density of the structure was calculated by a similar counting scheme, and compared to that of an "ideal" clean structure created by digitally removing Ni-S from the 3-D volume and replacing it with pore. Although only an approximation, it was found that the Ni-S formation decreases the TPB density of the anode by 67%. In the poisoned structure, only the anomalous exposed Ni surfaces, as described earlier, are still contributing to TPB density while the majority of the Ni surfaces are covered with Ni-S thus eliminating their TPB sites. This decrease in TPB sites could create a corresponding decrease in electrochemical reactions and cell performance.

To further characterize the Ni-S scale, a ray-shooting method was used to measure feature sizes of each phase.[68] The ray shooting algorithm operates separately on each phase of the sample by taking each interface point of that phase, and launching a ray into the interior of the phase in the normal direction. The ray is propagated until it hits another interface or the boundary of the domain. The lengths of all such rays are catalogued and used to form a distribution, as shown in Fig. 28. Note the relative size of the sample features compared to the total sample size is important in understanding the distributions. In this sample, the Ni, YSZ, and pore phases have mostly large features close to the size scale of the entire sample (see Fig. 27(a)). Consequently, because the sample was extracted from the bulk using FIB milling, a

significant number of rays for these phases would terminate prematurely on the sample boundary, rather than continuing to propagate until another interface is reached (see section 3.4.3.2 for a proposed methodology for mitigating this problem). Therefore, the distribution represents an under-estimation of the true feature sizes, and is best interpreted as describing the relative feature sizes of the Ni, YSZ, and pore phases. The Ni-S scale, on the other hand, has generally small features with most rays traversing its thickness and terminating at the opposing interface within the structure, rather than on the boundary. Therefore, for the Ni-S phase interpretation of the quantitative results shown in the distribution is appropriate. And, as expected, the distribution of Ni-S is narrow, contained mostly within 1 micron, and is indicative of a scale of nearly uniform thickness. The peak of the distribution is located at about 570 nm. The tail on the right side of the Ni-S distribution can be attributed to locally larger regions of Ni-S, such as where it has completely filled cavities within the Ni (discussed previously), and the effect of a small number of rays that could be launched through the scale with a nearly tangent orientation, rather than in the more typical direction normal to the scale. The distributions of YSZ and Ni are quite similar to each other, and bearing in mind the discussion above, generally have feature sizes in the single micron range. The pore distribution is somewhat wider and contains a number of longer rays, covering a range of sizes from sub-micron up to the maximum measureable size, which is that of the sample itself.

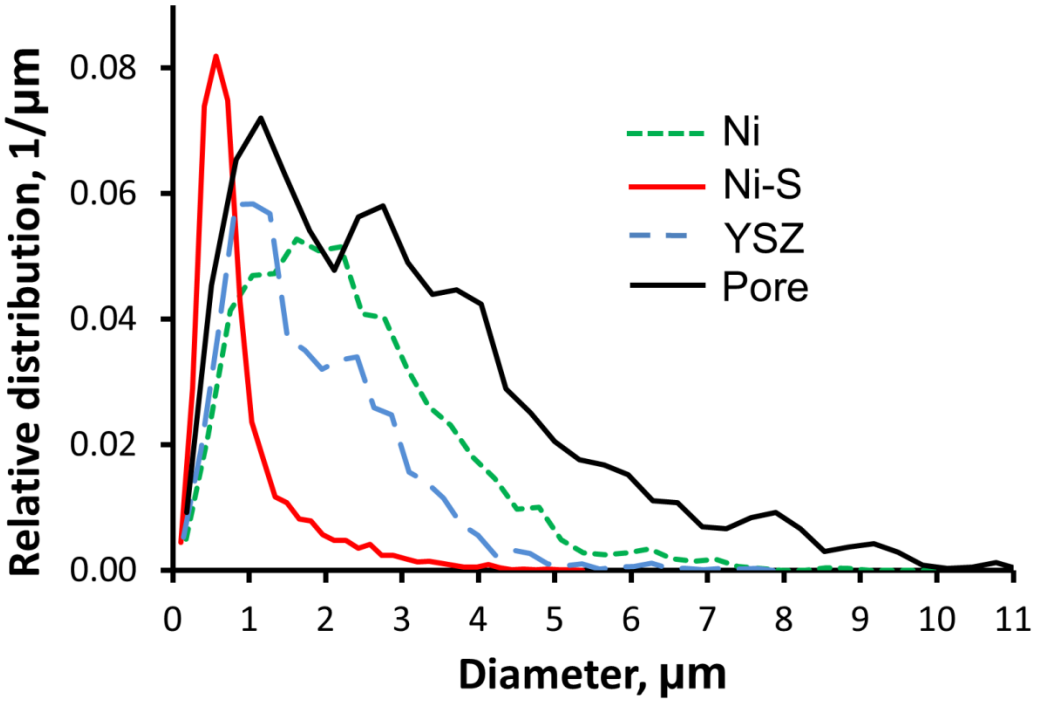

Figure 28: Feature sizes computed using a ray shooting algorithm. The narrow Ni-S distribution reveals that the Ni-S scale is fairly uniform, and on the order of several hundred nanometers to 1 micron thick. Figure from [147].

3.2.5. Section Summary

This particular study demonstrates the application of multiple techniques capable of providing complementary information. The x-ray nanotomography can provide excellent structural information, particularly when the imaging process is optimized by both experimental equipment (improved zone plate objective lens) and advanced image processing tools. This can be seen in the high-resolution tomography data used in this work. However, the chemical mapping capabilities of the nanotomography can be somewhat limited by the beamline's accessibility to certain absorption edges, as well as the noise and artifacts in the reconstructed data due to beam instability. With more extensive experimental time, these constraints could

possibly be overcome by careful imaging of multiple energy levels with the high-resolution tomography arrangement. With the careful collection of additional data around the Ni K-edge, it could be possible to match XANES spectra of the various phases with known reference standards as described in section 2.2. This is still a developing capability in the TXM field, and could provide valuable insights in the near future as instrumentation continues to improve. However, in this work a complementary x-ray fluorescence technique was used to provide elemental mapping to validate the identification of various phases in the tomography data. In particular, XRF was used to confirm the presence of S, and determine that its location approximately correlated with the edges of metallic Ni that were exposed to open pores. Although the exact composition of Ni-S was not determined, its implications for electrochemical activity of the electrode could be approximated based on its spatial mapping relative to Ni, YSZ, and pore phases. The Ni-S, which formed as a nearly-uniform scale on the Ni surface, significantly decreases the amount of clean Ni surface as well as the electrochemically active triple phase boundary. The exposure conditions, which included a ramped cool-down from elevated temperature, precluded the ability to provide a detailed description of the sulfidation reaction kinetics. It is likely that the formation of the bulk Ni-S phase occurred at least in part during the ramp-down process, as opposed to the 1 hour high-temperature hold period.[160] At this point it is difficult to determine whether the reactive species creating the Ni-S was gaseous H_2S, or atomic S adsorbed on the Ni surface during the hold period. A more rigorous and controlled experimental design would be necessary to reveal more information about the reaction mechanism. However the nature of the Ni-S formation, as a scale nearly covering the exposed Ni surface, has been presented and the characterization of the poisoned structure suggests

significant implications for electrode operation after brief exposure to relatively high levels of hydrogen sulfide.

3.3. Examination of Microstructural Networks in a Composite Gas Separation Membrane

Section 3.3 is based on the publishing of this work in [166].

3.3.1. Introduction to Mixed Ionic-Electronic Conducting Ceramics

Ceramic oxygen-transport membranes have applications in a number of energy conversion systems including solid oxide fuel cells,[167] Li-air batteries,[168] oxygen separation and permeation membranes for oxygen production,[169-171] partial oxidation of methane and clean coal production via oxy-combustion resulting in significant reductions in CO_2 emissions from coal fired power plants.[172-175] Besides energy generation systems, there are additional opportunities for ceramic membranes to be increasingly prominent in advanced manufacturing processes including electrochemical reduction cells for metals processing[176,177] and spent nuclear fuel re-processing[178] as well as high temperature electrolysis cells for hydrogen production[179] and state of the art combustion control sensors.[180]

The properties and function of these devices are controlled by mixed ionic and electronic conductivity (MIEC) in the respective material system. MIEC behavior can be expressed in one of two ways, either i) selecting a material with an intrinsic ability to conduct both ions and electrons, or ii) forming a dual phase composite material in which each phase forms a percolating network and serves as either primarily an ion or electron conductor. The present work focuses on the latter strategy for MIEC operation, namely fabricating a composite of ionic and electronic conductive materials, as depicted by the red and blue phases, respectively, in the cartoon in Fig. 29. The membrane separates regions of high (P''_{O_2}) and low (P'_{O_2}) oxygen partial pressure, and reactions occur on either side of the membrane, incorporating and releasing oxygen from the

ionic lattice. Electrons transport through the other phase to complete the electronic circuit and maintain charge neutrality. The inherent flexibility of multiphase systems makes it more feasible to tune the various properties needed to satisfy the set of stringent chemical, electrical, thermal and mechanical properties for a variety of MIEC applications. In this work, $Ce_{0.8}Gd_{0.2}O_2$ (GDC) is used as the oxygen ion-conducting phase due to its high ionic conductivity of close to 0.1 S/cm at 800 ^{o}C.[181] The electronic conductor is $CoFe_2O_4$ (CFO), which has a stable spinel structure and high electronic conductivity of greater than 1 S/cm at 800 ^{o}C.[182,183] This composite system has been used previously by several researchers, and has demonstrated high oxygen flux and stability under reducing environments in the presence of CO/CO_2, an important criteria for the membrane to be a viable component of syngas reactor systems.[170,182,184-186] In addition, this particular dual-phase membrane serves as a model system for general composite membrane studies.

Before discussing the nanotomography measurements and the results of this work in following sections, it is worth mentioning that it is recognized that the performance of ceramic composites are not necessarily bounded by the properties of the individual constituents. The presence of multiple solid phases, and the possible interaction of these phases (which could include such effects as interfacial contributions, bulk phase formation, long-term phase evolution, local stoichiometry change, etc.) could produce global response different than the properties expected from simple mixture rules.[1] This effect is described in terms of emergent properties and behavior, which have the potential to present both new opportunities and new challenges in microstructural design and functionality.[187] In MIEC composite membranes, the compatibility (or incompatibility) between the ionic and electronic phases, particularly during high temperature processing or operation, may lead to reactions producing additional interfacial

or bulk phases with implications for ionic and electronic transport. For example, Kharton in 2001 reported an order of magnitude drop in the ionic conductivity of a $Ce_{0.8}Gd_{0.2}O_2$- $La_{0.7}Sr_{0.3}MnO_3$ (GDC-LSM) composite membrane when elevated temperatures and increased sintering times were used during membrane fabrication.[188] The authors attributed this behavior to the formation of resistive "blocking" layers at GDC-GDC grain interfaces due to the diffusion of La, Sr, and Mn from the LSM phase. The hypothesized blocking layers are proposed to form during high temperature sintering, and provide significant barriers to ionic transport. An additional effect to consider is changes in local stoichiometry due to possible diffusion of La^{+3} and Sr^{+3} into the GDC fluorite lattice, leading to decreased mobility of oxygen vacancies and lower ionic conductivity. In the GDC-CFO system there is currently limited understanding of the impact of these interfacial phases on system performance.[182] In addition, unintentional formation of new phases in a bulk manner (whether it be during material processing or operation), on the same length scale as the primary phases, may also have impacts on the membrane performance, particularly from a transport perspective.

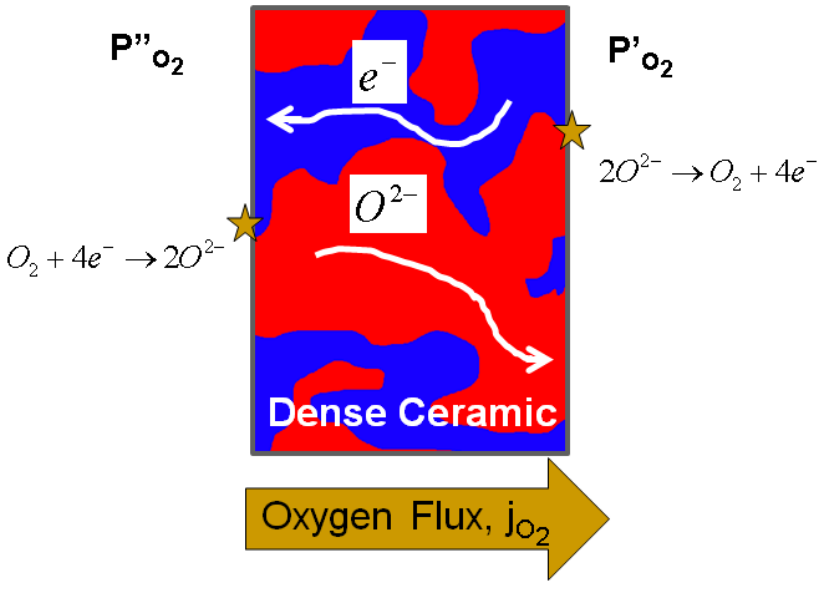

Figure 29: Dual-phase composite oxygen separation membrane.

3.3.2. Wagner Equation for Membrane Transport

A simple mathematical description of membrane transport can be found in the "Wagner equation".[189] A short derivation of the Wagner equation and discussion of its applications can also be found in [190], and is repeated briefly here. The Wagner equation is derived in the framework of transport-limited membrane performance, as opposed to kinetic-limitations from the reactions with the gas environment on either side of the membrane. The high temperature operation of these membranes (providing fast kinetics), as well as the appreciable thickness necessary to provide mechanical strength, provide reasonable justification for this assumption under most operating conditions. Under these conditions, incorporation of oxygen gas into the ceramic lattice is represented by

$$\frac{1}{2}O_2 + V_O^{\bullet\bullet} + 2e' = O_O^x \tag{16}$$

where $V_O^{\bullet\bullet}$ represents a lattice vacancy and O_O^x denotes lattice oxygen. It is assumed that the lattice vacancies are the charge carriers in the ionic phase. The flux of an arbitrary charge carrier *k* can be expressed as

$$j_k = -\frac{\sigma_k}{z_k^2 F^2}\nabla \eta_k \tag{17}$$

where z is the charge number, σ the conductivity, F is the Faraday constant, and $\nabla \eta_k$ the gradient of electrochemical potential. The electrochemical potential of a species can be expressed in terms of the contributions from the chemical potential and the electrical potential as

$$\nabla \eta_k = \nabla \mu_k + z_k F \nabla \phi \tag{18}$$

At steady state membrane operation, there can be no accumulation of charge, and the diffusion of ionic species in one direction is balanced by the diffusion of electronic species in the opposite direction. Electronic species can include, in general, electrons and holes, and the diffusional flux balance of the system to ensure overall charge neutrality is given by

$$2 j_{V_O^{\bullet\bullet}} = j_{e'} - j_{h^{\bullet}} \tag{19}$$

It is assumed that local equilibrium is obtained in the membrane and the internal defect structure is not affected by the transport processes. In this way, the chemical potential of the actual transport species can be re-cast in terms of a virtual chemical potential of gaseous oxygen. (In reality, there is no gaseous oxygen in the interior of the membrane, but the chemical potential of the solid-state species allow the determination of an equivalent gaseous oxygen chemical potential). This is expressed by

$$\frac{1}{2}\nabla\mu_{O_2} + \nabla\mu_{V_O^{\bullet\bullet}} + 2\nabla\mu_{e'} = 0 \tag{20}$$

$$\nabla\mu_{e'} + \nabla\mu_{h^{\bullet}} = 0 \tag{21}$$

The oxygen flux can then be expressed in terms of the flux of the oxygen vacancies, and grouping electron and hole conductivities as more general electronic conductivity,

$$j_{O_2} = -\frac{1}{2} j_{V_O^{\bullet\bullet}} \tag{22}$$

$$j_{O_2} = -\frac{1}{4^2 F^2} \frac{\sigma_{el}\sigma_{ion}}{\sigma_{el} + \sigma_{ion}} \nabla\mu_{O_2} \tag{23}$$

Integration across the membrane thickness L and expression of the chemical potential in terms of partial pressure of the gas phase yields

$$j_{O_2} = -\frac{RT}{4^2 F^2 L} \int_{\ln P'_{O_2}}^{\ln P''_{O_2}} \frac{\sigma_{el}\sigma_{ion}}{\sigma_{el} + \sigma_{ion}} d\ln P_{O_2} \tag{24}$$

Of interest in terms of microstructural characterization are the modifications that must be made to the conductivity terms. A correction factor accounting for the geometry of transport pathways must be applied to the bulk conductivities to obtain effective conductivities in a composite structure:

$$\sigma_{eff} = \frac{\phi}{\tau^2}\sigma_{bulk} \tag{25}$$

where ϕ and τ represent the volume fraction and tortuosity of the transport phase. These parameters are measurable using the x-ray nanotomography method, and can provide a measure of the transport limitations which can be prescribed specifically to the microstructure.

3.3.3. Membrane Fabrication and Electron Microscopy

The composite membranes were prepared by collaborator Kyle Brinkman (formerly of Savannah River National Laboratory, currently at Clemson University) and his team. They were prepared by mixing 60 percent by volume of the ionic conductive phase $Ce_{0.8}Gd_{0.2}O_{2-\delta}$ (InfraMat Advanced Materials LLC) and 40 percent by volume of the electronic conductive phase $CoFe_2O_4$ (InfraMat Advanced Materials LLC) by ball milling powder in ethanol for 6 hours. The ratio was chosen to provide a slightly higher amount of the ionic conducting phase, for which the bulk conductivity is lower than the electronically conducting phase. The mixture was then dried and sieved, and then mixed with a binder and uniaxially pressed under 20 kN of force into pellets of 16 mm diameter. Pressing was used to create a dense structure with minimal porosity. Pellets were then sintered in air at 1300^{o}C for 2 hours. The sintering temperature was selected as a compromise between the typical temperatures used for GDC and CFO sintering which are about 1500^{o}C and 1000^{o}C, respectively.[191] A ramp rate of 2^{o}C/minute was used during heating and cooling stages.

In order to confirm the chemical phases present and the spatial resolution required for X-ray nanotomograhy experiments, MIEC starting materials and ceramic membranes were characterized by High Resolution Transmission Electron Microscopy (HRTEM). The electron microscopy work presented here was performed as a collaborative effort between Kyle Brinkman and Dong Su at the Center for Functional Nanomaterials at Brookhaven National Laboratory. It is described briefly in order to properly preface following sections highlighting the new contributions of x-ray nanotomography central to this dissertation. Samples of the GDC and CFO powders (before any mixing or sintering) were prepared for electron microscopy by supersonic dispersion followed by careful dipping onto a Holey Carbon 400 mesh Cu grid (Ted Pella, Inc.) Thin samples of the sintered GDC/CFO membranes were prepared by a classic dimpling method using a Gatan dimpler 626. Ion milling was then used to decrease the final thickness to less than 10 nm (Fischione Model 1010). Scanning Transmission Electron Microscopy (STEM) with high-angle annular dark-field imaging (HAADF) and Energy Dispersive X-ray (EDX) mapping (with scan speed ~0.6 nm/s) were performed to distinguish each constituent phase in the composite. Bright field transmission electron microscopy and selected area electron diffraction (SAED) acquired using the JEOL-2100F TEM equipped with a Schottky field-emission gun (FEG) operated at 200 kV provided crystalline information.

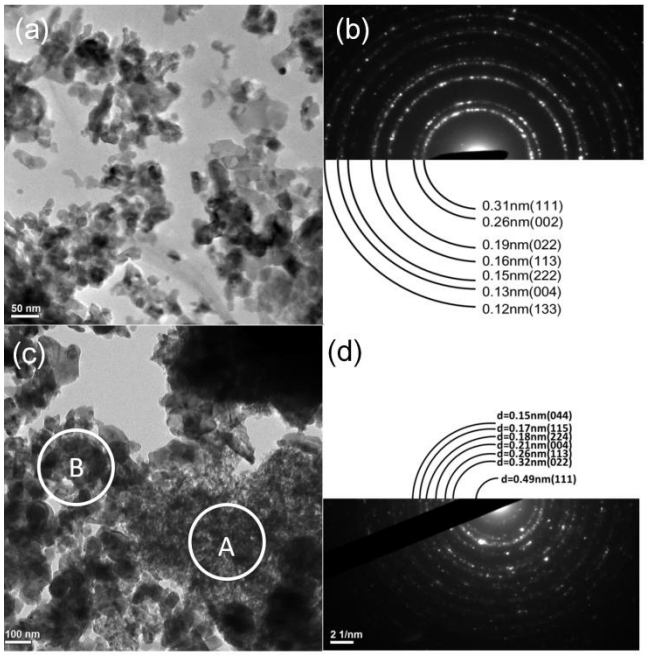

Figure 30: Electron microscopy of starting GDC and CFO powders. BF image (a) and SAED (b) of GDC powder. BF image (c) and SAED (d) of CFO powder. Figure from [166].

Electron microscopy of the GDC and CFO starting powders is shown in Fig. 30. As shown in Fig. 30(a), the individual nano-sized GDC powder is in the range of 12-50 nm. The SAED (Fig. 30(b)) diffraction pattern can be indexed to GDC (ICSD#28796), with cubic symmetry and lattice constant of a=5.42 Å. The starting powder of CFO is shown in Fig. 30(c). The CFO shows a distribution of particle sizes, two regions of which are labeled by circles A and B. Particles in A are smaller size particles in the 5-10 nm range, while larger particles (100-250 nm) are found in B. The SAED pattern of the CFO powder, shown in Fig. 30(d), was well indexed to ICSD #109045 as $CoFe_2O_4$ exhibiting a cubic structure with a=8.39 Å and a space group of F d -3 m (227). No secondary phases were observed for either of the starting powders.

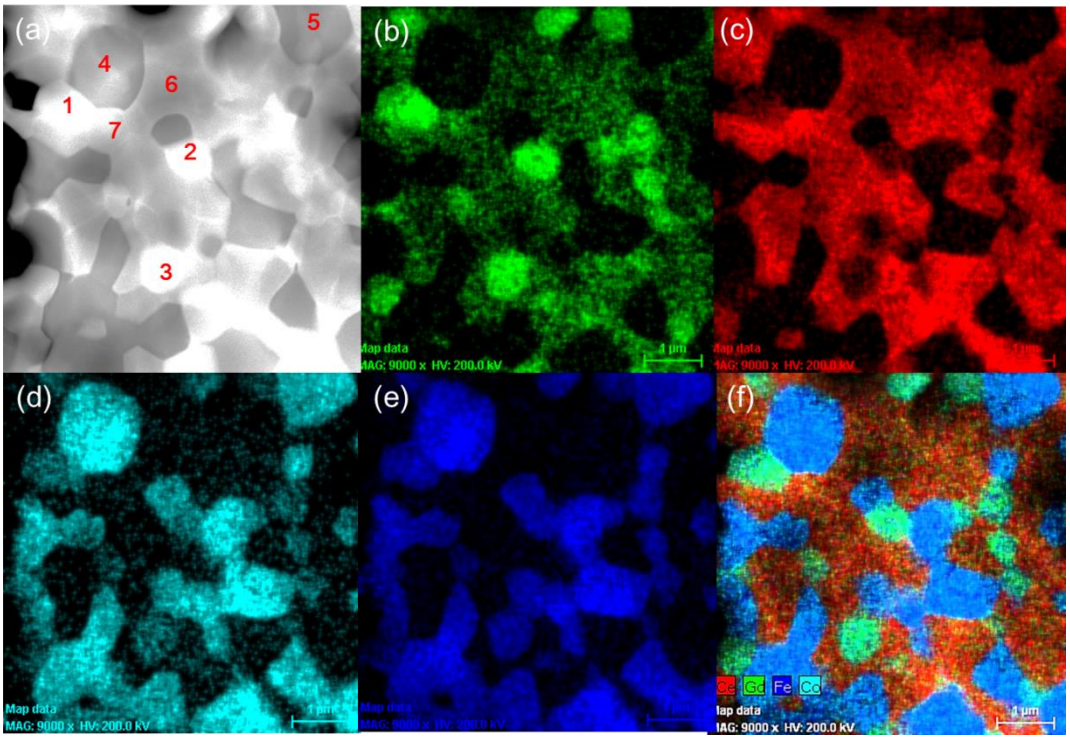

Figure 31: High resolution TEM mapping of composite membrane. a) HAADF image for the GDC/CFO (60% GDC, 40% CFO by volume) sample. (b-e) STEM elemental mapping for Gd (green), Ce (red), Co (cyan) and Fe (blue) respectively. f) Composite elemental map of Gd, Ce, Co, and Fe. Figure from [166]

The elements and phase distributions of sintered membrane composites were discriminated using STEM-HAADF imaging and EDX mapping as shown in Fig. 31. Three different contrast levels (bright, grey and dark) could be clearly found based on the HAADF image (Fig. 31(a)), indicating different average Z values of three solid phases. The EDX mapping in Fig. 31(b-e) could further be used to help distinguish the phases' constituent elements. The primary phases of GDC and CFO contained Gd/Ce and Co/Fe respectively, as expected, corresponding to the grey and dark grains in Fig. 31(a) respectively. In addition to these two phases, a brightest and heaviest phase seen in Fig. 31(a) is an emergent phase, which

can be seen in the EDX maps to contain Gd, Ce, Co and Fe. More substantial quantitative analysis in the supplementary material of the cited work suggests a chemical formula of $Gd_{0.374}Ce_{0.079}Co_{0.077}Fe_{0.47}O_x$, but for simplicity the phase will be denoted GFCC.[166] The electron energy loss spectroscopy (EELS) scan taken inside the GFCC grains (Fig. S2 of the cited work) has also shown the "fingerprints" for all four elements. In addition, this will be verified using a 3-D imaging method in the following section.

3.3.4. X-ray Nanotomography Imaging

Although advantageous in terms of its chemical mapping capabilities and spatial resolution, the electron microscopy imaging and elemental mapping results could only produce a 2-D description of the complex microstructure of the composite material. To achieve a truly 3-D quantitative description of the composite, the 3-D microstructure of the material was measured using x-ray nanotomography (XNT), which I performed on the transmission x-ray microscope (TXM) at the National Synchrotron Light Source, beamline X8C. Element-sensitive XNT measurements were performed at x-ray beam energies above and below elemental absorption edges, in order to invoke substantial elemental contrast in the absorption images. For the materials in this study, tomographic imaging spanning the Fe K-edge (7112 eV) and Gd L_3-edge (7243 eV) was performed by imaging at 7090, 7200, and 7280 eV, as shown in Fig. 32. Approximations of x-ray absorption behavior shown in Fig. 32 suggest distinguishing the expected phases by the following criteria[52]:

- GDC: no change across Fe K-edge, very small increase across the Gd L_3-edge
- CFO: increase in attenuation across Fe K-edge, flat across Gd L_3-edge
- GFCC: attenuation increases across both Fe K- and Gd L_3-edges

- Pore: negligible attenuation at all energy levels

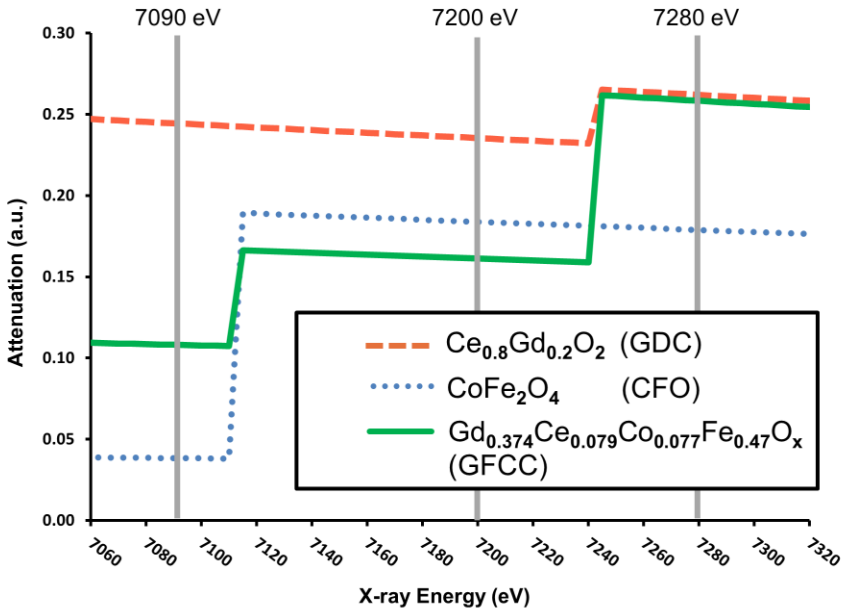

Figure 32: Density-based approximations show x-ray absorption behavior spanning the Fe K-edge (7112 eV) and the Gd L_3-edge (7243 eV). XNT imaging was performed at 7090, 7200, and 7280 eV to span both absorption edges and identify the solid phases based on their contrast change across each edge. Figure from [166].

The sample used for the XNT measurements was prepared by lab-mate Alex Cocco using FIB-SEM. The sample was then mounted in the TXM at NSLS, with a zone plate providing 30 nm spatial resolution. For each energy level (7090 eV, 7200 eV, and 7280 eV), tomography was performed by rotating the sample over a range of 180 degrees at 0.25 degree increments. At each angle, a projection image was collected with an exposure time of 20 seconds and a camera binning value of 2 (giving an image pixel size of 19.5 nm). The camera position was adjusted between each data set to maintain a consistent magnification of the sample, eliminating the need to rescale images in subsequent image processing. Each tomographic data set was reconstructed

using a filtered back projection algorithm to generate three 3-D volumes. Cross-sectional slices representative of each energy level are shown in Fig. 33(a-c).

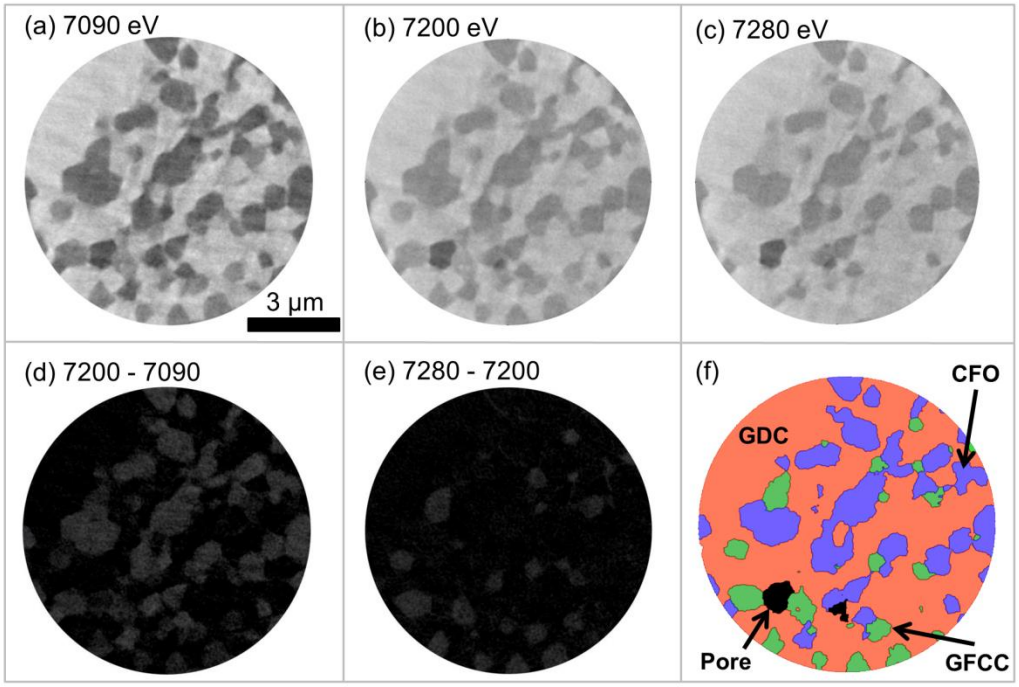

Figure 33: X-ray Nanotomography imaging of GDC-CFO. (a), (b), and (c) display cross sectional slices of the nanotomography data obtained at each energy level (Fig. 32). (d) Absorption contrast across the Fe K-edge. (e) Absorption contrast across the Gd L_3-edge. (f) Segmented, labeled structure. Figure from [166].

Minor pixilation, imaging artifacts, and outlier pixels were removed from each data set using a 3-D median filter, which replaces each voxel with the median of its value and its six nearest neighbors. Subtraction of the volumes spanning the Fe K-edge (Fig. 4d, 7200 eV – 7090 eV) and the Gd L_3-edge (Fig. 4e, 7280 eV – 7200 eV) was performed on a voxel-by-voxel basis to highlight the attenuation changes across the absorption edges and thus the elemental distributions. Using the contrast, regions belonging to each phase could be identified based on

the listed criteria. In addition, a maximum gradient magnitude map was created by taking the maximum of the gradient of Fig. 33(a-c) on a voxel-by-voxel basis. The identified phase regions and the gradient map were used as inputs to a watershed algorithm (with the identified regions serving as seeds, and the gradient map defining phase boundaries) to create a segmented structure, as shown in Fig. 33(f). The segmented structure has cylindrical geometry to retain as much usable data as possible.

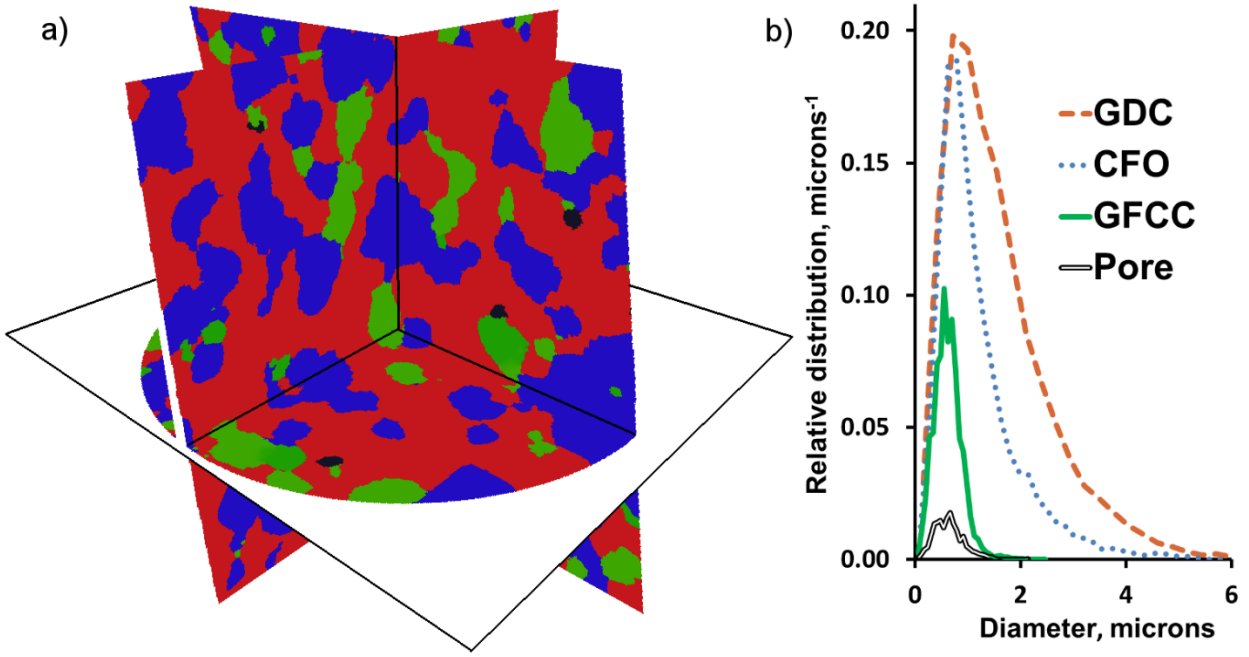

Figure 34: Visualization of the segmented structure. (a) Orthographic views demonstrate the 3-D structure. (b) Phase size distributions for the full 3-D structure. Figure from [166].

3.3.5. Characterization and Discussion

Although cross-sectional 2-D slices are shown in Fig. 33 for demonstration purposes, the entire process was conducted in 3-D. Several orthographic views of the 3-D structure are shown in Fig. 34(a). The 3-D structure was used to compute size distributions, volume fraction,

tortuosity, and contiguity of each phase. The size distributions of each phase are shown in Fig. 34(b), and the other properties are reported in Table 2. The GDC and CFO can both be characterized by a mean "particle" diameter of over 1 micron, whereas the GFCC and pore phases are mostly in the sub-micron range. The mean is evaluated on a volume-weighted basis for each phase, i.e. an equal volume of each phase is contained above and below its characteristic mean. The small size of the pore and GFCC phases helps explain why they form only isolated regions, and would likely not be substantial obstacles to transport.

	GDC	CFO	GFCC	Pore
Volume Fraction (%)	57	33	9	1
Contiguity (%)	100	96	0	0
Tortuosity	1.24	2.6	-	-
Mean diameter, μm	1.55	1.17	0.62	0.64

Table 2. 3-D volume fraction, tortuosity, contiguity, and mean size of each phase. Table from [166].

The spatial variation in the property values was tested by analyzing multiple smaller cylindrical sub-volumes of the structure. Only minor variations of the properties were observed. (See section 3.4 for a more detailed analysis of property-volume dependence). The measured volume fractions of GDC and CFO are similar to the nominal composition of the fabricated membrane (60% and 40%, respectively) with some clear loss of each phase contributing to the formation of the GFCC phase, which accounts for 9% of the structure, by volume. Pores account for the remaining 1% of the volume. As such small constituents, the pores and GFCC each consist of completely isolated regions, and form no connected percolating networks through the material. The lack of a contiguous pore structure is important in preventing gas crossover, which

would reduce the chemical potential driving force for separation applications. The formation of isolated and distinct GFCC regions may produce such effects as the geometric alteration of transport pathways and change of local stoichiometry in neighboring phases. With the pore and GFCC phases accounting for 10% of the volume, the GDC and CFO both still form nearly completely connected networks with very few isolated regions, and as such still serve as effective transport pathways with tortuosity values of 1.24 and 2.6, respectively.

Recalling from the Wagner equation, the oxygen flux through the membrane is proportional to a "total" conductivity term (if conductivity is assumed to not be a strong function of the oxygen partial pressure) which includes both the electronic and ionic conductivity in their respective phases

$$j_{O_2} \propto \frac{\sigma_{el}\sigma_{ion}}{\sigma_{el}+\sigma_{ion}} \tag{26}$$

Using the values cited earlier for bulk electronic (1 S/cm) and ionic (0.1 S/cm) conductivity in the CFO and GDC phases, we can calculate a total conductivity of approximately 0.09 S/cm. However, if Eq. 25 is used to modify the bulk values to account for the microstructure of each of the phases, the new value of total conductivity is 0.02 S/cm. Therefore, the constrictions in the transport pathways in the composite structure can be expected to cause a decrease in performance by a factor of roughly four compared to the bulk materials. This result is assuming the GFCC phase to be a perfect insulator of both transport species.

However, possible additional effects of the GFCC phase may alter this analysis, and are an area of continuing research. Considering the implications on bulk transport only, the main impact from the emergent GFCC phase formation is a depletion of Gd from the oxygen ion transport phase GDC. This reduces the Gd content from 0.2 to 0.16 ($Ce_{0.8}Gd_{0.2}O_{2-\delta}$ vs. $Ce_{0.84}Gd_{0.16}O_{2-\delta}$), resulting in a slight decrease in the bulk oxygen ion conductivity.[181]

Conversely, the possibility of some appreciable conductivity in the emergent GFCC phase and its associated new type of grain boundaries could lessen negative impacts on the membrane transport behavior, and is an area of ongoing investigation. Lastly, the formation of an emergent bulk phase, which is relatively isolated in the microstructure, may be beneficial compared to the possible additional formation of a Gd-rich interface in CeO_2 or other interfacial phases, which block ionic transport as has been observed in other MIEC material systems.[181,188]

3.3.6. Section Summary

The current work outlines a methodology of materials characterization consisting of TEM coupled with XNT for the determination of the 3-D microstructures of the bulk phases in the GDC-CFO model system with a resolution of ~30 nm. The x-ray imaging approach utilizes absorption edge imaging across multiple edges to map the distribution of Fe and Gd, which can be correlated to the GDC, CFO, and GFCC phases. Contrast across both of the edges is used to generate seeds and boundaries for a watershed algorithm to produce a segmented structure. Characterization of the structure suggests significant transport-related restrictions due to the formation of the emergent GFCC phase. However, ongoing and more detailed characterization and investigation of possible conductivity of the GFCC phase may lessen its negative impacts on the structure. In addition, future design and fabrication should consider *engineered interfaces* (i.e., grain boundaries) and *tailored defects* as a key focus area for next generation energy conversion systems including ceramic MIEC composites. This will in turn require more detailed characterization of the interfaces in MIEC composites using HRTEM and higher resolution XNT with resolution greater than ~10 nm that can potentially probe the interfacial regions resulting in

chemical information including tomographic mapping of bulk and grain boundary interfacial regions in polycrystalline materials.

3.4. Extended Membrane Study and Development of Predictive Models for RVE Size

This section addresses several tasks. First, several models are developed to provide predictive capabilities for estimating the RVE size needed to accurately measure microstructural properties. The results from the RVE models are compared to the results of an extensive imaging study of the GDC-CFO membrane system. GDC-CFO membranes have been fabricated under a variety of conditions by varying the powder ratios, sintering temperature, and sintering time. The different conditions create a variety of microstructures for testing the applicability of the developed models, and generally good agreement is found. Finally, the characterization results are used to describe the implications of the discrete microstructure on membrane performance and provide suggestions for future design.

3.4.1. Introduction to the RVE concept

In the study of multiphase composite materials, conceptually a large material domain at the device scale can be accurately represented by a smaller sub-section of the material termed a *representative volume element* (RVE). The motivation to study materials via an RVE is that it permits smaller computational and experimental domains while still maintaining a description of material behavior relevant to device performance. In essence, the RVE links the micro and macro-scales. The RVE concept has been used extensively in the field of continuum mechanics modeling to describe the stress and strain fields within composite materials.[192-198] These studies are typically concerned with predicting the effective physical properties of the material under mechanical load, namely the elastic modulus. However, with recent developments in high

resolution 3-D imaging capabilities, the RVE concept has been extensively applied in terms of accurate characterization, as well as simulation, of morphological properties in real physical systems. In particular, FIB-SEM and x-ray nanotomography methods capable of resolving the detailed distribution of multiple solid phases at the nanometer scale have helped move towards bridging the gap of understanding the connections between microscale material features and macroscale device performance.[4,37,199-201] Several researchers have explicitly considered the effect of the imaging volume size on characterization results, and some will be discussed in greater detail in following sections.[66,70,202-208]

From a characterization perspective, the goal of the experimentalist is to sample just a small portion of a total material domain, and in considering just this small region, be able to generate a description that represents the whole material. For this to be possible, an RVE extracted from any location within the material must statistically contain approximately the same structure and properties as any other randomly selected RVE. This requires the RVE to include a sufficient sampling of the variety of microstructural features that exist in the sample, such that a smaller sub-volume will contain an inadequate sampling of these features and therefore not be representative, while a larger sub-volume will contain more than a sufficient number of features and therefore will also be statistically representative. In that light, we seek a minimum RVE size, understanding that larger sub-volumes can also be used as an RVE. Implicit in this definition is the assumption that the bulk material displays a level of statistical homogeneity. In other words, on a local scale the material may have a variety of structures, phases, and complex geometries that are arranged in a specific way unique to that exact location, but on a statistical basis the effective properties of the multiphase material are uniform across a much larger length scale. This would, for example, exclude graded structures in which a property such as particle

size or volume fraction has been intentionally varied across the structure during the fabrication process.

In this study, for the sake of uniformity and general applicability, sub-volumes extracted from a total material domain will be restricted to cubic geometries. This is performed to remove some of the ambiguity involved in defining RVE sizes based purely on volume, in which case it is not clear over what range of geometry (aspect ratio and shape) that definition is applicable. For example, for some material properties, particularly those aimed at describing pathway-type transport properties, the characterization results will almost certainly not be the same for two RVE's with very different aspect ratios even if the total volume is the same due to the influence of the boundaries. Therefore, the cube has been chosen here as the standard shape.

The challenge to the experimentalist is that when imaging is to be performed on a given sample, the minimum RVE size to obtain accurate characterization results is generally not known *a priori*. Furthermore, the necessary size of an RVE may vary depending on the material property in which the researcher is interested. In the literature, typically 3-D image data is therefore analyzed after imaging to asses if volume-independent conditions have been met. In an effort to provide some predictive capabilities, this work outlines simplified models aimed at estimating the minimum RVE size for several common microstructural properties: volume fraction, phase size distribution, and network contiguity. The models are then compared to experimental results obtained through extensive x-ray nanotomography imaging of a multi-phase composite oxygen separation membrane.

3.4.2. Predictive Models

The models presented in the following sections use geometric simplifications of the complex and random microstructures that are often found in real materials. The simplified systems allow the variations in the structure to be described with a statistical basis in a tractable manner, with the understanding that the results serve only as approximations for real microstructures. Specifically, the models are designed for composite systems consisting of two or more phases (with pores treated equivalently to a solid phase), composed of randomly distributed particle-like features of relatively uniform size and exhibiting long-range statistical homogeneity. Many such materials are fabricated by the mixing and pressing of various powders, followed by sintering at high temperature. During the sintering process, the powders densify to form the particle-like features considered in this work. Numerous researchers have also used a simulation approach to generate material microstructures by random packing of spherical particles within a volume, sometimes followed by a simulated sintering process.[206-209] It is realized that for most materials, the concept of a "particle" is an abstraction, as neighboring features which are in close contact frequently form a contiguous network rather than an array of isolated particles. Understanding this distinction, it is assumed that these complex structures can still be represented approximately as an assembly of particles, some of which are in close contact with their neighbors due to the sintering process. For phases forming a contiguous structure, the terms "particle size" and "feature size" are thus used interchangeably. In addition to the references mentioned above, the idealization of real microstructures as random arrangements of particles of various phases has been used numerous times in the literature to develop analytical descriptions of device performance.[7,210-212] Certain features which may exist in real materials are not covered in this framework, including possible non-random agglomeration of particles of a certain phase, large disparities in structural/particle length scales,

highly anisotropic features such as fibrous or planar structures, and graded structures. Therefore, the descriptions presented are not universally applicable, but rather apply to a certain class of particle-like materials. As a cubic RVE size is sought for each property, we introduce a convenient description to scale the size of the cube

$$L^* = \frac{CubeEdgeLength[\mu m]}{ParticleSize[\mu m]} \tag{27}$$

The parameter L* provides a measure of the size of a cube by using the number of particles per side as the measuring unit. The measure of average particle size is an approximation made by the researcher, and is meant to be a characteristic length of all particles/features in the microstructure.

3.4.2.1. Analytical Model for Estimation of Volume Fraction RVE Size

From a simplified geometric perspective, composite materials can be thought of as a 3-D arrangement of particles of various phases (solid particles and pore "particles"). In this model, the particles are assumed to be of constant size, randomly-located, independent, and densely packed. In reality, close contact and sintering between neighboring particles may create interconnections of somewhat smaller size than the "particles" themselves. However, in the evaluation of volume fraction, it is acknowledged that most of the material volume of a given phase is contained in the "particles" themselves rather than these tenuous connections. Therefore, sintered regions of varying (smaller) size than the constituent particles are not explicitly considered. While these are substantial simplifications, they allow for the development of a simple model when little is known about a real material *a priori*.

A certain fraction, *p*, of the particles belong to a given phase of interest, and any such particle belonging to that phase is denoted as a "success". The probability that a particular

particle is a success is simply given by *p*, and the probability that the particle belongs to any other phase (not success) is 1-*p*. The identity of a particle doesn't provide any indicator of the identity of its neighboring particles. Given p and a sampling of n random and independent particles, the probability of observing a given number of successes n_i follows the binomial distribution. (For a real material, the volume fraction of the phase, *p*, is not known *a priori*. In fact, it is the volume fraction itself which the researcher is trying to accurately determine via an RVE. However, in this formulation p can be treated as a researcher's estimate of the volume fraction. The estimate can be provided based on known fabrication conditions or preliminary pilot studies of the material).

The mean number of successes if *n* total particles are sampled and with a probability *p* of success on any given particle is given by

$$\mu = n_i = np \tag{28}$$

and if sampling of *n* total particles is repeated many times, the standard deviation of the number of successes is

$$\sigma = \sqrt{np(1-p)} \tag{29}$$

The mean and the standard deviation in Eqs. 28 and 29 are both in terms of number of particles. However, to compute the volume fraction ϕ of a phase, we are interested in the fraction of particles which belong to that phase. We therefore divide by the total number of particles *n* to obtain the expected mean μ_ϕ and standard deviation σ_ϕ of the volume fraction of the phase of interest.

$$\mu_\phi = \frac{\mu}{n} = p \tag{30}$$

$$\sigma_\phi = \sigma / n = \sqrt{\frac{p(1-p)}{n}} \tag{31}$$

The expected volume fraction of a phase is exactly equal to the probability that any individual particle belongs to that phase. The standard deviation of the volume fraction under repeated sampling depends on the probability *p* as well as the number of particles n in each sample. The larger the number of particles sampled, the smaller the variation in the measurement of a phase's volume fraction. Because the discussion is limited to cubic geometries, the dimensionless cube length L* can also be written as

$$L^* = n^{(1/3)} \tag{32}$$

Combining Eqs. (31) and (32),

$$\sigma_\phi = \sqrt{\frac{p(1-p)}{L^{*3}}} \tag{33}$$

and rearranging provides

$$L^* = \left(\frac{p^*(1-p)}{\sigma_\phi^2} \right)^{(1/3)} \tag{34}$$

Equation 34 predicts the size of an RVE given a guess for the volume fraction *p* and the variation the researcher is willing to accept in their measurement in terms of the standard deviation of the volume fraction σ_ϕ. Equation 34 is plotted in Fig. 35 over a complete range of possible *p* values and several values of σ_ϕ, linearly spaced between 0.01 and 0.1.

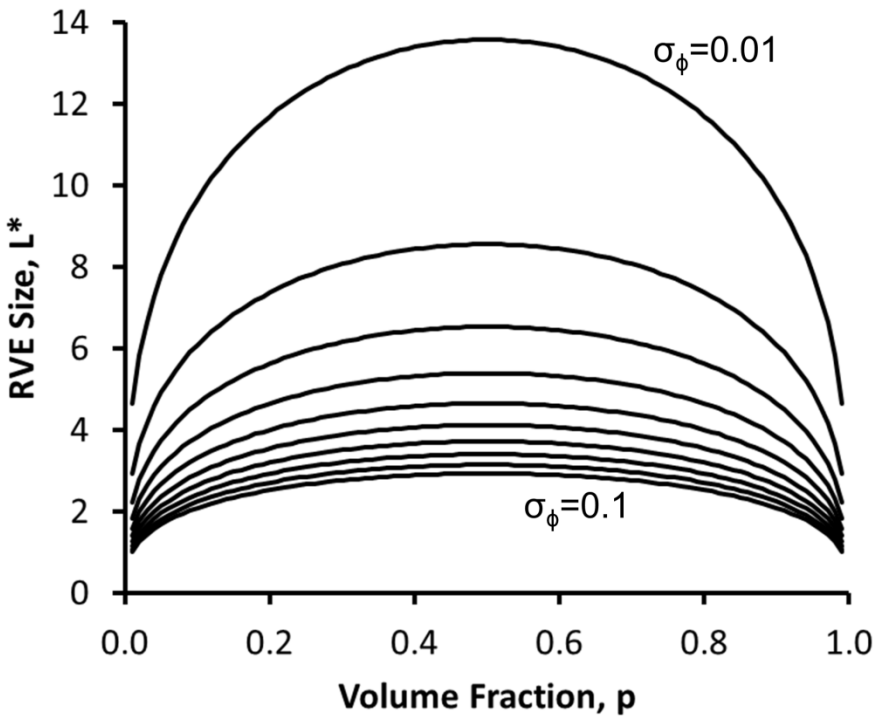

Figure 35: Analytical predictions for RVE size required for measurement of volume fraction. The required RVE size is a function of the researcher's estimate of the volume fraction, *p*, and the tolerable standard deviation in the results σ_ϕ.

Examining Fig. 35 leads to several conclusions. Most significantly, the size of an RVE will depend on the level of precision the researcher requires. For example, if the researcher has a phase with an estimated volume fraction of p=0.5 and would like to know the true volume fraction within a standard deviation of 0.01, an RVE of size L*~14 would be required. However, if knowing the exact volume fraction is not very important, and a standard deviation of 0.1 is tolerable, then an RVE of size L*~3 will suffice.

Secondly, the RVE size is dependent on the estimated of *p*. Very small and very large volume fractions can be measured with relatively small RVEs. However, to measure a moderate volume fraction with the same level of precision requires a larger RVE.

The model developed in this work is similar to a model used by Kanit et al., which also approaches the determination of a microstructural volume fraction property from a statistical sampling viewpoint.[192] In that way, the approach taken in this work for measuring volume fraction is not new, but there is a key difference in the metric which is used to define the microstructural length scale at which individual features exist. In this work, a linear dimension, the mean "particle" size, is used to define the characteristic size of the microstructural features. The size of the sampling volume is then specified relative to this dimension through the use of L*. Kanit et al.'s approach utilizes the mathematical concept of *integral range*, which provides a measurement of characteristic feature size in units of volume, rather than length. A further description of the development and definition of the integral range concept can be found in referenced work.[213] The sampling volume is then defined relative to how many of these random and independent volume units must be sampled to provide a certain desired precision in the result. The end result from both approaches is quite similar, and is demonstrated in Kanit et al. for Voronoi mosaic structures, with results reported in Fig. 14 and Table 4 of the cited work.[192] The advantage of the current approach is the more simple determination of the scaling unit, notably a linear feature size rather than a characteristic volume. From an experimental perspective, it is intuitively somewhat easier to observe a microstructure in preliminary studies, such as using SEM, and create a reasonable estimation of the characteristic particle length, as opposed to the volume, based off 2-D images. (Of course, that characteristic length could be raised to the third power to create a volumetric description of the characteristic feature size if desired). In addition, the characteristic length scaling used in this work also provides a convenient and consistent framework for determining sampling volumes for particle size and network contiguity properties, which are covered in the subsequent sections.

3.4.2.2. Analytical Model for Estimation of Phase Size Distribution RVE Size

Although in the previous formulation all particles of all phases were assumed to be equal in size, in reality there is some distribution of particle sizes for each phase. In a similar fashion to the previous derivation, we would like to have an estimate of the RVE size required to accurately capture this distribution for each phase.

Intuitively, to describe the distribution of particle sizes for a phase, it is necessary to sample a sufficient number of those particles such that the full span of possible sizes has been included in the sample. The problem is one of statistical sampling which asks how many items must be sampled from a population in order for the sample distribution (and therefore the sample statistics) to be representative of the population distribution. In this model, the sample mean particle size is used as the sample statistic. A sample size which consistently produces the correct sample mean can only be achieved if the sample itself includes a representative and consistent distribution of the constituent particle sizes. Assume $\sigma_{pop,i}$ is the standard deviation of particle sizes for the entire population of particles of phase *i* throughout the total material domain. The central limit theorem of statistics states that if many samples of n_i particles of phase *i* are taken from a population, and the mean particle size of each sample set is computed, the sample means will follow a normal distribution with the same mean as the population and a standard deviation given by

$$\sigma_i = \frac{\sigma_{pop,i}}{\sqrt{n_i}} \tag{35}$$

where σ_i is the standard deviation in the measurement of mean particle size when samples of n_i particles are taken from the population. Rearranging equation (35) leads to,

$$n_i = \left(\frac{\sigma_{pop,i}}{\sigma_{des,i}} \right)^2 \tag{36}$$

where the standard deviation of the sample means has now been relabeled as the researcher's desired standard deviation $\sigma_{des,i}$. This is the variation the researcher is willing to tolerate in the computation of the mean particle size of phase *i*. If the researcher does not need to know the particle sizes with much certainty, $\sigma_{des,i}$ will be relatively large, and therefore the number of phase *i* particles which need to be included in the sample is relatively small. Conversely, if the researcher would like to know the sizes of phase *i* particles with a high level of precision, the acceptable standard deviation $\sigma_{des,i}$ is relatively small, and a large number n_i of particles will need to be sampled.

It is realized that phase *i* particles account for only a fraction of the total particles in the system, approximately by

$$n_i = p_i n \tag{37}$$

where p_i is the estimated volume fraction of phase *i*, and *n* is the total number of particles in the system. By combining Eqs. (32), (36), and (37),

$$L^* = \frac{\left(\frac{\sigma_{pop}}{\sigma_{des}} \right)^{(2/3)}}{p^{(1/3)}} \tag{38}$$

Equation (38) provides an analytical expression for RVE size (where the subscript *i* has been dropped for clarity) as a function of two estimated parameters and one constraint. The estimated parameters, *p* and σ_{pop} represent the researcher's estimates of the volume fraction of the phase and the standard deviation of particle sizes they expect across the total material domain. Neither is known *a priori*, but can be approximated based on fabrication conditions, preliminary pilot

studies, or micrographs. The ratio of the standard deviations in the numerator will be referred to as the SD ratio.

Plots of L* vs. *p* for a range of SD ratios between 1 and 10 is shown in Fig. 36.

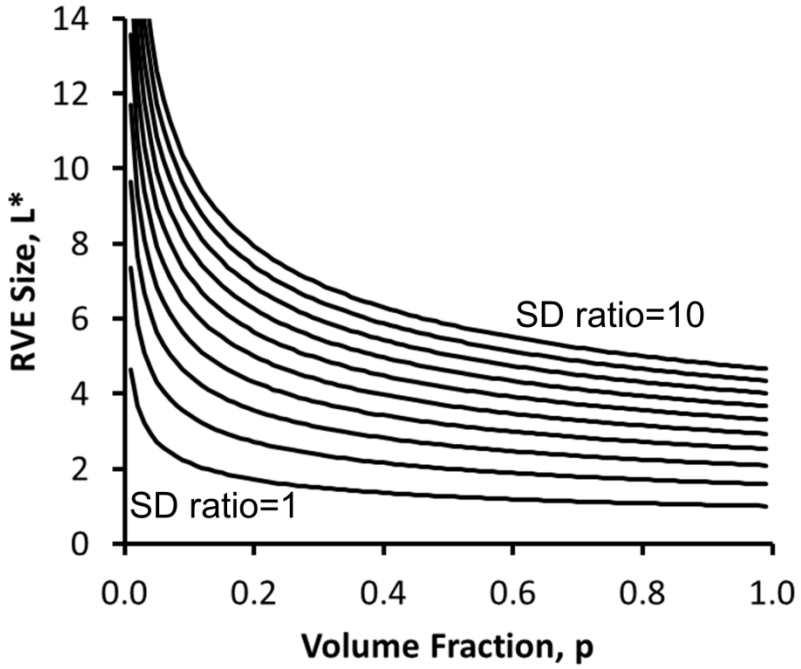

Figure 36: Analytical predictions for RVE size required for measurement of particle sizes. The required RVE size is a function of the researcher's estimate of the phase's volume fraction *p*, the estimate of the standard deviation of particle sizes which exist in the sample σ_{pop}, and the tolerable standard deviation in the measurement of the mean diameter σ_{des}.

Examination of Fig. 36 yields some qualitative observations. As expected the RVE size depends on the level of precision the researcher requires. A large SD ratio (indicative of a wide variation of particle sizes in the population and/or a small acceptable variation in the results) requires a larger RVE to sample enough particles. A small SD ratio (indicative of minor variations in particle sizes and/or a large acceptable variation in the results) permits a smaller

RVE to be used. Secondly, phases that account for a small volume fraction generally have substantial separation between their constituent particles, and therefore a larger total sample of the material needs to be analyzed to capture a sufficient number of the particles. A phase accounting for a high fraction of the volume, on the other hand, has particles located in close proximity to one another within the sample, so less total material needs to be sampled to obtain the same number of particles of that phase.

3.4.2.3. Simulation Model for Network Contiguity

The development of a descriptive model for network contiguity is somewhat more difficult than the previous descriptions. In the previous sections, simplified analytical models were developed for measurement of volume fraction and particle size distribution. In these cases, simple models are easy to implement due to the inherent local nature of those measurements. However, the description of network contiguity is complicated by the fact that the network depends on the long range order of the structure. The contribution of a single particle to a transport process within a network cannot be described considering that particle alone, it is necessary to look at the amount and spatial distribution of the other particles to which it is connected (or not connected).

3.4.2.3.1. Percolation Theory

Guidance for the analysis of network properties can be found in existing analytical and numerical work in percolation theory.[214-216] In general, percolation theory is concerned with describing the long-range connectedness of particle networks in an infinite domain. The discussion of percolation theory in this paper is far from comprehensive, and is focused only on

the connection of theory with real data from an experimental characterization point of view. First, some general concepts must be introduced. Particles within an infinite domain can exist in one of two possible states:

1) The particle can belong to a particle cluster which is isolated and finite in size. The size of the cluster can range from 1 particle to the theoretical size of infinity minus one.

2) The particle can be a part of a cluster which extends in size to infinity. Such an infinite cluster will be called a percolating network, or simply a network.

Percolation theory provides some useful tools to describe this behavior. At the most basic level, a percolation threshold can be defined, which serves as a cut-off differentiating systems which contain only isolated clusters from systems which contain an infinite network. This percolation threshold is typically defined in terms of a critical volume fraction of a given phase, denoted ϕ_c:

$\phi < \phi_c$ Only isolated clusters exist

$\phi > \phi_c$ An infinite network exists

A number of works have aimed at predicting the percolation behavior in composite materials in two or three dimensions.[210-212,217-220] Typically, the composite structure is simplified to an easily tractable geometrical model with a given type of packing (such as simple cubic, body-centered cubic, random, etc. and defined by particle coordination number, Z) of a binary system of spheres. Using the packing structure and the sizes of particles comprising the various phases, analytical expressions have been developed to predict the percolation threshold of each phase. For example, previous results suggest that when the phase of interest has small features/particles (relative to the other phase), its percolation threshold is lower than for the mono-sized particle case, and therefore a smaller volume fraction is required to form a

percolating network.[211,218,219] Conversely, a phase consisting of relatively large particles is expected to have a somewhat higher percolation threshold.

Results from Bouvard et al. suggest that although the value of the percolation threshold ϕ_c changes when particle size ratio is varied, the general behavior in the vicinity of the threshold remains similar (see Fig. 3 in Bouvard).[217] This behavior is depicted in Fig. 37. A phase below the percolation threshold contains only isolated clusters, and if more particles of that phase are added to the system and the volume fraction increased, the size of the isolated clusters would grow, but they would remain distinct from one another (regime 1). When the volume fraction of the phase is increased to near the threshold, large clusters of particles exist, and the subtle yet significant difference between non-percolating and percolating networks will be due to a seemingly minor local change in particle placement which has long-range implications. A phase just above the percolation threshold forms a connected and infinite network by bridging the gaps between some of the existing isolated clusters. While there is a nearly a 100% chance that such an infinite network exists above the threshold, there can still be isolated clusters which are not a part of the network. Therefore, the particles would have some probability of being connected to the infinite network, and some probability of being part of a finite isolated cluster (regime 2). To continue the process, if more particles are added and the volume fraction increased farther, more and more of the isolated clusters become connected to the network, and a smaller fraction remain isolated (regime 3). During that process, the larger isolated clusters have a higher likelihood of becoming attached to the network than the smaller isolated clusters, so as the volume fraction of the phase increases the average size of the remaining isolated clusters becomes increasingly small. If the process of adding particles is continued to the limiting case of

occupying the entire volume, 100% of the particles are connected to the infinite network and there are no isolated clusters of any size remaining.

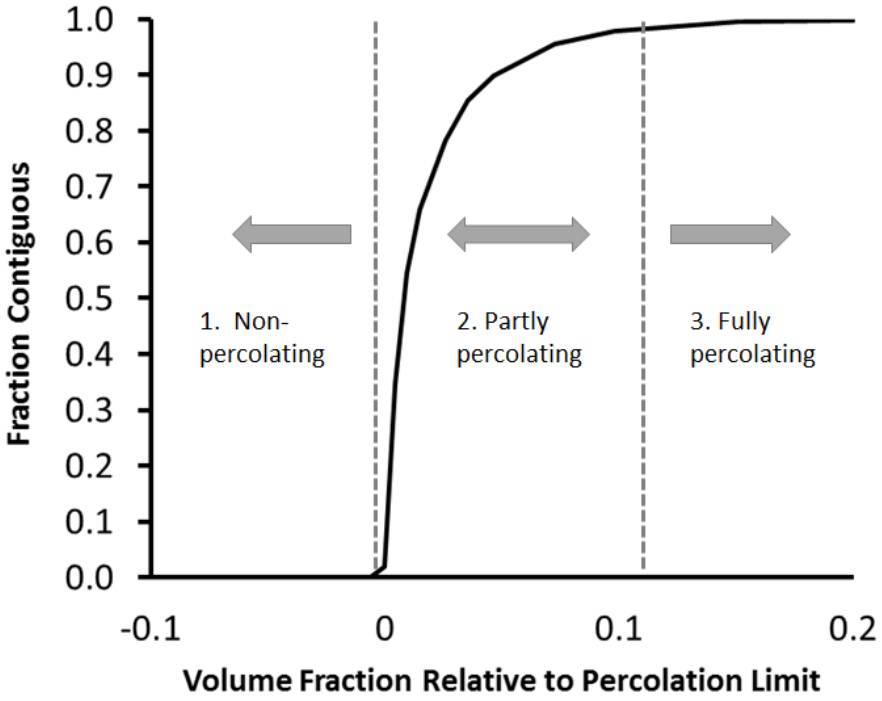

Figure 37: Percolation behavior can be qualitatively described in terms of three regimes. The results shown here are for percolation on a simple cubic lattice in 3-D. In regime 1, a phase is below its percolation threshold and there are no percolating paths. In regime 2, a phase is just above the percolation threshold, and some particles are connected to a percolating network. In regime 3, a phase is well above the percolation threshold and nearly all particles are connected to the network.

3.4.2.3.2. Simulation Methods

To describe network contiguity in the context of the RVE analysis, analytical theory will be complemented by a simulation approach. Simulation is able to capture the randomness and

long-range effects that impact the structure when the composition is near the percolation threshold, which is critical in the cases where the "averaged" behavior predicted by the analytical theory is not sufficiently descriptive. By repeating many simulations, we can obtain estimates of percolation thresholds, the connectedness of the network at compositions near the threshold, the statistical variation of properties amongst replicate volumes of the same size and composition, and the relative amounts of particles which contribute to percolating networks versus those which remain isolated. Most importantly, within the framework of the RVE concept, simulations can also provide insight into how these descriptions of the network change as a function of volume size L*.

A number of researchers have previously performed computer simulations to describe percolation. Most work has focused on determining the percolation threshold itself rather than the contiguity and size-dependence of the network phenomenon. For example, a number of past simulation studies have shown the threshold for site percolation on a simple cubic lattice is given by a site fraction f_i =0.3116.[221-224] However, if the sites are assumed to be occupied by spherical particles rather than cubic sites, which is a more realistic approximation of real materials, conversion from the site fraction f_i to the volume fraction ϕ_i of the spherical particles is simply given by a geometrical adjustment

$$\phi_i = f_i \frac{\pi}{6} \tag{39}$$

Thus the volume fraction of a phase of interest at the percolation threshold for a simple cubic lattice is about ϕ_c=0.16, which is quite similar to the value of ϕ_c=0.187 reported by Kuo and Gupta for percolation of randomly-placed spheres in a continuous medium.[218] In fact, the volume fraction percolation threshold in 3-D has been shown to be relatively insensitive to the packing structure in the case of monosized spherical particles.[210,217,225]

In addition to calculating the percolation threshold, at least a few studies have explicitly reported the size of the simulation domain relative to the particle size. Powell et al. found that when the composition of the material is near the percolation threshold, an L* value greater than 20 is needed to reliably capture the transition from non-percolating to percolating structures.[225] When the composition is not near the percolation threshold, an L* of 20 or less may be appropriate, more so the farther the composition is from the threshold.

Bouvard et al. performed more extensive simulation studies, and found that when particle size was made too large (akin to L* too small), significant scatter was present in the results when the material composition was near the percolation threshold.[217] The authors attributed this effect to too few of the large particles being present in the domain to provide a good statistical measure of the network. When particles were made smaller, and thus L* values larger (in the vicinity of L*=40), the data was more reliable. However, for most cases the authors did not analyze replicate volumes at a given size and composition, so they were not able to report a variation in results due to random statistical variations in particle placement. In addition, for a given particle size the authors did not simulate domains of different sizes to determine the impact of the total simulation volume on the percolation behavior.

Suzuki and Oshima presented a percolation model for a multi-component mixture of spherical particles aimed at estimating particle coordination numbers.[220] Computer simulation with randomly-generated packed sphere structures with L* ranging from 7.5 to 15 was used to confirm the validity of the model. However, the study was not explicitly interested in variation of percolation behavior with domain size, and the overall contiguity of particles of a certain type was not reported.

Simulation studies performed by Acharyya and Stauffer as well as Jan and Stauffer examined percolation behavior of networks with the composition fixed at the percolation threshold.[223,224] The authors report the fraction of percolating domains, which they call the critical spanning probability, as well as cluster sizes. The results are found to depend on boundary conditions, the dimension of the lattice, as well as domain size. In 3D, lattice dimensions in excess of L*=1000 were examined with result appearing to reach asymptotic values at around L*=100, indicating volume independence.

Additional simulations have been performed by several authors with the intention of describing the microstructure of a particular device, namely a solid oxide fuel cell composite electrode.[206,208,209,211] Bertei *et al.* found that using simulation domains with dimensions L*=16x16x48 generally gave less than 2% variation amongst replicate random volumes for a variety of investigated properties including contiguity, tortuosity, mean pore size, and triple phase boundary length. The authors also observed the same percolation behavior as shown in Fig. 3 (presented as Fig. 4 in Bertei *et al.*) for the pore phase, albeit at a low volume fraction owing to the small "particle" size of the pores. Kenney *et al.* used cubic simulation domains with L* equal to approximately 25 for measuring properties on structures above the percolation threshold. However, for all measurements the authors averaged results over 20 random replicate structures, and did not report the variation between individual replicates. Lastly, simulations of electrode microstructures by Cai *et al*. gave consistent measurements (within an acceptable variation of 10%) of percolated triple phase boundary density for L*>7.5. The simulations were performed for three interconnected phases with volume fractions of 0.215, 0.350, and 0.435.

The simulations presented in this work build upon those previously reported. In particular, the current simulations aim to analyze the variations in network percolation for

replicate cubes of the same size and same composition, as well as cubes of varying size. Studying these variations will help provide an estimate of the size L* required to accurately describe the overall material network properties.

The simulated structures used in this work are generated in the following manner. Particles of all phases are assumed to be mono-sized spheres and occupy sites on a simple cubic lattice. Site percolation, as opposed to bond percolation, is considered in this work. The lattice itself is a cube of prescribed dimension L* on a side, and contains 2 phases: the phase of interest with a particle fraction of f_i, and the "other" phases grouped collectively as not belonging to the phase of interest with particle fraction $(1-f_i)$. The cubic volume is considered one lattice point at a time, and each lattice point has a probability f_i of being labeled as a particle of the phase of interest. After each lattice point has been considered, a number n_i of them have been labeled as particles of the phase of interest, occupying approximately, but not necessarily exactly, a fraction f_i of the total possible lattice sites.

Simulation domains are generated varying L* between 6 and 100, and f_i between 0.02 and 0.9. For each combination of cube size L* and composition f_i, 30 random replicate volumes are generated. In each replicate, the placement of spheres occurs at random lattice locations, and therefore the replicates are all different (and can conceptually be thought of as different samples extracted from the same total material domain), accounting for the variations in long-range structure that can be seen even in samples with the same size and composition.

Each cube is analyzed using a painting algorithm to determine its contiguity. The algorithm follows a similar procedure as the Hoshen-Kopelman algorithm and starts by searching iteratively through the volume for a particle of the phase of interest which has not yet been marked.[226] Once found, that particle is marked, and its nearest neighbor lattice points (6

neighbors exist in 3D) are examined to see if any of them contain unmarked particles. If so, those particles are marked, and their neighbors are examined, and so on. The procedure continues until all particles connected to the single original particle have been given the same marker. The search through the volume then continues until a new unmarked particle is found. That particle is then marked with a new marker and its neighbors examined in the same fashion. The algorithm terminates when all particles have been marked. Two implementations of boundary conditions have been investigated: free boundary conditions and periodic boundary conditions. Free boundary conditions are physically equivalent to symmetry boundaries on all 6 sides of the cube. For periodic boundaries, one coordinate direction is arbitrarily chosen as the transport direction, and periodic boundaries are applied in the remaining two directions. The two cases are presented because, although it has seen some discussion in the literature, there is not yet a consensus on the most appropriate type of boundary condition when measuring pathway-type properties on experimental RVEs.[67,70,71,205] After the labeling algorithm is complete, all particles connected to a common cluster have the same marker, while separate clusters have a different marker. In the limiting case where all particles are connected, they will all share the same marker. Conversely, if every particle is completely isolated, each will be labeled by a unique marker.

Every cluster is then examined and classified based upon its connectedness to the cube boundaries. For the case of free boundary conditions in all 6 directions, the classifications are:

- A cluster intersecting all 6 faces of the cube is considered contiguous.
- A cluster that does not intersect any of the cube faces is an isolated cluster.
- A cluster that intersects at least 1, but less than 6, of the cube faces is a dead-end cluster.

For the case of periodic boundary conditions with a defined transport direction

- A cluster intersecting the 2 faces of the cube in the transport direction is considered contiguous.
- A cluster which does not intersect either of the faces in the transport direction is isolated.
- A cluster which intersects only one of the faces in the transport direction is a dead-end cluster.

For both cases, the term contiguity refers to the fraction of particles connected to a contiguous (percolating) cluster based on the definitions above.

Before discussion of the results, it is important to recall that each cube is conceptually considered to be a sub-volume extracted from within a much larger domain. The domain, presumably the entire device with some large but finite size, may contain clusters which are contiguous, isolated, or connected only at certain boundaries as dead-ends. However, when a sub-volume is extracted from an arbitrary location within the domain, new boundaries are artificially created and clusters are truncated. Therefore, there exists the possibility for the clusters within the sub-volume to be categorized as an incorrect cluster type. For example, a cluster which may be large but isolated in the total domain may, by chance, happen to intersect all faces of a small sub-volume cube and be incorrectly categorized as contiguous. Conversely, a contiguous network in the total domain may intersect a sub-volume cube only partially, leading to the incorrect categorization of "dead-end" particles. The prevalence of these categorization errors will depend on the sub-volume size as well as its composition relative to the percolation threshold. In general, large sub-volumes and/or compositions away from the percolation threshold will have fewer errors than small sub-volumes and/or compositions near the percolation threshold. This idea follows intuitively from the earlier discussion on cluster size.

3.4.2.3.3. Simulation Results

Simulation results are presented in Fig. 38 for several different values of L*. Results are reported in terms of the contiguity as a function of the volume fraction relative to the percolation threshold, which as discussed previously is approximately ϕ_c=0.16 for monosized spherical particles in 3-D. Panels (a)-(d) are the results for free boundary conditions, and panels (e)-(h) are for periodic boundaries. On each plot, a black line is included to show the expected behavior in the limit of an infinite domain. This was approximated by fitting a curve through the data points for the domain of L*=100, as the scatter was very minimal and thus the data seemed to be approaching the infinite limit. The black curves are almost exactly identical for the two types of boundary conditions. It is apparent that for the free boundary conditions, at small L* the data seem to lie beneath the black curve, while for the periodic boundary conditions they have a more even spread around the black curve. This can be explained considering that for free boundary conditions, isolated particles located on the domain boundary will never be labeled as connected, and therefore the fraction of contiguous particles is underestimated. Conversely, for periodic boundaries, particles located on the domain boundary have some chance of being connected to the structure on the opposite side of the domain via periodicity. Therefore, the placement of the particle on the boundary is no different than any other location in the interior of the volume.

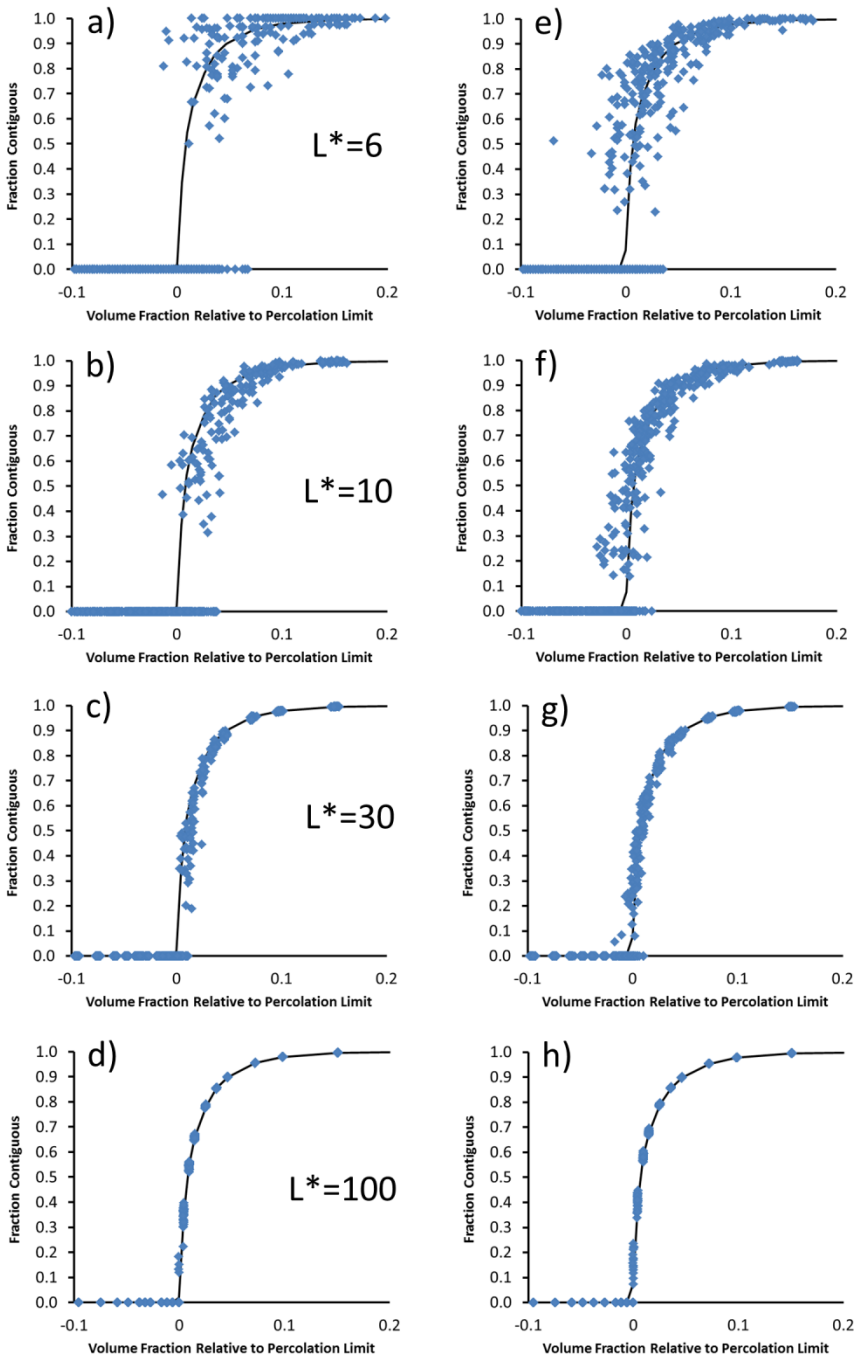

Figure 38: Results for contiguity of simulated structures. Results are shown for four different cube sizes, L*=6, 10, 30, and 100. (a)-(d) are obtained using free boundary conditions with no preference to transport direction, while (e)-(h) are obtained assuming a primary transport direction and implementing periodic boundary conditions in the orthogonal directions.

The effects of sub-volume size can be described using Fig. 38. For L*=6, substantial variation in the contiguity is observed close to the percolation threshold for both types of boundaries. There are numerous instances where the volume fraction of the phase is below the threshold, yet the cube displays percolating behavior, and there are also many instances where the volume fraction is greater than the threshold yet cubes display completely non-percolating behavior. Both of these cases represent errors introduced by the small volume size near the percolation threshold. Furthermore, the spread of data in the horizontal direction provides evidence of the difficulty in interpreting experimental results. This is largely because when a real sample is examined experimentally, the percolation threshold of a phase is generally not known, so it is also unknown whether the phase is above or below the threshold. So for example, if a cube of L*=6 is measured experimentally to have a contiguity of 0.8, then that phase could actually have a composition ranging from just below the percolation threshold to a nearly 100% percolating phase. Likewise, if a single cube is measured to have a contiguity of 0, it could correspond to a material with a contiguity which is actually zero, or could be as large as roughly 90%. Clearly the measurement of a single small volume is not useful to the experimentalist for either type of boundary. However, measurements taken on replicate small cubes could be beneficial and provide more evidence as to the material's composition relative to the percolation threshold. For example, if the researcher measures a single cube and gets a contiguity of 0, but then measures several other samples and gets results in the range of 0.7-0.9, it could be reasonably concluded that the sample is almost certainly above the percolation threshold, and most particles are connected to a percolating network. The true value of contiguity is likely in the range of 0.7-0.9, and the first measurement is likely an erroneous measurement.

Interpretation of the results is much more straightforward when large volumes are used. As percolation theory has been developed in the hypothetical context of an infinite domain, as the simulated or experimental cube size is made very large, the results obtained will approach the infinite limit and become independent of boundary conditions. This behavior can be seen for $L^*=100$. For a given measured contiguity, there is no longer any ambiguity of where the true material lies relative to the percolation threshold. A measured contiguity value of 0.5, for example, can only correspond to a phase which has a volume fraction about 0.01 greater than the percolation threshold. In addition, a measured contiguity of 0 is certain to mean the material is at or below the percolation threshold, and a measured contiguity of 1 or nearly 1 is certain to mean the material is well above the percolation threshold and nearly completely contiguous.

It is therefore up to the researcher how much uncertainty is tolerable. If one would just like to know whether the phase is in percolation regime 1, 2, or 3, described in Fig. 3, then it might be sufficient to simply measure several small samples, say of $L^*<10$. If all samples have contiguity of zero, it is likely the bulk material does as well, and is in regime 1. If the samples have some mix of contiguity between 0 and 1, then the bulk material is close to the percolation threshold and is located in regime 2. If all samples measure a large contiguity, of nearly 1, it is likely the bulk sample is well above the percolation threshold in regime 3.

However, if the researcher is interested in a more exact and quantitative measure of the fraction of contiguous particles, or would like a single cube which displays representative behavior for subsequent quantitative modeling for example, a small volume will not suffice and a larger cube must be examined. In this case, the closer the composition to the percolation threshold and the higher the accuracy desired, the larger the cube must be. For example, if a researcher suspects or knows their material to be well above the percolation threshold, this could

be confirmed by making measurements on a cube of L*=10. For a cube of L*=10, if the results indicate a very high contiguity, say greater than 95%, it can be confirmed using Fig. 38 that the material is in fact well above the percolation threshold with a high contiguity. But alternatively if the researcher suspects their material is close to the percolation threshold, L*=10 will not be sufficient as a significant spread of results can occur for this volume size. In this case, a larger volume, perhaps L*>30, will be necessary to produce the desired accuracy near the percolation threshold.

From an experimental perspective, the applicability of each of the types of boundary conditions must also be considered. In reality, a physical sample would not be expected to display a periodic or repeated symmetric structure. Therefore, the use of either in characterization of real materials is an additional approximation of the larger structure, and will be discussed further in a following section comparing the simulations to experimental measurements.

3.4.3. Experimental Measurements of GDC-CFO Membranes

A number of previous experimental studies have aimed to quantify an RVE size for material characterization. Several are briefly mentioned here to provide context for the following discussion of the characterization performed in this work. Shearing *et al.* used x-ray tomography to examine the microstructure of a graphite electrode for a lithium-ion battery.[202] After imaging, the domain was sub-divided into a number of smaller sub-volumes of different sizes to analyze the variation in properties. An RVE was defined when the standard deviation of results at a given size was considered adequately small, although this criteria was not strictly defined. In this manner the authors determined an RVE size for specific surface area to occur for

a volume of 43x60x60 microns, and for tortuosity to be at least as large as the entire sample, 43x348x478 microns. Although not stated in the paper, the mean particle size visually appears to be about 20-30 microns based on a 3-D rendering. Metcalfe *et al.* used a simulation approach to generate and analyze structures of composite solid oxide fuel cell electrodes.[204] The group was most interested in the triple phase boundary length (TPBL), and defined an RVE as existing when less than 3% variation existed amongst replicate volumes of the same ratio of pore, ionic, and electronic phases. Such a criteria was used to determine a cubic RVE volume of L*=14. Measurements of the effective TPBL based on only contiguous structures were also performed at a single composition and provided similar results. The authors also acknowledged that significant variations of the effective TPBL could exist when one of the composite's phases is near its percolation threshold, increasing the necessary size of the RVE.

Lombardo *et al.* used x-ray nanotomography to evaluate a variety of properties for a composite SOFC anode composed of nickel and yttria-stabilized zirconia (YSZ).[66] The approach evaluated a single cube for several different values of L*, and defined an RVE when the characterization results did not vary significantly between successive L* sizes. Large YSZ particles were found to cause significant fluctuations in the results for low values of L*, and the approach suffered from not evaluating replicate sub-volumes for each L*. Nevertheless, it was concluded that particle size distribution, tortuosity, and properties involving the YSZ phase required the largest RVE's, in excess of roughly L*~6.

Laurencin *et al.* also used x-ray tomography to study Ni-YSZ, but used a slightly different imaging procedure capable only of distinguishing solid from pore.[70] A large total volume was imaged, which was split into numerous smaller sub-volumes to analyze the variation

in porosity and tortuosity for different sub-volume size. For both properties, an RVE was obtained for L*=14.6 based on sufficiently small variation of results.

Lastly, Joos *et al.* used FIB-SEM imaging to characterize an SOFC cathode consisting of a single porous solid phase.[205] The imaged volume was split into 3 smaller sub-volumes and characterized in terms of porosity, tortuosity, and specific surface area. The size of the 3 sub-volumes was varied and RVE size was determined based on the variations between the sub-volumes as well as the results for different sub-volume sizes. It was found that the porosity and tortuosity of the pore phase could be measured using a volume of 5.25x5.25x10 microns, while measuring tortuosity of the solid phase required 5.25x5.25x20 microns. An RVE for specific surface area was not conclusive as the results showed variation even at large sub-volume sizes. The solid particle size is reported to be about 0.5 microns.

3.4.3.1. X-ray Nanotomography Imaging

GDC-CDO membranes fabricated using the same starting materials as in section 3.3 were used for comparison to the developed models. The initial work described in section 3.3 also revealed an additional solid phase, denoted GFCC (suspected formula $Gd_{0.374}Ce_{0.079}Co_{0.077}Fe_{0.47}O_x$), which emerges during high temperature sintering in the membrane fabrication process.[37] The same sample preparation and imaging procedures were used in this section to examine membranes fabricated under 5 sets of processing conditions, four of which are listed below:

1) 50/50 GDC-CFO ratio, sintered at 1300C for 2 hours
2) 60/40 GDC-CFO ratio, sintered at 1300C for 2 hours
3) 80/20 GDC-CFO ratio, sintered at 1300C for 2 hours

4) 80/20 GDC-CFO ratio, sintered at 1300C for 5 hours

The fifth set of conditions (80/20 GDC-CFO ratio, sintered at 1400°C for 2 hours) produced samples with very large feature sizes compared to the other four conditions. Presumably this is due to the higher sintering temperature. Because of the large features, nanotomography measurements could only be performed on samples containing a small number of microstructural features, corresponding roughly to L*=1 or 2. Therefore, the samples are certainly too small to provide representative volumes, and are omitted from this study. Three cylindrical samples of each processing condition were prepared by FIB-SEM milling (performed by Alex Cocco), followed by x-ray nanotomography imaging performed at the Stanford Synchrotron Radiation Lightsource (SSRL, beamline 6-2c) and the National Synchrotron Light Source (NSLS, beamline X8C). Again, nanotomography was performed spanning the Fe k-edge and Gd L_3-edge to map GDC, CFO, GFCC, and pore phases. At both beamlines, a zone plate lens providing 30 nm spatial resolution was used. Microscope configuration and imaging parameters were similar for each sample, but slight adjustments were made according to the capabilities of the particular beamline. For example, when experimental time was constrained, imaging was performed at the 3 energy levels reported in section 3.3: 7090, 7200, and 7280 eV. But when time was not a factor, such as due to the shorter exposure times required per image at SSRL, tomography could be performed at 4 energy levels to more precisely span each of the absorption edges: 7095, 7130, 7230, and 7260 eV.

The image processing for each sample was performed in the same fashion as section 3.3. The data sets were reconstructed using a filtered back-projection algorithm, and contrast across the absorption edges was used to generate seeds for a watershed segmentation algorithm

implemented in MATLAB. The output of the watershed is 3-D digitized structures with the phases denoted by an integer label of 1, 2, 3, or 4 on a Cartesian grid.

3.4.3.2. Statistical Characterization Approach

Testing the existence of an RVE requires sampling random and independent cubic sub-volumes of the material and observing the variation in properties among them. Because each cylindrical sample was extracted from a random location on the membrane, each selected sub-volume from within the cylinder can also be considered random. But particular attention must be paid to ensure samples are also independent. Two volumes which overlap or are in very close proximity to one another will not be independent. To avoid such a scenario, it is useful to define a separation distance, specific to the particular material, at which microstructural features at two locations are not correlated. For this purpose, we introduce a definition of covariance, which in the x-direction is written as[70,192]

$$K_x(h) = \frac{1}{V}\int I(x,h,y,z)dV \tag{40}$$

$$\text{where} \quad I(x,h,y,z) = \begin{cases} 1 & \text{if } k(x,y,z) = k(x+h,y,z) \\ 0 & \text{if } k(x,y,z) \neq k(x+h,y,z) \end{cases}$$

To evaluate Eq. 40, a cubic volume of material is first extracted from the segmented data set. For the purposes of determining the covariance, the largest possible cube is taken from the reconstructed data as to include as much material, and therefore produce as accurate a measurement, as possible. The covariance of the cube with itself, as a function of the offset distance *h*, gives a measure of the scale over which the microstructural features are correlated. A typical result applying Eq. 40 to a sample in this study is shown in Fig. 39(a).

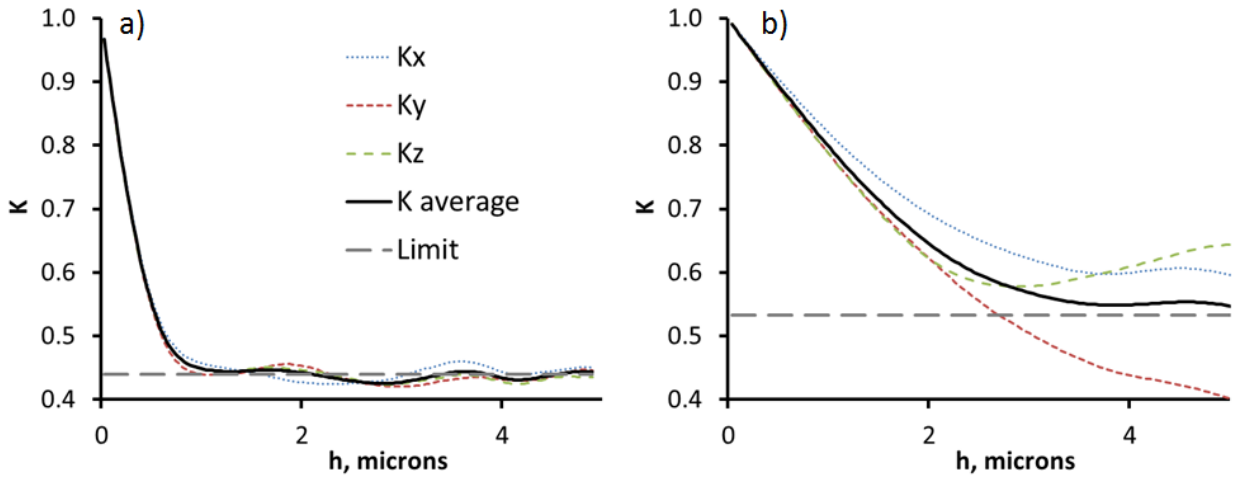

Figure 39: Covariograms for two different samples. In (a), a sufficiently large volume of material is sampled to produce a covariogram which display the expected asymptotic limiting behavior. In (b), very large features relative to the volume size prevented the measurement of a meaningful covariogram.

At small *h*, a structure is highly correlated with itself, and K is close to a value of 1. As *h* increases, the correlation decreases and asymptotes to the value of the sum of the volume fractions of each phase squared, as in Eq. 41.

$$K_x(h) = \sum_i \phi_i^2 \qquad h \to \infty \tag{41}$$

The asymptotic limit indicates uncorrelated structures, and can be used to define a correlation length. Following the definition used by Laurencin et al., the correlation length is defined as the offset *h** at which the covariance is within 5 percent of its asymptotic value,[70]

$$\frac{K_{ave}(h^*) - \sum_i \phi_i^2}{\sum_i \phi_i^2} \le 0.05 \tag{42}$$

It should be noted that the method outlined above to determine the correlation length is, in itself, subject to the RVE volume independence concept. Therefore we arrive at a case of circular logic: the correlation length is being used in a process to help determine the RVE size for a number of other properties, but the correlation length itself cannot be rigorously calculated without knowing the RVE size. While this is true, in practice it has not been a significant issue for two reasons. First of all, the definition of correlation length in Eq. 42 is somewhat arbitrary and should be seen as an approximation. It is meant to give an estimate of the length scale over which structures are correlated. Secondly, it is typically clear when not enough material is available for Eq. 42 to produce meaningful results. This has been illustrated in Fig. 39(b). It can be seen that the covariance in the x, y, and z directions is not similar, and furthermore do not seem to asymptote towards the expected value. This behavior occurs when the cube is small compared to the size of the microstructural features, and indicates not enough of these features have been sampled to provide a meaningful covariogram and correlation length. This has been observed in particular for the samples of processing condition #5, which were not analyzed any further in this work.

Once the correlation length is known, it defines the minimum spatial separation at which two adjacent samples can be considered independent. It is a property of that sample's microstructure. With this notion in mind, for a given size L* we wish to extract as many independent cubic samples from the tomography data as possible. The tomography results, consistent with the shape of the FIB-prepared samples, are cylindrical and due to imperfect mounting of the cylinders on the pin during the preparation process are frequently tilted relative to the Cartesian grid, creating oblique cylinders. A simple geometric search routine has been written in MATLAB to determine the number and locations of cubes of a given size L* that can

be extracted from within the constraints of the sample geometry and the required separation distance h^*. Logically, the number of cubes that can be extracted depends on both L* and h^*. This procedure can be repeated for different desired L* using the same tomography data and same h^*. The results of the cube extraction routine for 2 different cube sizes are shown in Fig. 40. Note, to test the RVE concept, each cube will only be compared to others of the same L*, therefore cubes of different sizes are allowed to re-sample the same data.

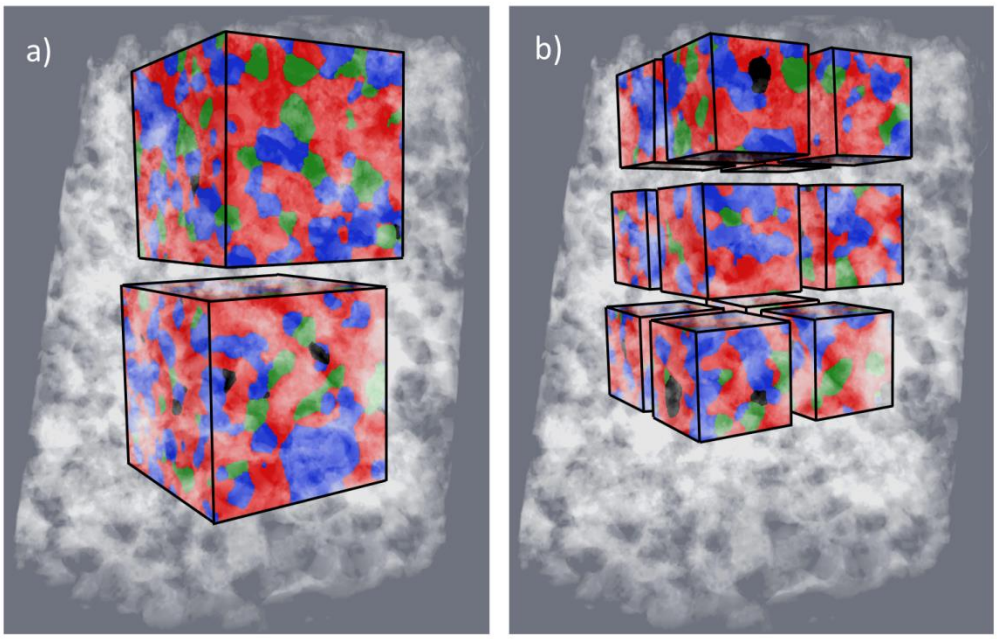

Figure 40: Cubic sub-volumes are extracted from within the cylindrical samples analyzed using x-ray nanotomography. Cubes of different sizes are used, while maintaining a separation between cubes equal to the sample's covariance length h^*. Cubes of edge length 6 microns (a) and 3 microns (b) are shown.

Owing to the geometry of the cylindrical samples, the largest cube that could be extracted from most samples was 7 microns on a side. Throughout each cylindrical sample, as many cubes as possible were extracted with 7, 6, 5, 4, and 3 micron dimensions. The exact size and

orientation of the cylindrical samples dictated how many cubes of each size could be extracted. The number obtained for each size is shown in Table 3. To express the cube dimensions in terms of L*, an average characteristic particle size must be chosen to represent the denominator in Eq. 27. This number is an approximation that must be estimated by the researcher, and for this work was taken as the average *h** for all samples created using processing conditions #1-4. The estimate for average particle size was thus taken as 0.77 microns. The cubes measured experimentally in this study therefore correspond approximately to L*=3.9, 5.2, 6.5, 7.8, and 9.1.

Sample ID #	Processing Conditions	Location	7 μm L*=9.1	6 μm L*=7.8	5 μm L*=6.5	4 μm L*=5.2	3 μm L*=3.9
1	1	SSRL	2	2	3	6	16
2	4	SSRL	0	0	2	3	3
4	3	SSRL	0	0	2	3	6
5	2	SSRL	1	2	4	4	12
7	1	NSLS	1	2	2	6	12
8	4	NSLS	1	1	2	4	12
10	3	NSLS	1	2	2	4	12
11	2	NSLS	2	2	2	6	16
12	1	NSLS	1	2	2	5	12
13	3	NSLS	1	1	2	4	12
14	2	NSLS	2	2	2	6	16
15	4	NSLS	1	2	2	2	6

Table 3: The experimental data used in this study, including the processing conditions, where imaging was performed, and the number of cubes of each size that were extracted from each sample.

Each cube was analyzed using a set of microstructural characterization codes.[67,68] Properties obtained through the characterization include the volume fraction of each phase, the size distribution of the "particles" of each phase, the contiguity (or isolation) of

that phase's network structure, and the tortuosity of the contiguous networks. Some of the codes have been modified slightly from their original formulation, as described below.

The ray tracing method described by Grew *et al.* and used in this work to determine phase sizes has been modified to provide an improved manner of handling domain boundaries.[67,68] Following the RVE definition, a cubic volume which we would like to use as representative and descriptive of the total sample could conceptually be replicated and repeated spatially, in a tile-like fashion, to recover the full size of the total sample and with a consistent set of properties and behavior. Therefore, a cube for which we are testing the concept of volume independence can be treated as if it were a single structural unit. Such a representation can be achieved through the use of symmetry boundary conditions at each of the 6 faces of the cube. Rays that are launched from within the structure during the ray shooting routine can either i) intercept another phase of material, thereby terminating the ray propagation, or ii) reach the boundary of the cubic volume. In previous implementations of the code, rays of type (ii) were terminated and tabulated along with those of type (i). However, a more realistic implementation within the framework of the RVE concept is to impose symmetry boundaries and have rays "bounce back" into the structure and continue propagating until another phase is intercepted and terminates the ray. Figure 41 shows examples of several rays used to measure the red phase, including one which intercepts the top boundary of the domain and follows the symmetry boundary condition. This methodology will provide a more accurate description of the structure because it prevents the premature termination of rays at the cube boundary, which is not a true physical boundary within the material but rather a boundary created by cropping of the sub-volume from a larger domain. After all possible rays have been measured a number-weighted mean particle size is calculated by the arithmetic mean of all ray lengths.

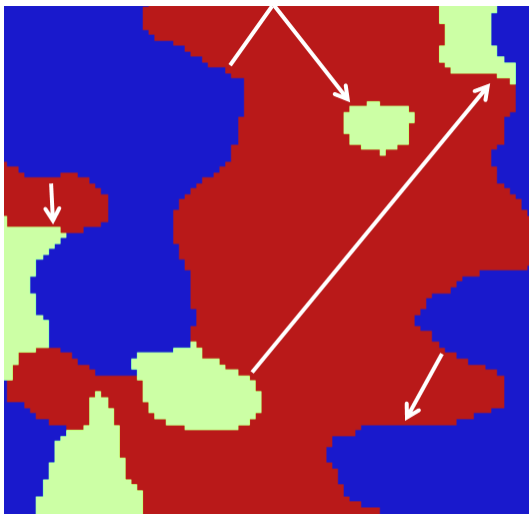

Figure 41: Depiction of the ray shooting method to measure the size distribution of the red phase. Implementation of symmetry boundary conditions is demonstrated with the ray on the top boundary of the domain.

Contiguity of the real structures is measured using the same region-growing method used for the simulated structures, which has been modified slightly from the version presented by Grew *et al*. to provide the symmetry and periodic boundary condition cases described previously.

3.4.4. Comparison of Models and Experimental Measurements

3.4.4.1. General procedure for Anderson-Darling Goodness-of-Fit Test

For each L* and each of four processing conditions, a finite number of independent cubes were analyzed, as described in Table 3. Conceptually however, a nearly infinite number of such cubes could be analyzed if experimental time allowed. From a statistical perspective, this nearly infinite number represents the total population of possible cubes which could be examined. In order to have an RVE, it is this total population which we desire to have a standard deviation of

properties less than or equal to some acceptable value σ. But since in reality only a very small sub-set of the population has been analyzed, we must perform a statistical test to determine if the sub-set could have come from the total population of cubes with standard deviation σ (for the volume fraction model, $\sigma = \sigma_{\phi}$ and for the size distribution model, $\sigma = \sigma_{des}$).

Specifically, the group of cubes for each L* and each processing condition is tested to see if it could have been taken from a hypothesized normal population of cubes with the same mean property value as that of the group, and standard deviation σ. Because of the relatively small sample sizes of the empirical data, the Anderson-Darling (A-D) goodness-of-fit test is used which compares the cumulative distribution function of the hypothesized normal distribution with that of the ordered empirical data.[227] The hypothesized normal distribution is defined as having the same mean as the experimental data and standard deviation σ. The null hypothesis of the test states that the data came from a population with the specified normal distribution, while the alternative hypothesis states the data came from a different distribution. A p-value significance level of p=0.05 was used for all cases. A p-value of less than 0.05 indicates rejection of the null hypothesis, while a p-value greater than 0.05 fails to reject the null hypothesis, indicating the data may have come from the specified normal distribution and therefore displays the requirements for an RVE. The test was performed using the built in Anderson-Darling function in MATLAB (adtest) for each phase of the material, each property (volume fraction and mean particle size), L* value, and processing condition. (The A-D test was not applied to the experimental contiguity results, as will be discussed in a following section). In certain cases, the data were clearly non-normal due to being close in value to the minimum or maximum of their range, such as volume fractions very nearly equal to zero. In these cases, the goodness-of-fit test based on a normal distribution is not valid, and the variation in the data has

instead been considered sufficiently small to define an RVE when the total spread is less than $2*\sigma$.

3.4.4.2. Model for Volume Fraction RVE

Comparison of experimental data with the RVE model for volume fraction is performed in the following manner. First, an acceptable standard deviation of results σ_ϕ is chosen as 0.02 for this work. This means that I seek a cube size for which, if many cubes of that same size were extracted from the total material and analyzed in the same manner, the variation in the measurements of volume fraction would have a standard deviation of 0.02 (or 2%).

Next, the experimental results are analyzed using the A-D test to determine at which L* the required condition of σ_ϕ =0.02 is met. The experimental data is analyzed separately for each phase within each set of processing conditions #1-4. An example of the data is shown in Fig. 42 for the volume fraction of the CFO phase from processing condition #2. This data set passed the A-D test at L*=7.8. Therefore, any cube larger than this size will be representative. The lower limit for the volume representative cube size is somewhere between L*=7.8 and L*=6.5. Because the experimental sampling has been performed for discrete cube sizes, it is unknown exactly where in this range the true limit occurs, and is therefore reported as the L* at which the A-D test is first satisfied, which for this example is L*=7.8.

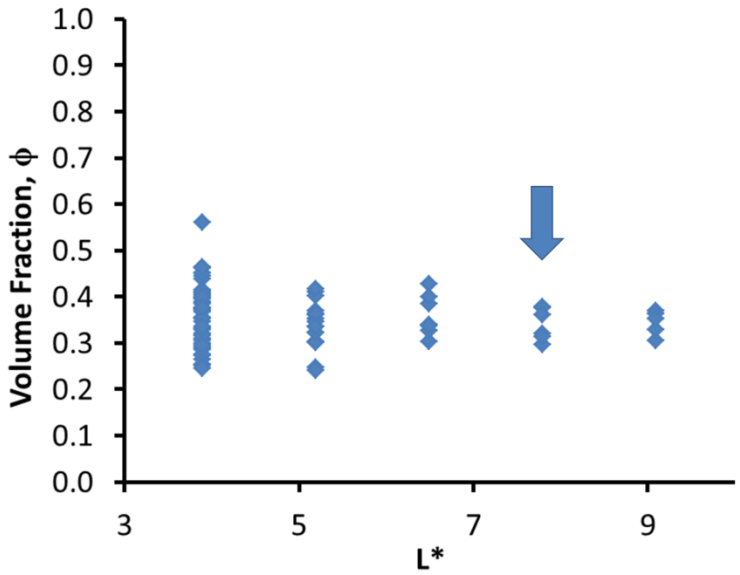

Figure 42: Experimental results for the volume fraction of the CFO phase in the sample produced using processing condition #2. The blue arrow indicates the value of L* at which the data passes the Anderson-Darling test with σ_ϕ =0.02.

A comparison of experimental results (4 phases and 4 processing conditions for a total of 16 data points) and the analytical model for fixed σ_ϕ =0.02 is shown in Fig. 43. The green data points indicate instances in which the A-D test was not valid due to non-normal data, which is just at very small volume fractions as expected. The volume fraction *p*, which in a real application of this method is estimated by the researcher, is taken as the average volume fraction of the phase over all 7 micron (L*=9.1) cubes measured for that processing condition. The experimental results show reasonable agreement to the model, with the largest RVE sizes required for compositions with volume fractions close to 0.5. In addition, in most cases the model is conservative and over-predicts the necessary RVE size, although a number of exceptions are seen at very small volume fractions. This could be due to the strong non-normality of the data near the limit of its range.

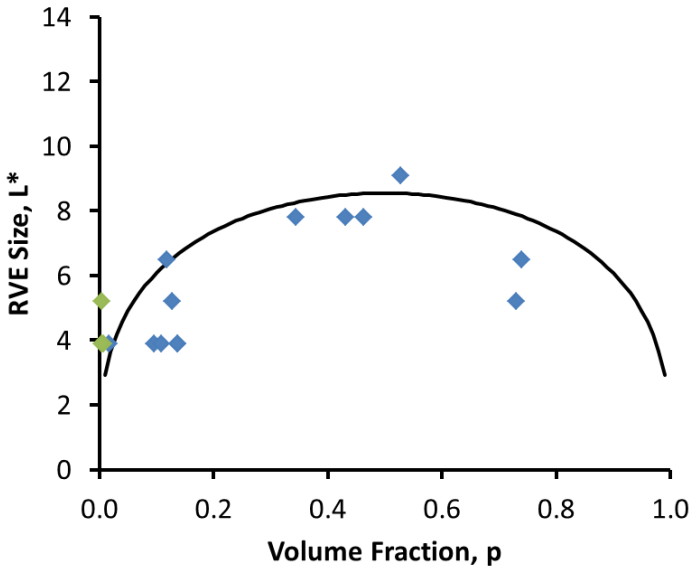

Figure 43: Comparison of the volume fraction RVE model with experimental results for fixed σ_ϕ =0.02. The model is shown by the black curve, while the points represent experimental results. The green points are instances where strongly non-normal data prevented the use of the Anderson-Darling test, as discussed in the text.

For the property of volume fraction, additional comparisons can be made to data in the literature. The results presented in Joos *et al.* suggest an RVE of about 250 microns^3 (corresponding roughly to L*=12) for accurately measuring porosity of 0.49 within a standard deviation of about 0.01 (based on Fig. 7 in Joos *et al.*), which is in reasonable agreement to the model.[205] In addition, Laurencin *et al.* calculated an RVE size of L*=14 for measuring porosity of 0.5 also with accuracy of about 0.01, which is in similar agreement.[70]

3.4.4.3. Model for Phase Size Distribution RVE

The comparison of data to the PSD model is done in a similar fashion. The comparison is performed using a fixed SD ratio of 10. An estimate for σ_{pop}, the standard deviation of particle sizes in the sample, must be provided by the researcher. In this work, rays obtained during the ray-shooting routine on the 7 micron cubes of the various samples were used. The standard deviation of lengths of all pore, GFCC, CFO, and GDC rays from the 7 micron cubes was measured, providing values of σ_{pop}= 0.31, 0.27, 0.63, and 1.05 microns, respectively. The SD ratio was then used to calculate σ_{des} which was used in the A-D test to evaluate the experimental data.

Experimental results are shown as data points alongside the analytical model curve in Fig. 44. A green arrow is also shown, indicating a location where 3 data points had very small volume fractions, and large enough cubes were not analyzed to satisfy the RVE criteria. The arrow indicates that the size of the RVEs for those phases must therefore be larger than what was measured.

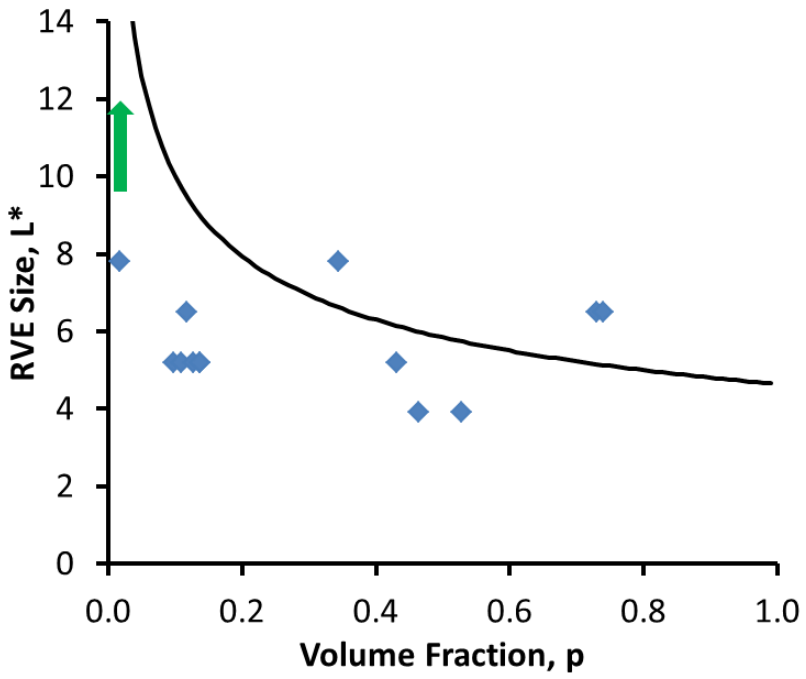

Figure 44: Comparison of the size distribution RVE model with experimental results for a fixed standard deviation ratio of 10. The model is shown by the black curve, while the points represent experimental results. The green arrow is meant to depict several instances where an RVE size was not determined (and must therefore be larger than the maximum size which was measured).

Reasonable agreement between the data and model is shown in Fig. 44. Some discrepancies seem to appear at the high volume fractions, where a larger RVE is required experimentally than dictated by the model. However, measurements are still reasonably close to the prediction curve, validating that it provides a reasonable starting point for the prediction of RVE dimensions needed for measuring particle sizes.

3.4.4.4. Model for Network Contiguity

The simulation approach presented in this paper to describe network contiguity does not provide a closed-form prediction equation as was found for the other two properties. Rather, the variation observed in simulated structures is meant to provide some general guidance in the planning of experiments as well as the interpretation of the results for real structures. The contiguity of the GDC-CFO samples in this study was analyzed using the symmetry boundary condition formulation described previously. Symmetry boundaries are chosen in an effort to produce realistic geometric features at the boundaries because they ensure smooth and continuous particle surfaces without creating new, artificial surfaces at the boundaries. Periodic boundary conditions, on the other hand, would generate jagged and discontinuous surfaces when the domain is stacked periodically with itself, and are therefore considered to be a conceptually

poor representation of the structure. (Note, in the infinite limit with large cube sizes, the material at the boundaries becomes insignificant in comparison to the internal volume, and the distinction of different boundary conditions is no longer important). The interpretation of most results was trivial. For the 4 processing conditions and 4 phases considered, 15 out of the 16 phases contained clusters which were either very nearly completely contiguous or completely isolated for all L*. However, interesting results were found for the CFO phase of processing condition #2. For condition #2, the CFO volume fraction was found to be about 34% and the contiguity of the phase as a function of L* is shown in Fig. 45.

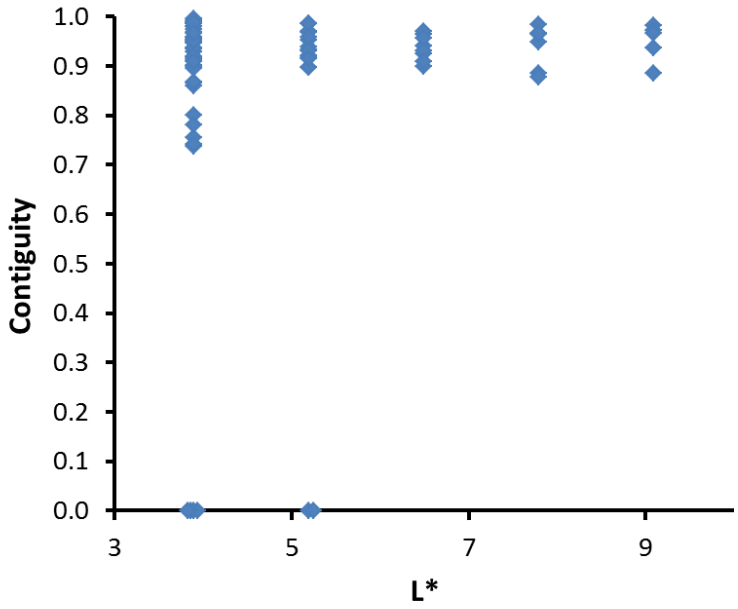

Figure 45: Experimental results for the contiguity of the CFO phase of the sample produced with processing condition #2. Free boundary conditions were used to measure contiguity.

Comparison of this result with the simulation results in Fig. 38(a)-(d) can help provide a description of the structure. At small L* (L*<6) erroneous experimental measurements can be observed describing zero contiguity. Likewise, the simulations predict significant scatter of

results for L* = 6, even when the phase composition may be well above the percolation limit, as shown in Fig. 38(a). However, at larger L* the experimental errors are not present, and there is a fairly narrow spread of values between 0.9 and 1. Comparing the experimental data points at L*=9.1 to the simulation data for L*=10 in Fig. 38(b) suggests the phase is likely at least 10% above its percolation threshold. As described earlier, the percolation threshold predicted by Kuo and Gupta for spherical particles in a 3-D continuous matrix is about 18.7%, meaning a 10% increase would be about ~29%.[218] This is fairly close to the measured volume fraction of the CFO (34%), indicating the simulations provide a reasonable means of analyzing real data. If the material is thus assumed to be about 10% above its percolation limit, the simulations for very large L* (L*=100) provide a predictive capability for the infinite material, and suggest a true contiguity value of about 0.97.

3.4.4.5. Outlook for RVE Models

While only three morphological properties were considered explicitly in this work, we present hypotheses for two additional properties. First, accurate measurement of specific surface area (or in the case of a multi-phase system, interfacial contact area or triple phase boundary length) is expected to follow the accurate measurement of volume fraction and particle size. It is intuitive to infer that, in order to quantify the interfacial characteristics between two phases, each phase itself must be accurately quantified. If the description of volume fraction or particle sizes of a given phase contains a large amount of uncertainty, so should the description of that phase's contacts with its neighboring phases.

In addition, the required RVE size for measurement of network tortuosity is expected to follow a similar trend as that of network contiguity. Tortuosity, which is the ratio of an effective path length divided by nominal path length, is written as:

$$\tau = \frac{L_{eff}}{L} \tag{43}$$

A number of researchers have implemented algorithms for measuring tortuosity on real structures.[67,69,70,73,202] The methods broadly fall into two categories: effective diffusion-type simulations and geometric pathway measurements, which are discussed in detail by Chen-Wiegart et al.[69] In both cases, the measurement of the tortuosity will depend first and foremost on having a structure which is representative of the contiguity of the network. In this sense, the tortuosity measurement can be thought of as a more detailed description; while the network contiguity provides information on whether or not a network is connected, the tortuosity provides information as to how specifically it is connected and the geometric effectiveness of those connections from a transport perspective. Therefore, it is hypothesized that an RVE for tortuosity measurements must be at least as large as an RVE for the contiguity measurement as described above.

3.4.5. GDC-CFO Membrane Characterization Results

Using the criteria described above, representative cubic volumes were obtained for almost all phases for volume fraction and mean particle diameter properties. Exceptions were noted for determining particle sizes of the pore phase due to its very small volume fraction in all samples. It was also noted that nearly complete contiguity or complete isolation of particles occurred for all phases in all samples with the exception of the CFO phase from processing condition #2, which displayed a very high, but somewhat less than 100% contiguity.

It is understood that volumes larger than the minimum RVE size will also be RVE's, and should display even less variation in properties. Therefore, a number of microstructural properties are reported in Table 4, based on the average value obtained for the 7 micron cubes of that processing condition. The number of such cubes was different for each condition, dependent on the particular size and shape of the cylindrical samples that were examined by x-ray nanotomgography, and is reported in the top of the table. Because each 7 micron cube should individually provide a result within acceptable accuracy (with the exceptions mentioned above), the average of multiple cubes provides a further improved estimator of the true property value.

		Condition #1 50/50 1300°C, 2 hr			Condition #2 60/40 1300°C, 2 hr			Condition #3 80/20 1300°C, 2 hr			Condition #4 80/20 1300°C, 5 hr		
Number of 7 μm cubes		4			5			2			2		
Volume Fraction (%)	GDC	46			53			73			74		
	CFO	43			34			13			12		
	GFCC	10			11			14			14		
	Pore	1			2			0			0		
Contiguity (%)	GDC	100			100			100			100		
	CFO	100			95			0			0		
Tortuosity		X	Y	Z	X	Y	Z	X	Y	Z	X	Y	Z
	GDC	1.4	1.4	1.6	1.3	1.3	1.3	1.1	1.1	1.1	1.1	1.1	1.1
	CFO	1.6	1.6	1.9	2.5	2.2	2.6	-	-	-	-	-	-
Mean Diameter, μm	GDC	1.49			1.70			3.16			3.32		
	CFO	1.58			1.31			1.11			1.04		
	GFCC	0.69			0.74			0.76			0.78		
	Pore	0.82			0.72			1.04			0.73		

Table 4: Microstructural Characterization of GDC-CFO membranes fabricated using four different set of conditions.

The results in Table 4 can be used to draw some conclusions about the variations in microstructure that result from the different processing conditions. Some observations are as follows

- The volume fraction of GDC and CFO decreases between 4 and 8% from their nominal values due to the creation of the new GFCC phase.
- The volume fraction of GFCC and pore is relatively constant for all conditions.
- The sintering time does not appear to be a significant factor in the microstructural properties. Processing conditions #3 and #4, which differed only by sintering time, produce very similar results.
- The GDC phase is contiguous for all conditions, while CFO is contiguous when its nominal fraction is 50% or 40%, but not 20%.
- GFCC and pore phases do not form connected networks. In the case of pore, this is especially important as connected through-pores would allow gas leakage and decrease or completely destroy the oxygen selectivity of the membrane.
- The tortuosity of GDC in all cases is quite close to 1, especially for conditions #3 and #4 with higher GDC volume fraction. Tortuosity values for CFO for conditions #1 and #2 are somewhat larger, owing to the fact that the phase is closer to its percolation threshold and the connected pathways are smaller and more tenuous, restricting transport. The tortuosity in the X, Y, and Z coordinate directions are comparable.
- GFCC and pore have a relatively constant mean diameter, in the sub-micron range, across all processing conditions. The size distribution of GFCC particles is also shown in Fig. 46. The distribution is very similar for all conditions.

- When both GDC and CFO form connected networks, as in processing conditions #1 and #2, the mean "particle" size of each is close to 1.5 μm.
- The concept of GDC and CFO "particles" is somewhat abstract when the phases form connected networks. For the large GDC volume fractions of conditions #3 and #4, the GDC effectively acts as a matrix phase in which isolated CFO, GFCC and pore particles are dispersed. In these cases, the GDC matrix can be characterized by a length slightly greater than 3 μm.

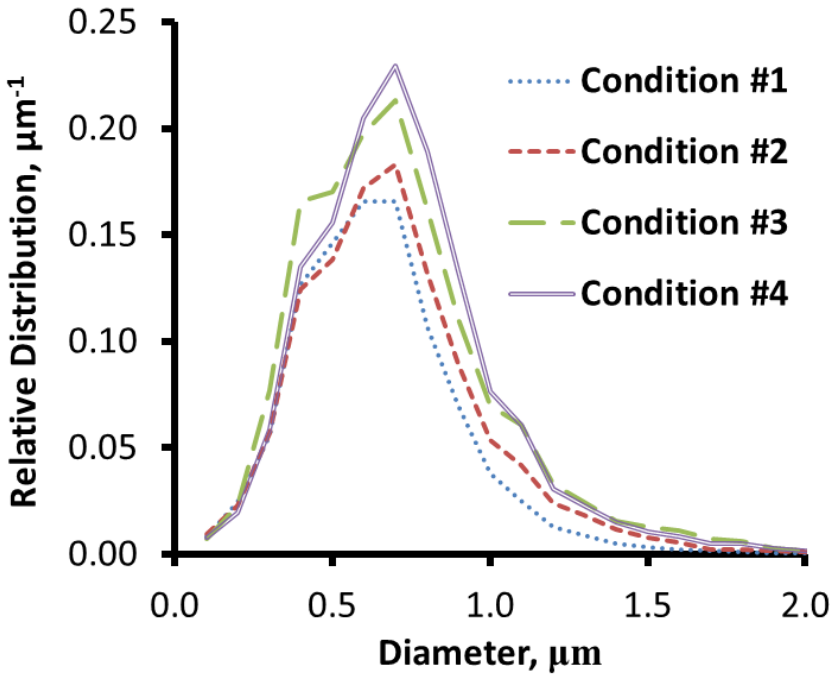

Figure 46: Particle size distribution of the GFCC phase.

The most significant result from the microstructural characterization is the loss of percolation of the CFO phase for conditions #3 and #4. While the nominal composition for each consisted of 80% GDC and 20% CFO, the decrease in the volume fraction of each during sintering resulted in a CFO phase below its percolation threshold. If the GFCC is in fact an

insulator, these membranes would be expected to be completely inoperable due to a lack of an electronic transport pathway.

However, preliminary experimental data by Kyle Brinkman's group (the team that synthesized the membranes) suggests this may not be the case. Although not yet published, early experimental measurements show appreciable oxygen permeation for each of the processing conditions. For this to be the case, GFCC would almost certainly need to display some amount of electronic conductivity to produce a percolating electron transport pathway. This is an area of ongoing investigation. More detailed analysis of the composition and crystal structure of the GFCC phase may provide valuable insight into its transport behavior.

3.4.6. Section Summary

In this work, the concept of the representative volume element for the experimental measurement of material properties is discussed in detail. The discussion focuses on particle-like composite materials with relatively uniform feature sizes and randomly distributed particles of various phases. Simple geometric models were developed to describe the measurement of properties for these types of materials as a function of the measurement volume size, described in terms of a dimensionless length L*. Analytical closed-form equations were developed for the prediction of L* for volume fraction and phase size distribution properties, while a simulation approach was used to examine network contiguity. Results of the models were compared to experimental results from a multiphase composite membrane that was imaged in 3-D using synchrotron-based x-ray nanotomography. Reasonable agreement was found between the models, experimental data, and several previous reports in the literature, providing confidence in the predictive capabilities of the models.

Extensive imaging data for the GDC-CFO system was used to infer connections between the microstructure and membrane performance for membranes fabricated using several different sets of processing conditions. The creation of the emergent GFCC phase during fabrication was found to account for about 10% of the membrane volume, at the expense of the primary GDC and CFO phases. GFCC was found to form isolated and distinct particles distributed uniformly throughout the volume. Small amounts of porosity exist in all samples, on the order of single percent, and are also isolated with no through-pores. For the 80/20 nominal ratio of GDC/CFO, the consumption of the CFO (during the creation of GFCC) led to severing of CFO transport pathways and a loss of percolation for electronic conduction. Ongoing investigations of the emergent GFCC phase should lead to a more complete description of membrane performance, possibly including some positive contribution, rather than pure degradation effects, due to the emergent phase.

4. Summary of Key Results, Conclusions, and Impacts

4.1. Results Summary

The work in this dissertation has focused on the development and application of x-ray nanotomography imaging techniques for heterogeneous functional materials. This class of materials has emerged in recent years with applications particularly in energy-related devices such as fuel cells, batteries, and gas separation membranes. These materials typically consist of multiple interconnected solid and pore phases, each of which contributes to the functionality of the device (or not contributing if it is an unintentional poisoning phase). This contribution can come in a number of forms, including mechanical stability, reaction catalysis, or solid/gas phase transport. Frequently, various reaction and transport processes are coupled at the meso- or microscale, the intermediate length scale coupling atomic crystal structure with macroscale device response. This scale, on the nano/micrometer level, contains complex microstructures of interconnected and interwoven phase networks, the specific distribution of which is intimately linked to that phase's functionality. Furthermore, these structures are typically not static, but can undergo dynamic alteration during fabrication as well as operation due to such factors as solid contamination, gas-phase poisoning, material incompatibility/reactivity, and long-term microstructural evolution. The understanding of these processes at the appropriate length scale is critical to both understanding the performance of these devices as well as developing strategies and designs for more effective materials in next generation devices.

In this work, synchrotron x-ray nanotomography has been utilized to examine some of these processes. The development and use of x-ray nanotomography, capable of imaging in 3-D with elemental and chemical sensitivity, represents a significant advance in material

characterization techniques over established 2-D or "averaged" methods. First, specific techniques were developed with application to this specific type of materials. Most simply, absorption contrast methods capable of distinguishing distinct solid phases by utilizing either density differences or absorption-edge imaging were demonstrated for several materials, including two SOFC cathode materials, one consisting of an LSM-YSZ composite and another a contaminated neodymium nickelate mixed ionic-electronic conductor.

Significant advances were made in the identification of different chemical states of the same element through full field XANES spectroscopy. The original development was performed using nickel (Ni) and nickel oxide (NiO), chosen for their applications in a number of energy devices including SOFC anodes. Performing imaging at incremental steps across the Ni K absorption edge was used to identify distinguishing spectral features of each composition which would not have been apparent using a simple absorption edge contrast method. These distinguishing features were then used to map Ni and NiO regions in a composite sample, and perform tomography to obtain the 3-D distribution of each with resolution of tens of nanometer. This advancement has significant potential to help identify regions of degradation in Ni-YSZ composite anodes which have undergone redox cycling during operation.

The proof of concept for this approach has been demonstrated by Chen-Wiegart *et al*.[113] The same XANES imaging approach was also used to examine a composite sample of Ni and Ni_3S_2, in which the spectral features distinguishing the two compositions are more subtle. For the two phase system however, it was still possible to create a spatial map of the phases' distributions. In addition, Kiss *et al.* has already used the XANES approach to complement a developing *in situ* method for observing reaction processes, along with their associated structural change, in real time using the TXM.[43]

The developed methods were applied to a number of real samples to analyze microstructure-related limitations. An alternative intermediate temperature SOFC cathode material, neodymium nickelate, was exposed to unintentional silicon contamination during fabrication. Although the contamination was, at first glance, minor at only 2-3 at%, the silicon reacted with the primary phase during sintering, creating a silicate phase covering most of the nickelate surface. As a mixed conductor, the entire exposed nickelate surface could normally be available for electrochemical activity, but the decrease in surface area resulting from the silicate formation could substantially hinder the reactions and thus increase activation losses in the electrode.

A multi-energy imaging approach was also applied to an SOFC anode exposed to hydrogen-sulfide gas. The exposure conditions, while somewhat exaggerated compared to typical poisoning levels in operating fuel cells, were used to provide an accelerated aging effect and drastic microstructural change. Imaging performed across the Ni k-edge was able to identify contrast from two different nickel-containing phases, presumably metallic Ni and a nickel sulfide compound. While a limited data set and imaging artifacts precluded the ability to match the absorption behavior to known XANES spectra, a recent improvement in zone plate optics by the beamline staff at APS permitted the acquisition of an additional tomography scan with unprecedented resolution and clarity. Additional information was also contributed by synchrotron x-ray fluorescence measurements performed by the staff at APS, which were subsequently used to confirm the identification of the second nickel-containing phase as a nickel sulfide. A segmentation approach utilizing information from both the tomography and fluorescence data was used to map the distribution of the sulfide relative to the other phases. The sulfide was found to cover most of the Ni surface, and cause a significant decrease in triple phase

boundary density. The spatial distribution of the sulfide, as a scale on the Ni surface rather than isolated and distinct particles, helps to explain the substantial performance drop seen in SOFCs exposed to extensive hydrogen sulfide poisoning.

Absorption edge contrast performed across multiple edges was used to analyze the distribution of three solid phases in a composite GDC-CFO gas separation membrane. The membrane, nominally a dual phase structure, performs gas separation by the distinct transport of ionic and electronic species through separate phases, forming a complete circuit of charge. The overall transport process is driven by a gradient in the oxygen partial pressure on either side of the membrane and eliminates the need for any external circuitry. The performance of the membrane is due in large part to the efficiency with which it transports oxygen ions and electrons across its width. However, initial electron microscopy work by collaborators Kyle Brinkman and Dong Su suggested the formation of a third, emergent phase during the sintering process due to a mild incompatibility between the primary phases. X-ray nanotomography revealed the emergent phase was characterized by distinct and isolated particles distributed throughout the dense composite ceramic. Creation of the emergent phase, at the expense of the primary phases, was found to limit the percolation of the primary phases at low volume fractions. The results directly reveal the importance of maintaining sufficient volume of each primary phase as to maintain percolating pathways, especially when the microstructure undergoes an alteration or poisoning process during sintering or operation. Continued work by Kyle Brinkman's team is expected to provide further insight into this membrane system, including a more detailed analysis of the chemical composition and crystal structure of the emergent phase, possibly even revealing some conductive properties which may enhance, rather than limit, membrane performance.

The extensive imaging of the GDC-CFO composite was also used for evaluation of several new models developed to estimate the volume size necessary to experimentally quantify various microstructural properties. Analytical expressions, based on statistical sampling, are used to estimate the RVE size for accurately measuring volume fraction and particle size distributions. A simulation approach was used to examine network contiguity, which relies on the long-range order of particle distributions, especially for phases near their percolation threshold. It was found that very large RVE's may be needed to correctly identify the contiguity state of phases near a percolation threshold, but such large RVE's may not be realistically possible using current experimental techniques (and may also be equally difficult to analyze computationally). Multiple smaller RVE's can sometimes be used instead, but caution must be exercised by the researcher to avoid false identification of contiguous or isolated regions.

4.2. Publications

The work presented in this dissertation has resulted in the following publications.

First authorship:

- W.M. Harris, J.J. Lombardo, G.J. Nelson, B. Lai, S. Wang, J. Vila-Comamala, M. Liu, M. Liu, and W.K.S. Chiu, "Three-dimensional microstructural imaging of sulfur poisoning-induced degradation in a Ni-YSZ anode of solid oxide fuel cells," *Scientific Reports*, **4**, article number 5246 (2014), DOI: 10.1038/srep05246
- W.M. Harris, K.S. Brinkman, L. Ye, D. Su, A.P. Cocco, A. Nakajo, M.B. DeGostin, Y.-C. Karen Chen-Wiegart, J. Wang, F. Chen, Y.S. Chu, and W.K.S. Chiu, "Characterization of 3D interconnected microstructural network in mixed ionic and

electronic conducting ceramic composites," *Nanoscale*, (2014), DOI: 10.1039/C3NR06684C

- W.M. Harris, J.J. Lombardo, M.B. DeGostin, G.J. Nelson, H. Luebbe, J.A. Schuler, J. Van herle, J.C. Andrews, Y. Liu, P. Pianetta, Y.-C. Karen Chen-Wiegart, J. Wang, and W.K.S. Chiu, "Three-dimensional microstructural mapping of poisoning phases in the Neodymium Nickelate solid oxide fuel cell cathode," *Solid State Ionics*, **237**, 16-21 (2013), DOI: 10.1016/j.ssi.2013.01.020
- W.M. Harris, G.J. Nelson, A.M. Kiss, J.R. Izzo Jr., Y. Liu, M. Liu, S. Wang, Y.S. Chu, and W.K.S. Chiu, "Nondestructive volumetric 3-D chemical mapping of nickel-sulfur compounds at the nanoscale," *Nanoscale*, **4**, 1557-1560 (2012), DOI: 10.1039/c2nr11690a

Notable contributions to co-authorship of papers benefiting from the techniques developed in this dissertation:

- A.P. Cocco, G.J. Nelson, W.M. Harris, A. Nakajo, T.D. Myles, A.M. Kiss, J.J. Lombardo, and W.K.S. Chiu, "Three-dimensional microstructural imaging methods for energy materials," *Phys. Chem. Chem. Phys.*, **15** (39), 16377-16407 (2013), DOI: 10.1039/c3cp52356j
- A.M. Kiss, W.M. Harris, S. Wang, J. Vila-Comamala, A. Deriy, and W.K.S. Chiu, "In-situ observation of nickel oxidation using synchrotron based full-field transmission X-ray microscopy," *Appl. Phys. Letters*, **102** (5), 053902 (2013), DOI: 10.1063/1.4789991
- M.E. Lynch, D. Ding, W.M. Harris, J.J. Lombardo, G.J. Nelson, W.K.S. Chiu, and M. Liu, "Flexible multiphysics simulation of porous electrodes: Conformal to 3D

reconstructed microstructures," *Nano Energy*, **2** (1), 105-115 (2013), DOI: 10.1016/j.nanoen.2012.08.002

- Y.-C. Karen Chen-Wiegart, W.M. Harris, J.J. Lombardo, W.K.S. Chiu, and J. Wang, "Oxidation states study of nickel in solid oxide fuel cell anode using x-ray full-field spectroscopic nano-tomography," *Appl. Phys. Letters*, **101** (25), 253901 (2012), DOI: 10.1063/1.4772784
- G.J. Nelson, W.M. Harris, J.J. Lombardo, J.R. Izzo Jr., W.K.S. Chiu, P. Tanasini, M. Cantoni, J. Van herle, C. Comninellis, J.C. Andrews, Y. Liu, P. Pianetta, and Y.S. Chu, "Comparison of SOFC cathode microstructure quantified using X-ray nanotomography and focused ion beam-scanning electron microscopy," *Electrochem. Commun.*, **13** (6), 586-589 (2011), DOI: 10.1016/j.elecom.2011.03.016
- G.J. Nelson, W.M. Harris, J.R. Izzo Jr., K.N. Grew, W.K.S. Chiu, Y.S. Chu, J. Yi, J.C. Andrews, Y. Liu, and P. Pianetta, "Three-dimensional mapping of nickel oxidation states using full field x-ray absorption near edge structure nanotomography," *Appl. Phys. Letters*, **98** (17), 173109 (2011), DOI: 10.1063/1.3574774

In Preparation:

- W.M. Harris and W.K.S. Chiu, "Predictive Models for Estimating RVE Size for Microstructural Material Characterization"

4.3. Outlook and Recommendations

As synchrotron techniques continue to develop, there will undoubtedly be ample opportunities for application to heterogeneous functional materials. In the past couple years, significant work has been performed by Yijin Liu, Florian Meirer, Joy Andrews, and other team

members at SSRL to advance full-field XANES imaging capabilities.[110-112,228] The team has also developed complementary software to aid in the image acquisition and processing of TXM data.[55] The group has made large gains towards accurate, robust localized XANES measurements in complex, multiphase composite materials. However, limitations still exist in terms of imaging time, as an extensive amount of high-quality data is necessary to guarantee strong signal and accurate phase mapping. Maintaining a high signal to noise ratio throughout the image acquisition remains an instrumental challenge. The management and processing of such large amounts of data, even after collection, also remains a challenge.

Development of new synchrotron equipment and methods is also beneficial for materials characterization. Holotomography, an alternative synchrotron-based 3-D imaging technique based on phase contrast rather than absorption contrast (ie. the real rather than imaginary component of the refractive index) has been applied especially at the European Synchrotron Radiation Facility to obtain flexible imaging capable of operating on a variety of length scales. A high energy beam is used to obtain much larger penetration depth allowing larger samples. Very recently, Villanova *et al*. applied the technique to SOFC electrodes and were able to obtain images of various features covering length scales ranging from single to hundreds of microns.[48,50] This methodology has potential, as it could help to more directly link the length-scales of microstructural transport and overall device response. Even more recent, developing techniques including 3-D fluorescence and ptychography (3-D diffraction-based tomography) could help add to the available tools and complement existing absorption-based tomography methods.[229]

The new National Synchrotron Light Source II will soon replace the NSLS, and will benefit from a higher intensity beam as well as equipment and instrumentation improvements

including new lenses, stage control motors, data collection and management, etc. These will all lead to faster and more comprehensive imaging capabilities. In addition, the continued development of *in-situ* imaging methods will be hugely beneficial as far as directly observing processes in real time, so called 4-D imaging.[10,43,44,230] It will, however, remain a challenge to simultaneously coordinate control of the sample environment, the transient processes of interest affecting the sample, and the time-scale of image acquisition. The implementation of *in-situ* methods relies on consistency of time scales between the phenomenon of interest and the ability to collect data fast enough to properly observe the phenomenon at a given stage of the process.

In device design, it is acknowledged that the understanding and fabrication of new materials should be a two-way street. Advances in fabrication techniques are capable of producing a variety of novel microstructures not previously achievable using classic powder sintering methods. New fabrication techniques include screen printing, plasma spraying, spin-coating, freeze tape-casting, 3-D printing, and so on.[12-14,231-234,234] It is equally interesting, and necessary, to have 3-D imaging capabilities to characterize these structures. While there are new possibilities to create new engineered microstructures, inevitably not all will be durable enough to withstand device operation, and imaging methods will be able to help identify reasons for both success and failure of new materials. This knowledge can then be fed back into the design and fabrication process for the next generation, with an improved foundation of the interconnectedness between the microstructure and device performance.

5. References

[1] Reifsnider, K. L., Chiu, W. K. S., Brinkman, K. S., Du, Y., Nakajo, A., Rabbi, F., Liu, Q., 2013, "Multiphysics design and development of heterogeneous functional materials for renewable energy devices: The heterofoam story," J.Electrochem.Soc., **160**(4), pp. F470-F481.

[2] Chiu, W. K. S., Virkar, A. V., Zhao, F., Reifsnider, K. L., Nelson, G. J., Rabbi, F., Liu, Q., 2012, "HeteroFoaMs: Electrode modeling in nanostructured heterogeneous materials for energy systems," J. Fuel Cell Sci. Tech., **9**(1), pp. 011019-1-011019-6.

[3] Liu, C., Burghaus, U., Besenbacher, F., Wang, Z. L., 2010, "Preparation and characterization of nanomaterials for sustainable energy production," ACS nano, **4**(10), pp. 5517-5526.

[4] Grew, K. N., Chu, Y. S., Yi, J., Peracchio, A. A., Izzo Jr., J. R., Hwu, Y., De Carlo, F., Chiu, W. K. S., 2010, "Nondestructive nanoscale 3D elemental mapping and analysis of a solid oxide fuel cell anode," J.Electrochem.Soc., **157**(6), pp. B783-B792.

[5] Lynch, M. E., Ding, D., Harris, W. M., Lombardo, J. J., Nelson, G. J., Chiu, W. K., Liu, M., 2012, "Flexible multiphysics simulation of porous electrodes: Conformal to 3D reconstructed microstructures," Nano Energy, **2**(1), pp. 105-115.

[6] Song, H. S., Kim, W. H., Hyun, S. H., Moon, J., Kim, J., Lee, H., 2007, "Effect of starting particulate materials on microstructure and cathodic performance of nanoporous LSM–YSZ composite cathodes," J.Power Sources, **167**(2), pp. 258-264.

[7] Cannarozzo, M., Borghi, A. D., Costamagna, P., 2008, "Simulation of mass transport in SOFC composite electrodes," J.Appl.Electrochem., **38**(7), pp. 1011-1018.

[8] Zhao, F., Virkar, A. V., 2005, "Dependence of polarization in anode-supported solid oxide fuel cells on various cell parameters," J.Power Sources, **141**(1), pp. 79-95.

[9] Song, M., Park, S., Alamgir, F. M., Cho, J., Liu, M., 2011, "Nanostructured electrodes for lithium-ion and lithium-air batteries: the latest developments, challenges, and perspectives," Materials Science and Engineering: R: Reports, **72**(11), pp. 203-252.

[10] Chen, W.-C., Song, Y.-F., Wang, C.-C., Liu, Y., Morris, D. T., Pianetta, P. A., Andrews, J. C., Wu, H.-C., Wu, N.-L., 2013, "Study on the synthesis-microstructure-performance relationship of layered Li-excess nickel-manganese oxide as a Li-ion battery cathode prepared by high-temperature calcination," Journal of Materials Chemistry A, **1**(36), pp. 10847-10856.

[11] Kharton, V., Marques, F., 2002, "Mixed ionic–electronic conductors: effects of ceramic microstructure on transport properties," Current Opinion in Solid State and Materials Science, **6**(3), pp. 261-269.

[12] P. Khatri-Chhetri, A. Datar, D. Cormier, Ceramic Transactions, 236 (2012) 129-140.

[13] V. Kumar, G. Manogharan, D.R. Cormier, 20th Annual International Solid Freeform Fabrication Symposium, (2009) 738-748.

[14] Harrysson, O. L. A., Cansizoglu, O., Marcellin-Little, D. J., Cormier, D. R., West II, H. A., 2008, "Direct metal fabrication of titanium implants with tailored materials and mechanical properties using electron beam melting technology," Materials Science and Engineering C, **28**(3), pp. 366-373.

[15] Othman, M. H. D., Wu, Z., Droushiotis, N., Doraswami, U., Kelsall, G., Li, K., 2010, "Single-step fabrication and characterisations of electrolyte/anode dual-layer hollow fibres for micro-tubular solid oxide fuel cells," J.Membr.Sci., **351**(1–2), pp. 196-204.

[16] Droushiotis, N., Doraswami, U., Kanawka, K., Kelsall, G., Li, K., 2009, "Characterization of NiO–yttria stabilised zirconia (YSZ) hollow fibres for use as SOFC anodes," Solid State Ionics, **180**(17), pp. 1091-1099.

[17] C.H.P. Lupis, Chemical Thermodynamics of Materials, Prentice-Hall, New York; 1983, pp. 581.

[18] Mendoza, R., Savin, I., Thornton, K., Voorhees, P. W., 2004, "Topological complexity and the dynamics of coarsening," Nature Materials, **3**(6), pp. 385-388.

[19] L. Ratke, P.W. Voorhees, Growth and coarsening : Ostwald ripening in material processing, Springer, Berlin; New York; 2002.

[20] Voorhees, P. W., 1985, "The theory of Ostwald ripening," Journal of Statistical Physics, **38**(1-2), pp. 231-252.

[21] Nelson, G. J., Grew, K. N., Jr., J. R. I., Lombardo, J. J., Harris, W. M., Faes, A., Hessler-Wyser, A., Herle, J. V., Wang, S., Chu, Y. S., Virkar, A. V., Chiu, W. K. S., 2012, "Three-dimensional microstructural changes in the Ni-YSZ solid oxide fuel cell anode during operation," Acta Mater., **60**(8), pp. 3491-3500.

[22] Cocco, A. P., Nelson, G. J., Harris, W. M., Nakajo, A., Myles, T. D., Kiss, A. M., Lombardo, J. J., Chiu, W. K. S., 2013, "Three-dimensional microstructural imaging methods for energy materials," Physical Chemistry Chemical Physics, **15**(39), pp. 16377-16407.

[23] Möbus, G., Inkson, B. J., 2007, "Nanoscale tomography in materials science," Mater. Today, **10**(12), pp. 18-25.

[24] Koster, A. J., Ziese, U., Verkleij, A. J., Janssen, A. H., De Jong, K. P., 2000, "Three-dimensional transmission electron microscopy: a novel imaging and characterization technique with nanometer scale resolution for materials science," J. Phys. Chem. B, **104**(40), pp. 9368-9370.

[25] Gommes, C. J., De Jong, K., Pirard, J.-P., Blacher, S., 2005, "Assessment of the 3D localization of metallic nanoparticles in Pd/SiO2 cogelled catalysts by electron tomography," Langmuir, **21**(26), pp. 12378-12385.

[26] González, J. C., Hernández, J. C., López-Haro, M., Del Río, E., Delgado, J. J., Hungría, A. B., Trasobares, S., Bernal, S., Midgley, P. A., Calvino, J. J., 2009, "3D characterization of gold nanoparticles supported on heavy metal oxide catalysts by HAADF-STEM electron tomography," Angew. Chem. Int. Ed., **48**(29), pp. 5313-5315.

[27] Chung, S.-Y., Kim, J.-G., Kim, Y.-M., Lee, Y.-B., 2011, "Three-dimensional morphology of iron phosphide phases in a polycrystalline LiFePO4 matrix," Adv. Mater, **23**(11), pp. 1398-1403.

[28] Yoshizawa, N., Tanaike, O., Hatori, H., Yoshikawa, K., Kondo, A., Abe, T., 2006, "TEM and electron tomography studies of carbon nanospheres for lithium secondary batteries," Carbon, **44**(12), pp. 2558-2564.

[29] Shukla, A., Ercius, P., Gautam, A., Cabana, J., Dahmen, U., 2011, "Characterization of Nickel Oxide Nanoplates Using STEM Tomography and In-situ Electron Microscopy," Microsc. Microanal., **17**(Supplement S2), pp. 936-937.

[30] Herzing, A. A., Richter, L. J., Anderson, I. M., 2010, "3D nanoscale characterization of thin-film organic photovoltaic device structures via spectroscopic contrast in the TEM," J. Phys. Chem. C, **114**(41), pp. 17501-17508.

[31] Nelson, G. J., Harris, W. M., Lombardo, J. J., Izzo Jr., J. R., Chiu, W. K. S., Tanasini, P., Cantoni, M.,Van herle, J., Comninellis, C., Andrews, J. C., Liu, Y., Pianetta, P., Chu, Y. S., 2011, "Comparison of SOFC cathode microstructure quantified using X-ray nanotomography and focused ion beam–scanning electron microscopy," Electrochem. Commun., **13**(6), pp. 586-589.

[32] Shikazono, N., Kanno, D., Matsuzaki, K., Teshima, H., Sumino, S., Kasagi, N., 2010, "Numerical assessment of SOFC anode polarization based on three-dimensional model microstructure reconstructed from FIB-SEM images," J.Electrochem.Soc., **157**(5), pp. B665-B672.

[33] Shearing, P. R., Cai, Q., Golbert, J. I., Yufit, V., Adjiman, C. S., Brandon, N. P., 2010, "Microstructural analysis of a solid oxide fuel cell anode using focused ion beam techniques coupled with electrochemical simulation," J.Power Sources, **195**(15), pp. 4804-4810.

[34] Faes, A., Hessler-Wyser, A., Presvytes, D., Vayenas, C. G., Van herle, J., 2009, "Nickel-zirconia anode degradation and triple phase boundary quantification from microstructural analysis," Fuel Cells, **9**(6), pp. 841-851.

[35] Wilson, J. R., Gameiro, M., Mischaikow, K., Kalies, W., Voorhees, P. W., Barnett, S. A., 2009, "Three-dimensional analysis of solid oxide fuel cell Ni-YSZ anode interconnectivity," Microscopy and Microanalysis, **15**(1), pp. 71-77.

[36] Wilson, J. R., Kobsiriphat, W., Mendoza, R., Chen, H. Y., Hiller, J. M., Miller, D. J., Thornton, K., Voorhees, P. W., Adler, S. B., Barnett, S. A., 2006, "Three-dimensional reconstruction of a solid-oxide fuel-cell anode," Nature Mater., **5**(7), pp. 541-544.

[37] Wilson, J. R., Cronin, J. S., Barnett, S. A., 2011, "Linking the microstructure, performance and durability of Ni-yttria-stabilized zirconia solid oxide fuel cell anodes using three-dimensional focused ion beam-scanning electron microscopy imaging," Scr.Mater., **65**(2), pp. 67-72.

[38] Vila-Comamala, J., Pan, Y., Lombardo, J. J., Harris, W. M., Chiu, W. K. S., David, C., Wang, Y., 2012, "Zone-doubled Fresnel Zone Plates for High-Resolution Hard X-ray Full-Field Transmission Microscopy," J. Synchrotron Rad., **19**, pp. 705-709.

[39] Yin, G.-C., Song, Y.-F., Tang, M.-T., Chen, F.-R., Liang, K. S., Duewer, F. W., Feser, M., Yun, W., Shieh, H.-P. D., 2006, "30 nm resolution x-ray imaging at 8 keV using third order diffraction of a zone plate lens objective in a transmission microscope," Appl.Phys.Lett., **89**(22), 221122.

[40] Chen, Y. T., Lo, T. N., Chu, Y. S., Yi, J., Liu, C. J., Wang, J. Y., Wang, C. L., Chiu, C. W., Hua, T. E., Hwu, Y., Shen, Q., Yin, G. C., Liang, K. S., Lin, H. M., Je, J. H., Margaritondo, G., 2008, "Full-field hard x-ray microscopy below 30 nm: A challenging nanofabrication achievement," Nanotechnology, **19**(39), pp. 395302.

[41] Chen, T. Y., Chen, Y. T., Wang, C. L., Kempson, I. M., Lee, W. K., Chu, Y. S., Hwu, Y., Margaritondo, G., 2011, "Full-field microimaging with 8 keV X-rays achieves a spatial resolutions better than 20 nm," Optics Express, **19**(21), pp. 19919-19924.

[42] Chu, Y. S., Yi, J. M., Carlo, F. D., Shen, Q., Lee, W. K., Wu, H. J., Wang, C. L., Wang, J. Y., Liu, C. J., Wang, C. H., Wu, S. R., Chien, C. C., Hwu, Y., Tkachuk, A., Yun, W., Feser, M., Liang, K. S., Yang, C. S., Je, J. H., Margaritondo, G., 2008, "Hard-x-ray microscopy with Fresnel zone plates reaches 40 nm Rayleigh resolution," Appl.Phys.Lett., **92**(10), 103119.

[43] Kiss, A. M., Harris, W. M., Wang, S., Vila-Comamala, J., Deriy, A., Chiu, W. K. S., 2013, "In-situ observation of nickel oxidation using synchrotron based full-field transmission X-ray microscopy," Appl.Phys.Lett., **102**(5), 053902.

[44] Shearing, P. R., Bradley, R. S., Gelb, J., Lee, S. N., Atkinson, A., Withers, P. J., Brandon, N. P., 2011, "Using Synchrotron X-Ray Nano-CT to Characterize SOFC Electrode Microstructures in Three-Dimensions at Operating Temperature," Electrochem. Solid-State Lett., **14**(10), pp. B117-B120.

[45] Bronnikov, A. V., 2002, "Theory of quantitative phase-contrast computed tomography," Journal of the Optical Society of America A: Optics and Image Science, and Vision, **19**(3), pp. 472-480.

[46] Zhao, Y., Brun, E., Coan, P., Huang, Z., Sztrokay, A., Diemoz, P. C., Liebhardt, S., Mittone, A., Gasilov, S., Miao, J., Bravin, A., 2012, "High-resolution, low-dose phase contrast X-ray tomography for 3D diagnosis of human breast cancers," Proc.Natl.Acad.Sci.U.S.A., **109**(45), pp. 18290-18294.

[47] B. Hornberger, PhD Dissertation in Physics. Stony Brook University. (2007).

[48] Villanova, J., Laurencin, J., Cloetens, P., Bleuet, P., Delette, G., Suhonen, H., Usseglio-Viretta, F., 2013, "3D phase mapping of solid oxide fuel cell YSZ/Ni cermet at the nanoscale by holographic X-ray nanotomography," J.Power Sources, **243** pp. 841-849.

[49] Snigirev, A., Snigireva, I., Kohn, V., Kuznetsov, S., Schelokov, I., 1995, "On the possibilities of x-ray phase contrast microimaging by coherent high-energy synchrotron radiation," Rev.Sci.Instrum., **66**(12), pp. 5486-5492.

[50] Villanova, J., Cloetens, P., Suhonen, H., Laurencin, J., Usseglio-Viretta, F., Lay, E., Delette, G., Bleuet, P., Jauffrès, D., Roussel, D., 2014, "Multi-scale 3D imaging of absorbing porous materials for solid oxide fuel cells," J.Mater.Sci., **49**(16), pp. 5626-5634.

[51] Zhou, S., Brahme, A., 2008, "Development of phase-contrast X-ray imaging techniques and potential medical applications," Physica Medica, **24**(3), pp. 129-148.

[52] B.L. Henke, E.M. Gullikson, J.C. Davis, Atomic Data and Nuclear Data Tables, 54 (1993) 181-342.

[53] Wang, J., Chen, Y. K., Yuan, Q., Tkachuk, A., Erdonmez, C., Hornberger, B., Feser, M., 2012, "Automated markerless full field hard x-ray microscopic tomography at sub-50 nm 3-dimension spatial resolution," Appl.Phys.Lett., **100**(14), pp. 143107.

[54] Long, Y., Fessler, J. A., Balter, J. M., 2010, "3D forward and back-projection for X-ray CT using separable footprints," IEEE Trans.Med.Imaging, **29**(11), pp. 1839-1850.

[55] Liu, Y., Zhu, P.P., Chen, B., Wang, J.Y., Yuan, Q.X., Huang, W.X., Shu, H., Li, E.R., Liu, X.S., Zhang, K., Ming, H., Wu, Z.Y., 2007, "A new iterative algorithm to reconstruct the refractive index," Phys.Med.Biol., **52**(12), pp. L5.

[56] B.A. Dowd, G.H. Campbell, R.B. Marr, V.V. Nagarkar, S.V. Tipnis, L. Axe, D.P. Siddons, International Society for Optics and Photonics, (1999) 224-236.

[57] A. Markoe, Analytic Tomography (Encyclopedia of Mathematics and its Applications), Cambridge University Press, New York; 2006, pp. 410.

[58] Pan, X., Sidky, E. Y., Vannier, M., 2009, "Why do commercial CT scanners still employ traditional, filtered back-projection for image reconstruction?" Inverse problems, **25**(12), pp. 123009.

[59] Liu, Y., Meirer, F., Williams, P. A., Wang, J., Andrews, J. C., Pianetta, P., 2012, "TXM-Wizard: A program for advanced data collection and evaluation in full-field transmission X-ray microscopy," Journal of Synchrotron Radiation, **19**(2), pp. 281-287.

[60] R.J. Schalkoff, Digital image processing and computer vision, Wiley New York; 1989.

[61] H. Chuang, PhD Dissertation. Purdue University. (2011)

[62] R. Jain, R. Kasturi, B.G. Schunck, Machine vision, McGraw-Hill New York; 1995.

[63] P. Jørgensen, PhD Dissertation. Technical University of Denmark. (2010)

[64] Jørgensen, P. S., Hansen, K. V., Larsen, R., Bowen, J. R., 2010, "A framework for automatic segmentation in three dimensions of microstructural tomography data," Ultramicroscopy, **110**(3), pp. 216-228.

[65] Bleau, A., Leon, L. J., 2000, "Watershed-Based Segmentation and Region Merging," Comput.Vision Image Understanding, **77**(3), pp. 317-370.

[66] Lombardo, J. J., Ristau, R., Harris, W. M., Chiu, W. K. S., 2012, "Focused Ion Beam Preparation of Samples for X-ray Nanotomography," J. Synchrotron Radiat., **19** pp. 789-796.

[67] Grew, K. N., Peracchio, A. A., Joshi, A. S., Izzo Jr., J. R., Chiu, W. K. S., 2010, "Characterization and analysis methods for the examination of the heterogeneous solid oxide fuel cell electrode microstructure. Part 1: Volumetric measurements of the heterogeneous structure," J.Power Sources, **195**(24), pp. 7930-7942.

[68] Grew, K. N., Peracchio, A. A., Chiu, W. K. S., 2010, "Characterization and analysis methods for the examination of the heterogeneous solid oxide fuel cell electrode microstructure: Part 2. Quantitative measurement of the microstructure and contributions to transport losses," J.Power Sources, **195**(24), pp. 7943-7958.

[69] Chen-Wiegart, Y. K., DeMike, R., Erdonmez, C., Thornton, K., Barnett, S. A., Wang, J., 2014, "Tortuosity characterization of 3D microstructure at nano-scale for energy storage and conversion materials," J.Power Sources, **249** pp. 349-356.

[70] Laurencin, J., Quey, R., Delette, G., Suhonen, H., Cloetens, P., Bleuet, P., 2012, "Characterisation of Solid Oxide Fuel Cell Ni–8YSZ substrate by synchrotron X-ray nano-tomography: from 3D reconstruction to microstructure quantification," J.Power Sources, **198**(0), pp. 182-189.

[71] Joos, J., Carraro, T., Weber, A., Ivers-Tiffée, E., 2011, "Reconstruction of porous electrodes by FIB/SEM for detailed microstructure modeling," J.Power Sources, **196**(17), pp. 7302-7307.

[72] Hubbell, J. H., Seltzer, S. M., 1996, "Tables of x-ray mass attenuation coefficients and mass energy-absorption coefficients," National Institute of Standards and Technology.

[73] Cronin, J. S., Chen-Wiegart, Y.-C. K., Wang, J., Barnett, S. A., 2013, "Three-dimensional reconstruction and analysis of an entire solid oxide fuel cell by full-field transmission X-ray microscopy," J.Power Sources, **233** pp. 174-179.

[74] Guan, Y., Li, W., Gong, Y., Liu, G., Zhang, X., Chen, J., Gelb, J., Yun, W., Xiong, Y., Tian, Y., Wang, H., 2011, "Analysis of the three-dimensional microstructure of a solid-oxide fuel cell anode using nano X-ray tomography," J.Power Sources, **196**(4), pp. 1915-1919.

[75] W.M. Harris, G.J. Nelson, J.J. Lombardo, A.P. Cocco, J.R. Izzo Jr., W.K.S. Chiu, P. Tanasini, J. Van Herle, C. Comninellis, J.C. Andrews, Y. Liu, P. Pianetta, Y.S. Chu, ASME 2011 International Mechanical Engineering Congress and Exposition, IMECE 2011, 4 (2011) 581-584.

[76] Waldbillig, D., Wood, A., Ivey, D. G., 2005, "Electrochemical and microstructural characterization of the redox tolerance of solid oxide fuel cell anodes," J.Power Sources, **145** pp. 206-215.

[77] Waldbillig, D., Wood, A., Ivey, D. G., 2005, "Thermal analysis of the cyclic reduction and oxidation behaviour of SOFC anodes," Solid State Ionics, **176**(9-10), pp. 847-859.

[78] Faes, A., Nakajo, A., Hessler-Wyser, A., Dubois, D., Brisse, A., Modena, S., Van herle, J., 2009, "RedOx study of anode-supported solid oxide fuel cell," J.Power Sources, **193**(1), pp. 55-64.

[79] Laurencin, J., Delette, G., Lefebvre-Joud, F., Dupeux, M., 2008, "A numerical tool to estimate SOFC mechanical degradation: Case of the planar cell configuration," Journal of the European Ceramic Society, **28**(9), pp. 1857-1869.

[80] Laurencin, J., Delette, G., Morel, B., Lefebvre-Joud, F., Dupeux, M., 2009, "Solid Oxide Fuel Cells damage mechanisms due to Ni-YSZ re-oxidation: Case of the Anode Supported Cell," J.Power Sources, **192**(2), pp. 344-352.

[81] Sarantaridis, D., Atkinson, A., 2007, "Redox cycling of Ni-based solid oxide fuel cell anodes: A review," Fuel Cells, **7**(3), pp. 246-258.

[82] Meher, S. K., Justin, P., Rao, G. R., 2010, "Pine-cone morphology and pseudocapacitive behavior of nanoporous nickel oxide," Electrochim.Acta, **55**(28), pp. 8388-8396.

[83] Wang, Q., Gao, R., Li, J., 2007, "Porous, self-supported Ni3S2 Ni nanoarchitectured electrode operating through efficient lithium-driven conversion reactions," Appl.Phys.Lett., **90**(14), 143107.

[84] Wang, J., Chou, S., Chew, S., Sun, J., Forsyth, M., MacFarlane, D. R., Liu, H., 2008, "Nickel sulfide cathode in combination with an ionic liquid-based electrolyte for rechargeable lithium batteries," Solid State Ionics, **179**(40), pp. 2379-2382.

[85] Wang, J., Liu, M., 2008, "Surface regeneration of sulfur-poisoned Ni surfaces under SOFC operation conditions predicted by first-principles-based thermodynamic calculations," J.Power Sources, **176**(1), pp. 23-30.

[86] Bae, K. W., Kim, H. S., Cho, G. B., Kim, K. W., Cho, K. K., Lee, J. H., Nam, T. H., 2009, "Ni sulfide/Ti50Ni50 electrode with the superelasticity," J.Power Sources, **189**(1), pp. 378-384.

[87] Kim, J., Cho, G., Kim, K., Ahn, J., Wang, G., Ahn, H., 2011, "The addition of iron to Ni3S2 electrode for sodium secondary battery," Current Applied Physics, **11**(1, Supplement 1), pp. S215-S218.

[88] Kim, J., Ahn, H., Ryu, H., Kim, D., Cho, G., Kim, K., Nam, T., Ahn, J. H., 2008, "The discharge properties of Na/Ni3S2 cell at ambient temperature," J.Power Sources, **178**(2), pp. 852-856.

[89] Sun, H., Qin, D., Huang, S., Guo, X., Li, D., Luo, Y., Meng, Q., 2011, "Dye-sensitized solar cells with NiS counter electrodes electrodeposited by a potential reversal technique," Energy and Environmental Science, **4**(8), pp. 2630-2637.

[90] Braun, A., Janousch, M., Sfeir, J., Kiviaho, J., Noponen, M., Huggins, F. E., Smith, M. J., Steinberger-Wilckens, R., Holtappels, P., Graule, T., 2008, "Molecular speciation of sulfur in solid oxide fuel cell anodes with X-ray absorption spectroscopy," J.Power Sources, **183**(2), pp. 564-570.

[91] Allen, A. J., Ilavsky, J., Braun, A., 2009, "Multi-scale microstructure characterization of solid oxide fuel cell assemblies with ultra small-angle X-ray scattering," Advanced Engineering Materials, **11**(6), pp. 495-501.

[92] Cheng, Z., Wang, J.-H., Choi, Y., Yang, L., Lin, M. C., Liu, M., 2011, "From Ni-YSZ to sulfur-tolerant anode materials for SOFCs: Electrochemical behavior, in situ characterization, modeling, and future perspectives," Energy and Environmental Science, **4**(11), pp. 4380-4409.

[93] Haga, K., Adachi, S., Shiratori, Y., Itoh, K., Sasaki, K., 2008, "Poisoning of SOFC anodes by various fuel impurities," Solid State Ionics, **179**(27-32), pp. 1427-1431.

[94] Cayan, F. N., Zhi, M., Pakalapati, S. R., Celik, I., Wu, N., Gemmen, R., 2008, "Effects of coal syngas impurities on anodes of solid oxide fuel cells," J.Power Sources, **185**(2), pp. 595-602.

[95] Sato, K., Fujimoto, K., 2007, "Development of new nickel based catalyst for tar reforming with superior resistance to sulfur poisoning and coking in biomass gasification," Catalysis Communications, **8**(11), pp. 1697-1701.

[96] Li, L., Howard, C., King, D. L., Gerber, M., Dagle, R., Stevens, D., 2010, "Regeneration of sulfur deactivated Ni-based biomass syngas cleaning catalysts," Industrial and Engineering Chemistry Research, **49**(20), pp. 10144-10148.

[97] Matsumoto, S., Ikeda, Y., Suzuki, H., Ogai, M., Miyoshi, N., 2000, "NO(x) storage-reduction catalyst for automotive exhaust with improved tolerance against sulfur poisoning," Applied Catalysis B: Environmental, **25**(2-3), pp. 115-124.

[98] Di Carlo, G., Melaet, G., Kruse, N., Liotta, L. F., Pantaleo, G., Venezia, A. M., 2010, "Combined sulfating and non-sulfating support to prevent water and sulfur poisoning of Pd catalysts for methane combustion," Chemical Communications, **46**(34), pp. 6317-6319.

[99] Corro, G., Cano, C., Fierro, J. L. G., 2010, "A study of Pt–Pd/γ-Al2O3 catalysts for methane oxidation resistant to deactivation by sulfur poisoning," Journal of Molecular Catalysis A: Chemical, **315**(1), pp. 35-42.

[100] Chen, Y., Xie, C., Li, Y., Song, C., Bolin, T. B., 2010, "Sulfur poisoning mechanism of steam reforming catalysts: An X-ray absorption near edge structure (XANES) spectroscopic study," Physical Chemistry Chemical Physics, **12**(21), pp. 5707-5711.

[101] Xie, C., Chen, Y., Li, Y., Wang, X., Song, C., 2010, "Sulfur poisoning of CeO2–Al2O3-supported mono- and bi-metallic Ni and Rh catalysts in steam reforming of liquid hydrocarbons at low and high temperatures," Applied Catalysis A: General, **390**(1-2), pp. 210-218.

[102] Cheng, Z., Zha, S., Liu, M., 2006, "Stability of materials as candidates for sulfur-resistant anodes of solid oxide fuel cells," J.Electrochem.Soc., **153**(7), pp. A1302-A1309.

[103] Gong, M., Liu, X., Trembly, J., Johnson, C., 2007, "Sulfur-tolerant anode materials for solid oxide fuel cell application," J.Power Sources, **168**(2), pp. 289-298.

[104] Yang, L., Choi, Y., Qin, W., Chen, H., Blinn, K., Liu, M., Liu, P., Bai, J., Tyson, T. A., Liu, M., 2011, "Promotion of water-mediated carbon removal by nanostructured barium oxide/nickel interfaces in solid oxide fuel cells," Nature Communications, **2**(1), 357.

[105] Huang, Y.-H., Dass, R. I., King, Z.-L., Goodenough, J. B., 2006, "Double perovskites as anode materials for solid-oxide fuel cells," Science, **312**(5771), pp. 254-257.

[106] G.J. Nelson, W.M. Harris, J.R. Izzo Jr., K.N. Grew, W.K.S. Chiu, Y.S. Chu, J. Yi, J.C. Andrews, Y. Liu, P. Pianetta, ECS Transactions, 35 (2011) 1315-1321.

[107] W.M. Harris, G.J. Nelson, A.M. Kiss, J.R. Izzo, Y. Liu, M. Liu, S. Wang, Y.S. Chu, W.K.S. Chiu, Nanoscale, **4** (2012) 1557-1560.

[108] Huggins, F. E., Shah, N., Huffman, G. P., Robertson, J. D., 2000, "XAFS spectroscopic characterization of elements in combustion ash and fine particulate matter," Fuel Process Technol, **65**, pp. 203-218.

[109] Niemann, W., Clausen, B. S., Topsøe, H., 1990, "X-Ray absorption studies of the Ni environment in Ni-Mo-S," Catalysis Letters, **4**(4-6), pp. 355-363.

[110] Meirer, F., Cabana, J., Liu, Y., Mehta, A., Andrews, J. C., Pianetta, P., 2011, "Three-dimensional imaging of chemical phase transformations at the nanoscale with full-field transmission X-ray microscopy," Journal of Synchrotron Radiation, **18**(5), pp. 773-781.

[111] Liu, Y., Meirer, F., Wang, J., Requena, G., Williams, P., Nelson, J., Mehta, A., Andrews, J. C., Pianetta, P., 2012, "3D elemental sensitive imaging using transmission X-ray microscopy," Analytical and Bioanalytical Chemistry, **404**(5), pp. 1297-1301.

[112] Kao, T. L., Shi, C. Y., Wang, J., Mao, W. L., Liu, Y., Yang, W., 2013, "Nanoscale elemental sensitivity study of Nd2Fe14B using absorption correlation tomography," Microsc.Res.Tech., **76**(11), pp. 1112-1117.

[113] Chen-Wiegart, Y.-C. Karen, Harris, W. M., Lombardo, J. J., Chiu, W. K. S., Wang, J., 2012, "Oxidation states study of nickel in solid oxide fuel cell anode using x-ray full-field spectroscopic nano-tomography," Appl.Phys.Lett., **101**(25), 253901.

[114] Harris, W. M., Lombardo, J. J., DeGostin, M. B., Nelson, G. J., Luebbe, H., Schuler, J. A., Van herle, J., Andrews, J. C., Liu, Y., Pianetta, P., Chen, Y.-C. Karen, Wang, J., Chiu, W. K. S., 2013, "Three-dimensional microstructural mapping of poisoning phases in the Neodymium Nickelate solid oxide fuel cell cathode," Solid State Ionics, **237** pp. 16-21.

[115] Omosun, A., Bauen, A., Brandon, N., Adjiman, C., Hart, D., 2004, "Modelling system efficiencies and costs of two biomass-fuelled SOFC systems," J.Power Sources, **131**(1), pp. 96-106.

[116] Kee, R. J., Zhu, H., Sukeshini, A. M., Jackson, G. S., 2008, "Solid oxide fuel cells: operating principles, current challenges, and the role of syngas," Combustion Sci.Technol., **180**(6), pp. 1207-1244.

[117] S. Singhal, High-temperature Solid Oxide Fuel Cells: Fundamentals, Design and Applications: Fundamentals, Design and Applications, Elsevier; 2003.

[118] Atkinson, A., Barnett, S., Gorte, R. J., Irvine, J., McEvoy, A. J., Mogensen, M., Singhal, S. C., Vohs, J., 2004, "Advanced anodes for high-temperature fuel cells," Nature Materials, **3**(1), pp. 17-27.

[119] Wachsman, E. D., Lee, K. T., 2011, "Lowering the temperature of solid oxide fuel cells," Science, **334**(6058), pp. 935-939.

[120] Huang, J., Xie, F., Wang, C., Mao, Z., 2012, "Development of solid oxide fuel cell materials for intermediate-to-low temperature operation," Int. J. Hydrogen Energy, **37**(1), pp. 877-883.

[121] Cowin, P. I., Petit, C. T., Lan, R., Irvine, J. T., Tao, S., 2011, "Recent progress in the development of anode materials for solid oxide fuel cells," Advanced Energy Materials, **1**(3), pp. 314-332.

[122] Menzler, N. H., Tietz, F., Uhlenbruck, S., Buchkremer, H. P., Stöver, D., 2010, "Materials and manufacturing technologies for solid oxide fuel cells," J.Mater.Sci., **45**(12), pp. 3109-3135.

[123] Lawlor, V., Griesser, S., Buchinger, G., Olabi, A. G., Cordiner, S., Meissner, D., 2009, "Review of the micro-tubular solid oxide fuel cell: Part I. Stack design issues and research activities," J.Power Sources, **193**(2), pp. 387-399.

[124] Kendall, K., 2010, "Progress in Microtubular Solid Oxide Fuel Cells," International Journal of Applied Ceramic Technology, **7**(1), pp. 1-9.

[125] Cui, D., Cheng, M., 2009, "Numerical analysis of thermal and electrochemical phenomena for anode supported microtubular SOFC," AIChE J., **55**(3), pp. 771-782.

[126] K. Kendall, C.M. Dikwal, ECS Transactions, 25 (2009) 899-906.

[127] Yamaguchi, T., Shimizu, S., Suzuki, T., Fujishiro, Y., Awano, M., 2008, "Demonstration of the rapid start-up operation of cathode-supported SOFCs using a microtubular LSM support," J.Electrochem.Soc., **155**(11), pp. B1141-B1144.

[128] Liu, Y., Hashimoto, S.-I., Nishino, H., Takei, K., Mori, M., Suzuki, T., Funahashi, Y., 2007, "Fabrication and characterization of micro-tubular cathode-supported SOFC for intermediate temperature operation," J.Power Sources, **174**(1), pp. 95-102.

[129] Sayers, R., Liu, J., Rustumji, B., Skinner, S. J., 2008, "Novel K2NiF4-Type Materials for Solid Oxide Fuel Cells: Compatibility with Electrolytes in the Intermediate Temperature Range," Fuel Cells, **8**(5), pp. 338-343.

[130] Yamaguchi, T., Shimizu, S., Suzuki, T., Fujishiro, Y., Awano, M., 2008, "Fabrication and characterization of high performance cathode supported small-scale SOFC for intermediate temperature operation," Electrochemistry Communications, **10**(9), pp. 1381-1383.

[131] Yamaguchi, T., Shimizu, S., Suzuki, T., Fujishiro, Y., Awano, M., 2008, "Evaluation of micro LSM-supported GDC/ScSZ bilayer electrolyte with LSM-GDC activation layer for intermediate temperature-SOFCs," J.Electrochem.Soc., **155**(4), pp. B423-B426.

[132] Suzuki, T., Yamaguchi, T., Fujishiro, Y., Awano, M., 2006, "Fabrication and characterization of micro tubular SOFCs for operation in the intermediate temperature," J.Power Sources, **160**(1), pp. 73-77.

[133] Zhao, C., Liu, R., Wang, S., Wang, Z., Qian, J., Wen, T., 2009, "Fabrication and characterization of a cathode-supported tubular solid oxide fuel cell," J.Power Sources, **192**(2), pp. 552-555.

[134] Liu, Y., Hashimoto, S.-I., Takei, K., Mori, M., Funahashi, Y., 2008, "Development and characterization of cathode-supported SOFCs by single-step cofiring fabrication for intermediate temperature operation," Journal of Fuel Cell Science and Technology, **5**(3), 031209.

[135] Boehm, E., Bassat, J.-M., Dordor, P., Mauvy, F., Grenier, J.-C., Stevens, P., 2005, "Oxygen diffusion and transport properties in non-stoichiometric Ln2 − xNiO4 + δ oxides," Solid State Ionics, **176**(37–38), pp. 2717-2725.

[136] Lalanne, C., Prosperi, G., Bassat, J.-M., Mauvy, F., Fourcade, S., Stevens, P., Zahid, M., Diethelm, S., Van herle, J., Grenier, J.-C., 2008, "Neodymium-deficient nickelate oxide Nd1.95NiO4+δ as cathode material for anode-supported intermediate temperature solid oxide fuel cells," J.Power Sources, **185**(2), pp. 1218-1224.

[137] Mauvy, F., Bassat, J.-M., Boehm, E., Manaud, J.-P., Dordor, P., Grenier, J.-C., 2003, "Oxygen electrode reaction on Nd2NiO4+δ cathode materials: impedance spectroscopy study," Solid State Ionics, **158**(1–2), pp. 17-28.

[138] Mauvy, F., Lalanne, C., Bassat, J.-M., Grenier, J.-C., Zhao, H., Huo, L., Stevens, P., 2006, "Electrode properties of Ln 2NiO 4+δ (Ln=La, Nd, Pr): AC impedance and DC polarization studies," J.Electrochem.Soc., **153**(8), pp. A1547-A1553.

[139] Bassat, J.-M., Odier, P., Villesuzanne, A., Marin, C., Pouchard, M., 2004, "Anisotropic ionic transport properties in La2NiO4+δ single crystals," Solid State Ionics, **167**(3–4), pp. 341-347.

[140] Mauvy, F., Lalanne, C., Fourcade, S., Bassat, J. M., Grenier, J. C., 2007, "Impedance spectroscopy study of Nd2NiO4+δ, LSM and platinum electrodes by micro-contact technique," Journal of the European Ceramic Society, **27**(13–15), pp. 3731-3734.

[141] Kharton, V. V., Viskup, A. P., Kovalevsky, A. V., Naumovich, E. N., Marques, F. M. B., 2001, "Ionic transport in oxygen-hyperstoichiometric phases with K2NiF4-type structure," Solid State Ionics, **143**(3–4), pp. 337-353.

[142] Luebbe, H., Van herle, J., Hofmann, H., Bowen, P., Aschauer, U., Schuler, A., Snijkers, F., Schindler, H.-J., Vogt, U., Lalanne, C., 2009, "Cathode-supported micro-tubular SOFCs based on Nd1.95NiO4 + δ: Fabrication and characterisation of dip-coated electrolyte layers," Solid State Ionics, **180**(11-13), pp. 805-811.

[143] H. Luebbe, PhD Dissertation. Ecole Polytechnique Fédérale de Lausanne. (2011).

[144] Andreas Schuler, J., Lübbe, H., Hessler-Wyser, A., Van herle, J., 2012, "Nd-nickelate solid oxide fuel cell cathode sensitivity to Cr and Si contamination," J.Power Sources, **213**(0), pp. 223-228.

[145] Wold, A., Post, B., Banks, E., 1957, "Rare Earth Nickel Oxides," J.Am.Chem.Soc., **79**(18), pp. 4911-4913.

[146] An, T., Baikie, T., Wei, F., Li, H., Brink, F., Wei, J., Ngoh, S. L., White, T. J., Kloc, C., 2011, "Single crystal growth of apatite-type Al-doped neodymium silicates by the floating zone method," J.Cryst.Growth, **333**(1), pp. 70-73.

[147] Harris, W. M., Lombardo, J. J., Nelson, G. J., Lai, B., Wang, S., Vila-Comamala, J., Liu, M., Liu, M., Chiu, W. K. S., 2014, "Three-dimensional microstructural imaging of sulfur poisoning-induced degradation in a Ni-YSZ anode of solid oxide fuel cells," Scientific Reports, **4** pp. 5246.

[148] Cheng, Z., Liu, M., 2007, "Characterization of sulfur poisoning of Ni–YSZ anodes for solid oxide fuel cells using in situ Raman microspectroscopy," Solid State Ionics, **178**(13-14), pp. 925-935.

[149] Lakshminarayanan, N., Ozkan, U. S., 2011, "Effect of H2O on sulfur poisoning and catalytic activity of Ni–YSZ catalysts," Applied Catalysis A: General, **393**(1-2), pp. 138-145.

[150] Xiao, G., Liu, Q., Dong, X., Huang, K., Chen, F., 2010, "Sr 2Fe 4/3Mo 2/3O 6 as anodes for solid oxide fuel cells," J.Power Sources, **195**(24), pp. 8071-8074.

[151] Zhang, L., Jiang, S. P., He, H. Q., Chen, X., Ma, J., Song, X. C., 2010, "A comparative study of H2S poisoning on electrode behavior of Ni/YSZ and Ni/GDC anodes of solid oxide fuel cells," Int. J. Hydrogen Energy, **35**(22), pp. 12359-12368.

[152] Hagen, A., Rasmussen, J. F. B., Thydén, K., 2011, "Durability of solid oxide fuel cells using sulfur containing fuels," J.Power Sources, **196**(17), pp. 7271-7276.

[153] Kishimoto, H., Horita, T., Yamaji, K., Brito, M. E., Xiong, Y.-P., Yokokawa, H., 2010, "Sulfur poisoning on SOFC Ni anodes: Thermodynamic analyses within local equilibrium anode reaction model," J.Electrochem.Soc., **157**(6), pp. B802-B813.

[154] Lussier, A., Sofie, S., Dvorak, J., Idzerda, Y. U., 2008, "Mechanism for SOFC anode degradation from hydrogen sulfide exposure," Int. J. Hydrogen Energy, **33**(14), pp. 3945-3951.

[155] Zha, S., Cheng, Z., Liu, M., 2007, "Sulfur poisoning and regeneration of ni-based anodes in solid oxide fuel cells," J.Electrochem.Soc., **154**(2), pp. B201-B206.

[156] Sasaki, K., Susuki, K., Iyoshi, A., Uchimura, M., Imamura, N., Kusaba, H., Teraoka, Y., Fuchino, H., Tsujimoto, K., Uchida, Y., Jingo, N., 2006, "H2S poisoning of solid oxide fuel cells," J.Electrochem.Soc., **153**(11), pp. A2023-A2029.

[157] Hagen, A., 2013, "Sulfur poisoning of the water gas shift reaction on anode supported solid oxide fuel cells," J.Electrochem.Soc., **160**(2), pp. F111-F118.

[158] J.B. Hansen, J. Rostrup-Nielsen, Sulfur Poisoning on Ni catalyst and anodes, John Wiley & Sons, Ltd., 2009.

[159] Cayan, F. N., Pakalapati, S. R., Celik, I., Xu, C., Zondlo, J., 2012, "A degradation model for solid oxide fuel cell anodes due to impurities in coal syngas: Part i theory and validation," Fuel Cells, **12**(3), pp. 464-473.

[160] Wang, J.-H., Liu, M., 2007, "Computational study of sulfur-nickel interactions: A new S-Ni phase diagram," Electrochemistry Communications, **9**(9), pp. 2212-2217.

[161] Bastow, B. D., Wood, G. C., 1975, "Multilayer scale formation during the sulfidation of nickel," Oxidation Metals, **9**(6), pp. 473-496.

[162] Adams, F., Janssens, K., Snigirev, A., 1998, "Microscopic X-ray fluorescence analysis and related methods with laboratory and synchrotron radiation sources," J.Anal.At.Spectrom., **13**(5), pp. 319-331.

[163] Dravnieks, A., 1955, "Kinetics of Nickel-Sulfur and Steel-Sulfur Reactions," J. Electrochem. Soc., **102**(8), pp. 435-439.

[164] Stoklosa, A., Stringer, J., 1977, "Studies of the kinetics of nickel sulfidation in H2S-H2 mixtures in the temperature range 450-600°C," Oxidation Metals, **11**(5), pp. 263-276.

[165] Mrowec, S., 1995, "The problem of sulfur in high-temperature corrosion," Oxidation Metals, **44**(1-2), pp. 177-209.

[166] Harris, W., Brinkman, K., Lin, Y., Su, D., Cocco, A., Nakajo, A., DeGostin, M., Chen-Wiegart, Y. K., Wang, J., Chen, F. F., 2014, "Characterization of 3D Interconnected Microstructural Network in Mixed Ionic and Electronic Conducting Ceramic Composites," Nanoscale, **6**, pp. 4480-4485.

[167] J. Larminie, A. Dicks, Fuel Cell Systems Explained, 2nd ed., Wiley, England; 2003.

[168] Shao, Y., Ding, F., Xiao, J., Zhang, J., Xu, W., Park, S., Zhang, J.-G., Wang, Y., Liu, J., 2013, "Making Li-air batteries rechargeable: Material challenges," Advanced Functional Materials, **23**(8), pp. 987-1004.

[169] Dyer, P. N., Richards, R. E., Russek, S. L., Taylor, D. M., 2000, "Ion transport membrane technology for oxygen separation and syngas production," Solid State Ionics, **134**(1-2), pp. 21-33.

[170] Takamura, H., Ogawa, M., Suehiro, K., Takahashi, H., Okada, M., 2008, "Fabrication and characteristics of planar-type methane reformer using ceria-based oxygen permeable membrane," Solid State Ionics, **179**(27-32), pp. 1354-1359.

[171] Brinkman, K., Iijima, T., Takamura, H., 2010, "The oxygen permeation characteristics of Bi1 - xSrxFeO3 mixed ionic and electronic conducting ceramics," Solid State Ionics, **181**(1-2), pp. 53-58.

[172] Bouwmeester, H. J. M., 2003, "Dense ceramic membranes for methane conversion," Catalysis Today, **82**(1-4), pp. 141-150.

[173] Kagomiya, I., Iijima, T., Kakuta, H., Takamura, H., 2005, "Oxygen permeable Ce0.8Gd0.2O1.9-CoFe 2O4 thin films prepared on porous Ce0.8Gd 0.2O1.9 substrates," Electrochemical and Solid-State Letters, **8**(1), pp. A70-A73.

[174] Luo, H., Jiang, H., Klande, T., Cao, Z., Liang, F., Wang, H., Caro, J., 2012, "Novel cobalt-free, noble metal-free oxygen-permeable 40Pr 0.6Sr 0.4FeO 3-d-60Ce 0.9Pr 0.1O 2-d dual-phase membrane," Chemistry of Materials, **24**(11), pp. 2148-2154.

[175] Sunarso, J., Baumann, S., Serra, J. M., Meulenberg, W. A., Liu, S., Lin, Y. S., Diniz da Costa, J. C., 2008, "Mixed ionic-electronic conducting (MIEC) ceramic-based membranes for oxygen separation," J.Membr.Sci., **320**(1-2), pp. 13-41.

[176] Krishnan, A., Lu, X. G., Pal, U. B., 2005, "Solid oxide membrane process for magnesium production directly from magnesium oxide," Metall Mat Trans B Process Metall Mat Process Sci, **36**(4), pp. 463-473.

[177] Pal, U. B., Woolley, D. E., Kenney, G. B., 2001, "Emerging SOM technology for the green synthesis of metals from oxides," JOM, **53**(10), pp. 32-35.

[178] D.S. Poa, L. Burris, R.K. Steunenberg, US. Patent 4,995,948 (1991).

[179] Stoots, C. M., O'Brien, J. E., Condie, K. G., Hartvigsen, J. J., 2010, "High-temperature electrolysis for large-scale hydrogen production from nuclear energy - Experimental investigations," Int J Hydrogen Energy, **35**(10), pp. 4861-4870.

[180] Kim, I.-D., Rothschild, A., Tuller, H. L., 2013, "Advances and new directions in gas-sensing devices," Acta Materialia, **61**(3), pp. 974-1000.

[181] Inaba, H., Tagawa, H., 1996, "Ceria-based solid electrolytes," Solid State Ionics, **83**(1–2), pp. 1-16.

[182] H. Takamura, M. Kawai, K. Okumura, A. Kamegawa, M. Okada, Materials Research Society Symposium - Proceedings, 756 (2003) 121-126.

[183] Guo, J.-L., Chiou, Y.-D., Liang, W.-I., Liu, H.-J., Chen, Y.-J., Kuo, W.-C., Tsai, C.-Y., Tsai, K.-A., Kuo, H.-H., Hsieh, W.-F., Juang, J.-Y., Hsu, Y.-J., Lin, H.-J., Chen, C.-T., Liao, X.-P., Shi, B., Chu, Y.-H., 2013, "Complex oxide-noble metal conjugated nanoparticles," Adv Mater, **25**(14), pp. 2040-2044.

[184] Thursfield, A., Metcalfe, I. S., 2004, "The use of dense mixed ionic and electronic conducting membranes for chemical production," Journal of Materials Chemistry, **14**(16), pp. 2475-2485.

[185] Takamura, H., Koshino, Y., Kamegawa, A., Okada, M., 2006, "Electrode and oxygen permeation properties of (Ce, Sm)O2-MFe2O4 composite thin films (M = Co and Mn)," Solid State Ionics, **177**(19-25 SPEC. ISS.), pp. 2185-2189.

[186] Kagomiya, I., Iijima, T., Takamura, H., 2006, "Oxygen permeability of nanocrystalline Ce0.8Gd0.2O1.9-CoFe2O4 mixed-conductive films," J.Membr.Sci., **286**(1-2), pp. 180-184.

[187] Crabtree, G. W., Sarrao, J. L., 2012, "Opportunities for mesoscale science," MRS Bull, **37**(11), pp. 1079-1088.

[188] Kharton, V. V., Kovalevsky, A. V., Viskup, A. P., Figueiredo, F. M., Yaremchenko, A. A., Naumovich, E. N., Marques, F. M. B., 2001, "Oxygen permeability and Faradaic efficiency of Ce0.8Gd0.2O2–δ–La0.7Sr0.3MnO3–δ composites," Journal of the European Ceramic Society, **21**(10–11), pp. 1763-1767.

[189] Wagner, C., 1975, "Equations for transport in solid oxides and sulfides of transition metals," Progress in Solid State Chemistry, **10**, pp. 3-16.

[190] P.J. Gellings, H. Bouwmeester, Handbook of Solid State Electrochemistry, CRC press; 1997.

[191] Abbas, Y. M., Mansour, S. A., Ibrahim, M. H., Ali, S. E., 2011, "Microstructure characterization and cation distribution of nanocrystalline cobalt ferrite," J Magn Magn Mater, **323**(22), pp. 2748-2756.

[192] Kanit, T., Forest, S., Galliet, I., Mounoury, V., Jeulin, D., 2003, "Determination of the size of the representative volume element for random composites: statistical and numerical approach," Int.J.Solids Structures, **40**(13–14), pp. 3647-3679.

[193] Gitman, I. M., Askes, H., Sluys, L. J., 2007, "Representative volume: Existence and size determination," Eng.Fract.Mech., **74**(16), pp. 2518-2534.

[194] Evesque, P., 2000, "Fluctuations, correlation and representative elementary Volume (REV) in granular materials," Poudres and Grains, **11**, pp 6-17.

[195] Ostoja-Starzewski, M., 2006, "Material spatial randomness: From statistical to representative volume element," Prob.Eng.Mech., **21**(2), pp. 112-132.

[196] Stroeven, M., Askes, H., Sluys, L., 2004, "Numerical determination of representative volumes for granular materials," Comput.Methods Appl.Mech.Eng., **193**(30), pp. 3221-3238.

[197] Trias, D., Costa, J., Turon, A., Hurtado, J., 2006, "Determination of the critical size of a statistical representative volume element (SRVE) for carbon reinforced polymers," Acta materialia, **54**(13), pp. 3471-3484.

[198] Vinogradov, O., 2001, "On a representative volume in the micromechanics of particulate composites," Mechanics of composite materials, **37**(3), pp. 245-250.

[199] Cronin, J. S., Wilson, J. R., Barnett, S. A., 2011, "Impact of pore microstructure evolution on polarization resistance of Ni-Yttria-stabilized zirconia fuel cell anodes," J.Power Sources, **196**(5), pp. 2640-2643.

[200] Ender, M., Joos, J., Carraro, T., Ivers-Tiffée, E., 2012, "Quantitative Characterization of LiFePO4 Cathodes Reconstructed by FIB/SEM Tomography," J.Electrochem.Soc., **159**(7), pp. A972-A980.

[201] Shearing, P., Bradley, R., Gelb, J., Tariq, F., Withers, P., Brandon, N., 2012, "Exploring microstructural changes associated with oxidation in Ni–YSZ SOFC electrodes using high resolution X-ray computed tomography," Solid State Ionics, **216** pp. 69-72.

[202] Shearing, P. R., Howard, L. E., Jørgensen, P. S., Brandon, N. P., Harris, S. J., 2010, "Characterization of the 3-dimensional microstructure of a graphite negative electrode from a Li-ion battery," Electrochem. Commun., **12**(3), pp. 374-377.

[203] Romero, P., Masad, E., 2001, "Relationship between the representative volume element and mechanical properties of asphalt concrete," J.Mater.Civ.Eng., **13**(1), pp. 77-84.

[204] Metcalfe, C., Kesler, O., Rivard, T., Gitzhofer, F., Abatzoglou, N., 2010, "Connected three-phase boundary length evaluation in modeled sintered composite solid oxide fuel cell electrodes," J.Electrochem.Soc., **157**(9), pp. B1326-B1335.

[205] Joos, J., Ender, M., Carraro, T., Weber, A., Ivers-Tiffée, E., 2012, "Representative volume element size for accurate solid oxide fuel cell cathode reconstructions from focused ion beam tomography data," Electrochim.Acta, **82**, pp. 268-276.

[206] Kenney, B., Valdmanis, M., Baker, C., Pharoah, J. G., Karan, K., 2009, "Computation of TPB length, surface area and pore size from numerical reconstruction of composite solid oxide fuel cell electrodes," J.Power Sources, **189**(2), pp. 1051-1059.

[207] Bertei, A., Nucci, B., Nicolella, C., 2013, "Microstructural modeling for prediction of transport properties and electrochemical performance in SOFC composite electrodes," Chemical Engineering Science, **101**, pp. 175-190.

[208] Cai, Q., Adjiman, C. S., Brandon, N. P., 2011, "Modelling the 3D microstructure and performance of solid oxide fuel cell electrodes: Computational parameters," Electrochim.Acta, **56**(16), pp. 5804-5814.

[209] Berson, A., Choi, H., Pharoah, J. G., 2011, "Determination of the effective gas diffusivity of a porous composite medium from the three-dimensional reconstruction of its microstructure," Physical Review E, **83**(2), pp. 026310.

[210] Costamagna, P., Costa, P., Antonucci, V., 1998, "Micro-modelling of solid oxide fuel cell electrodes," Electrochim.Acta, **43**(3-4), pp. 375-394.

[211] Bertei, A., Nicolella, C., 2011, "Percolation theory in SOFC composite electrodes: Effects of porosity and particle size distribution on effective properties," J.Power Sources, **196**(22), pp. 9429-9436.

[212] Chen, D., Lin, Z., Zhu, H., Kee, R. J., 2009, "Percolation theory to predict effective properties of solid oxide fuel-cell composite electrodes," J.Power Sources, **191**(2), pp. 240-252.

[213] G. Matheron, Estimating and Choosing, Springer; 1989.

[214] A. Bunde, S. Havlin, Fractals and Disordered Systems, Springer-Verlag, New York, Inc.; 1991.

[215] Grimmett, G., "Percolation", volume 321 of Grundlehren der mathematischen Wissenschaften, 2nd edition, Springer-Verlag; 1999.

[216] A. Aharony, D. Stauffer, Introduction to percolation theory, Taylor & Francis; 2003.

[217] Bouvard, D., Lange, F., 1991, "Relation between percolation and particle coordination in binary powder mixtures," Acta Metallurgica et Materialia, **39**(12), pp. 3083-3090.

[218] Kuo, C., Gupta, P. K., 1995, "Rigidity and conductivity percolation thresholds in particulate composites," Acta Metallurgica et Materialia, **43**(1), pp. 397-403.

[219] Nan, C., Shen, Y., Ma, J., 2010, "Physical properties of composites near percolation," Annual Review of Materials Research, **40**, pp. 131-151.

[220] Suzuki, M., Oshima, T., 1983, "Estimation of the co-ordination number in a multi-component mixture of spheres," Powder Technol, **35**(2), pp. 159-166.

[221] Deng, Y., Blöte, H. W., 2005, "Monte Carlo study of the site-percolation model in two and three dimensions," Physical Review E, **72**(1), pp. 016126.

[222] Wang, J., Zhou, Z., Zhang, W., Garoni, T. M., Deng, Y., 2013, "Bond and site percolation in three dimensions," Physical Review E, **87**(5), pp. 052107.

[223] Jan, N., Stauffer, D., 1998, "Random site percolation in three dimensions," International Journal of Modern Physics C, **9**(02), pp. 341-347.

[224] Acharyya, M., Stauffer, D., 1998, "Effects of boundary conditions on the critical spanning probability," International Journal of Modern Physics C, **9**(04), pp. 643-647.

[225] Powell, M., 1979, "Site percolation in randomly packed spheres," Physical Review B, **20**(10), pp. 4194.

[226] Hoshen, J., Kopelman, R., 1976, "Percolation and cluster distribution. I. Cluster multiple labeling technique and critical concentration algorithm," Physical Review B, **14**(8), pp. 3438-3445.

[227] Anderson, T. W., Darling, D. A., 1954, "A test of goodness of fit," Journal of the American Statistical Association, **49**(268), pp. 765-769.

[228] Meirer, F., Liu, Y., Pouyet, E., Fayard, B., Cotte, M., Sanchez, C., Andrews, J. C., Mehta, A., Sciau, P., 2013, "Full-field XANES analysis of Roman ceramics to estimate firing conditions - A novel probe to study hierarchical heterogeneous materials," J.Anal.At.Spectrom., **28**(12), pp. 1870-1883.

[229] Nazaretski, E., Huang, X., Yan, H., Lauer, K., Conley, R., Bouet, N., Zhou, J., Xu, W., Eom, D., Legnini, D., Harder, R., Lin, C.-H., Chen, Y.-S., Hwu, Y., Chu, Y. S., 2014, "Design and performance of a scanning ptychography microscope," Rev.Sci.Instrum., **85**(3), 033707.

[230] Cats, K. H., Gonzalez-Jimenez, I. D., Liu, Y., Nelson, J., van Campen, D., Meirer, F., van der Eerden, Ad MJ, de Groot, F. M., Andrews, J. C., Weckhuysen, B. M., 2013, "X-ray nanoscopy of cobalt Fischer–Tropsch catalysts at work," Chemical Communications, **49**(41), pp. 4622-4624.

[231] Rotureau, D., Viricelle, J.-P., Pijolat, C., Caillol, N., Pijolat, M., 2005, "Development of a planar SOFC device using screen-printing technology," Journal of the European Ceramic Society, **25**(12 SPEC. ISS.), pp. 2633-2636.

[232] Hui, R., Wang, Z., Kesler, O., Rose, L., Jankovic, J., Yick, S., Maric, R., Ghosh, D., 2007, "Thermal plasma spraying for SOFCs: Applications, potential advantages, and challenges," J.Power Sources, **170**(2), pp. 308-323.

[233] Wang, Z., Weng, W., Chen, K., Shen, G., Du, P., Han, G., 2008, "Preparation and performance of nanostructured porous thin cathode for low-temperature solid oxide fuel cells by spin-coating method," J.Power Sources, **175**(1), pp. 430-435.

[234] Sofie, S. W., 2007, "Fabrication of functionally graded and aligned porosity in thin ceramic substrates with the novel freeze-tape-casting process," J Am Ceram Soc, **90**(7), pp. 2024-2031.